

**GRAIN REFINEMENT AND SURFACE  
MODIFICATION TECHNIQUE BY EQUAL  
CHANNEL ANGULAR PRESSING AND  
LASER SHOCK PEENING ON MAGNESIUM  
ALLOY**

Thesis

Submitted in partial fulfilment of the requirement for the degree of  
**DOCTOR OF PHILOSOPHY**

by

**PRAVEEN T. R.**



**DEPARTMENT OF MECHANICAL ENGINEERING  
NATIONAL INSTITUTE OF TECHNOLOGY KARNATAKA,  
SURATHKAL, MANGALORE - 575025**

**July-2020**

## DECLARATION

I hereby declare that the Research Thesis entitled “**Grain Refinement and Surface Modification Technique by Equal Channel Angular Pressing and Laser Shock Peening on Magnesium Alloy**” which is being submitted to the **National Institute of Technology Karnataka, Surathkal** in partial fulfilment of the requirements for the award of the degree of Doctor of Philosophy in **Mechanical Engineering** is a bonafide report of research work carried out by me. The material contained in this Research Thesis has not been submitted to any other universities or institutes for the award of any degree.

Register number: **158014ME15F21**

Name of the research scholar: **Praveen T. R.**

Signature of the research scholar:

Department of Mechanical Engineering

Place: **NITK-Surathkal**

Date: 13-07-2020

## CERTIFICATE

This is to certify that the Research Thesis entitled “**Grain Refinement and Surface Modification Technique by Equal Channel Angular Pressing and Laser Shock Peening on Magnesium Alloy**” submitted by **Mr. Praveen T. R.** (**Register Number: 158014ME15F21**) as the record of the research work carried out by him, is *accepted as the Research Thesis submission* in partial fulfilment of the requirements for the award of the Degree of **Doctor of Philosophy**.

Dr. H. Shivananda Nayaka

Research guide

Date:

Chairman- DRPC

Date:

## **Acknowledgment**

At first, I would like to express my sincere gratitude and heartiest thanks to **Dr. H. Shivananda Nayaka**, Associate Professor, Department of Mechanical Engineering, National Institute of Technology Karnataka (NITK), Surathkal for the greatest support during my stay in NITK. The research work carried out here is supervised by him and there was extensive motivation and encouragement, which led to completion of my research work. I got an opportunity to develop lot of personality skills and this gave me new dimension in understanding different situation.

It is an opportunity to thank the RPAC members, **Dr. Ramesh M. R.** Associate Professor, Department of Mechanical Engineering and **Dr. Nagendrappa H.** Assistant Professor, Department of Electrical and Electronics Engineering, for evaluating the work and there precise suggestions and extended support during my research work.

I would like to thank **Dr. Kumar G. N.** for providing an opportunity to involve in departmental activities and greatest support during my stay in NITK.

I express my sincere gratitude to **Dr. K. V. Gangadharan** and **Dr. S. Narendranath**, Professor and former Head of the Mechanical Engineering Department for their extended support for my research work.

I wish to thank **Dr. Shrikantha S. Rao**, Professor and Head of the Department, and all the faculties in Department of Mechanical Engineering for giving the opportunity to utilize the facilities in the Department and valuable support to complete my research work, and I would like to convey my gratitude to Mr. Jayadevadiga (Former), Mr. Verghese and Mr. Pradeep (Non-teaching staff) for their kind help during my work.

It's my pleasure to submit my gratitude for **Dr. Anandhan Srinivasan**, Professor and Head, and **Dr. Udaya Bhat K.** Professor and Former Head, Department of Metallurgical and Materials Engineering for providing opportunity to use the facilities in their department for completing my research work.

I would like to thank **Dr. Amba Shetty**, Professor and Head, and **Dr. Dwarakish G. S.** Professor and Former Head, Department of Applied Mechanics for giving an opportunity to conduct part of experiments in Department of Applied Mechanics. I convey my gratitude to Mr. Seetharam, Mr. Sreekanth and Mr. Shashi for their kind support to execute the experiments.

It is very important to thank **Dr. K. Umamaheshwar Rao**, Director, NITK and **Ministry of Human Resource and Development (MHRD)** for their financial and all other resources provided for me during my research.

I like to use this opportunity to thank **Dr. Sathya Swaroop**, School of Advanced Sciences, Vellore Institute of Technology, Vellore, for his guidance, support and hospitality during my visit to VIT and giving an opportunity to execute part of my research work in School of Advanced Sciences laboratay. In the same I like to thank their students Dr. Umapati, Mr. Praveen Kumar, Mr. Nataraj and Mr. Binod for their support for conducting experiments.

I would like to extend my gratitude to **Dr. Indradev S. Samajdar**, professor, Department of Metallurgical Engineering and Material Science for providing an opportunity to execute part of my experiments and the valuable suggestions.

I would like to thank **Dr. D. K. Ramesh**, Professor, U.V.C.E Bangalore for their kind support and encouragement in my carrier.

I would like to take this opportunity to thanks all my **colleagues in NITK** for their cheerful support and valuable time given for me, and the **TEAM-Hunters** for their support during my idiocy in NITK.

Finally I wish to thank my family, friends and teachers who are supported throughout my life and made me to reach till this stage. And special thanks to my parents.

**Praveen T. R.**

## **ABSTRACT**

Design and development of any part in mechanical design consists of three elemental parameters. Such as, selection of material, geometrical constrains (dimensioning) and loading or boundary conditions. Boundary conditions are the functional requirements of design which need to be satisfied from the geometry of the component by allowing optimal material to execute the function. Hence, selection of materials is the primary building block of any component in mechanical system. Selection of material is very crucial and based on type of loading, environment conditions and reliability to withstand for long duration.

Magnesium and its alloys have drawn great interest from the past decade due to its superior strength to weight ratio, bio-compatibility, effective manufacturing process and other positive attributes, but there are some limitation, such as effective strength, low fatigue life, low wear resistance and high corrosion rate. These properties can be altered by grain boundary characteristics, hence reformation of grain boundary to change the grain behaviour is of significant interest.

In most of the methods, one principle technique (controlling cooling rate while solidification, alloying, severe plastic deformation) is used to alter the grain size of a material, which affects the grains in whole material or at near surface. Hence, there is a research gap while combining two different techniques to achieve combination of grains for better application. Severe plastic deformation (SPD) is a top down approach to form fine grains from coarse grain, and equal channel angular pressing (ECAP) is one of the simple procedures in SPD to achieve fine grains effectively. Samples during the ECAP process experience severe shear strain followed by deformation of grains, which rupture the coarse grains into new grains with redistributed grain boundaries. Formation of fine grains and grain boundary redistribution by ECAP enhances the strength and other mechanical properties in accordance with Hall-Petch relation. Conversion of coarse grains into fine grains occurs throughout the sample and resultant grain size depends on number of passes and route of the pass. But the original shape of the sample doesn't get altered after processing. Laser shock peening (LSP) is a surface treatment process, to induce compressive residual stresses at the surface. This technique involves creating permanent deformation at the surface, which causes grain refinement

at near surface. Grain refinement of bulk sample is obtained by ECAP process, whereas grain refinement at the surface of already deformed ECAP processed sample, is obtained by laser shock peening process.

Present work describes the combined effect of ECAP and LSP on AM80 magnesium alloy. As-received (cast) AM80 (Wt. 8% of Al, Wt. 1 % of Mn, balance Mg) material is homogenized and processed by ECAP upto 4 passes under route Bc. The samples were tested for mechanical properties, which showed enhancement of strength and ductility in ECAP processed samples. Microscopic investigation revealed the formation of fine grains, due to applied shear strain. By increasing the number of ECAP passes, more fine grains are reported. 2-pass ECAP processed sample shows heterogeneous grains, where the large grains were surrounded by small grains, and possess maximum tensile strength of 310 MPa compared to 1, 3 and 4-pass samples. Therefore, 2-pass ECAP processed sample is considered for further processing by LSP. LSP is carried out with a power density of  $8 \text{ GWcm}^{-2}$  and repeatedly to achieve different percentage of coverages, LSP processed samples are analysed for mechanical properties and microstructural characterization.

Microscopic examination revealed the formation of fine grains in the range of few nanometers after peening near the surface. Scanning electron microscope revealed the formation of flower petal like structures, and transmission electron microscope revealed elongated grains in the form of bands, and these bands overlapped as the percentage of coverage increases. There was a slight increase in tensile strength in LSP processed samples, due to strain hardening at surface. Dimples of various sizes were observed on fracture surface of ECAP+LSP processed region.  $\text{Mg}_{17}\text{Al}_{12}$ ,  $\text{Mg}_2\text{Al}_3$ ,  $\text{MnAl}_6$  with Mg phases were identified by X-ray diffraction. Wear studies of LSP processed region showed an increase in wear resistance, and microscopic image of wear surface reveals the wear mechanisms due to oxidation and ploughing of hard particles. Roughness measurement was carried out on ECAP+LSP processed samples and there was significant influence of peening in increasing roughness of the surface.

Nano indentation experiments help to understand the hardness behaviour of processed material at nano scale. An increase in surface hardness is observed with LSP processed samples compared to as-cast and ECAP processed samples. Further, there was an

increase in toughness and yield strength in peened region. D-space measurements were done by X-ray diffraction to measure the lattice space before and after peening, and relative strains were converted into stresses and residual stresses were identified. Tensile residual stress profile is identified in as-cast sample due to solidification of molten metal, and homogenized sample showed decrease in tensile residual stress value due to kinetic grain growth. ECAP processed sample shows compressive residual stresses due to strains induced in between the lattice. But ECAP+LSP processed sample shows higher compressive stress at near surface (peened region). Fatigue experiments played crucial role to characterize the material in cyclic loads for reliability. Experiments were conducted at maximum stress of 120 MPa, with a stress ratio of 0.125. ECAP+LSP processed sample with 100 % coverage took 85268 cycles of load compared to homogenized sample (1 cycle of load). Investigation of fractured surface of fatigue samples showed crack initiation and propagation region followed by rupture. ECAP+LSP processed sample with 100 % of coverage shows, significant gap between crack initiation and rupture region. Hence delay in crack initiation and propagation was observed.

**Key words:** Magnesium alloy, SPD, ECAP, LSP, grain refinement, Residual stresses, Fatigue.



## CONTENTS

<b>LIST OF FIGURES</b>	<b>v</b>
<b>ABBREVATIONS</b>	<b>xi</b>
<b>SYMBOLS</b>	<b>xiii</b>
<b>CHAPTER 1</b>	
<b>INTRODUCTION</b>	<b>1</b>
1.1 Importance of material	1
1.2 Grain refinement	1
1.3 Surface treatment	2
1.4 Laser Shock Peening	2
1.5 AM series of magnesium alloy	2
<b>CHAPTER 2</b>	
<b>LITERATURE REVIEW</b>	<b>5</b>
2.1 Introduction	5
2.2 Crystallographic aspects of Mg	5
2.3 Introduction to Grain Size Modification	7
2.4 Severe Plastic deformation (SPD)	8
2.5 Classification of SPD	8
2.5.1 Equal channel angular pressing	8
2.5.2 Torsion/shear under high pressure	9
2.5.3 Direct/indirect extrusion	10
2.5.4 Pressing/forging method	11
2.5.5 Roll Bonding	12
2.5.6 Combined SPD techniques	13
2.6 Applications of SPD	14
2.7 Equal channel angular pressing (ECAP)	15
2.7.1 Strain Imposed during ECAP	15
2.7.2 Processing routes of ECAP	17
2.7.3 Slip system associated with different processing routes	18
2.7.4 Experimental Factors on ECAP procedure	18
2.7.5 Mechanism of grain refinement	19
2.8 Surface Modification	20

2.9	Laser shock peening	21
2.10	Advantages of plastic deformation	22
2.11	Literatures	22
2.12	Motivation for proposed work	31
2.13	Objectives of Research	31
<b>CHAPTER 3</b>		
<b>METHODOLOGY</b>		<b>33</b>
3.1	Material	34
3.2	ECAP die setup and working procedure	35
3.3	Execution of ECAP	35
3.4	Laser shock peening	37
3.5	Material characterization	38
3.5.1	Microstructure Characterization	39
3.5.2	Material phase and residual stress analysis using X-ray diffraction	41
3.6	Mechanical properties evaluation	42
3.6.1	Tensile characterization	42
3.6.2	Wear characterization	44
3.6.3	Nano indentation	45
3.6.4	Surface roughness	46
3.6.5	Fatigue characterization	47
<b>CHAPTER 4</b>		
<b>RESULTS AND DISCUSSIONS</b>		<b>49</b>
4.1	Equal channel angular pressing of AM80 alloy	49
4.1.1	Microstructure analysis	49
4.1.2	SEM analysis of ECAP processed samples	51
4.1.3	X-Ray diffraction analysis	55
4.1.4	Tensile strength	56
4.1.5	Fractography	58
4.2	Laser shock peening without coating carried on ECAP 2-pass processed samples	62
4.2.1	TEM analysis	63
4.2.2	XRD Analysis	66
4.2.3	Tensile strength	67

4.2.4	Fracture analysis of tensile failure	68
4.3	Nano indentation	70
4.3.1	Relation between hardness and depth of peening	74
4.4	Roughness measurement	77
4.5	Wear characteristic analysis	79
4.6	Residual stress Analysis	81
4.7	Fatigue analysis	86
4.7.1	Fracture analysis of fatigue samples	89
4.8	Summary	93
4.8.1	ECAP processed samples	93
4.8.2	ECAP-LSPwC processed samples	95
4.8.3	Nano Indentation	96
4.8.4	Roughness measurement	98
4.8.5	Wear analysis	97
4.8.6	Residual stresses	97
4.8.7	Fatigue analysis	97
<b>CHAPTER 5</b>		
<b>CONCLUSIONS</b>		<b>99</b>
5.1	Equal channel angular pressing for bulk refinement of grains	99
5.2	Laser shock peening for grain refinement at near surface	99
<b>FUTURE WORK</b>		<b>103</b>
<b>REFERENCES</b>		<b>105</b>
<b>LIST OF PUBLICATIONS</b>		<b>113</b>
<b>BIO DATA</b>		<b>115</b>

## LIST OF FIGURES

Figure 2.1 Hexagonal close-packed (HCP) crystal lattice and major planes of Mg	05
Figure 2.2 Classification of SPD technique based on ECAP method	09
Figure 2.3 Classification of SPD technique based on torsion/shear under high pressure method	10
Figure 2.4 Classification of SPD technique based on direct/indirect extrusion method	11
Figure 2.5 Classification of SPD technique based on pressing/forging method	12
Figure 2.6 Classification of SPD technique based on rolling method	13
Figure 2.7 Classification of SPD technique based on rolling method	14
Figure 2.8 (a) Commercial ECAE die with 4000 ton capacity and (b) ECAP processed pure Ti dental implant, used to install metal ceramic crown	15
Figure 2.9 Principle of ECAP, shear plane inside the die, acting on specimen: element 2 is transposed of element 1 due to shearing inside the die. (b) ECAP with different arc of curvature at point of intersection: (1) (a) $\Psi = 0$ , (2) $\Psi = \pi - \Phi$ and (3) $\Psi = 0^\circ < (\pi - \Phi)$	16
Figure 2.10 Characterization of Equivalent strain $\epsilon_N$ , with angle of intersection $\Phi$ and curvature angle $\Psi$	17
Figure 2.11 Different routes of ECAP processing	17
Figure 2.12 (a) slip planes associated with different routes for ECAP processing and (b) flow of slip planes under different processing routes	18
Figure 2.13 Experimental die setup with back pressure setup, two punches were used in setup where the first punch is used for the pressing the sample inside the die, and second punch controls the back pressure	19
Figure 2.14 Schematic representation of evolution of microstructure during first pass	19
Figure 2.15 Surface modification techniques (a) Deep rolling, (b) low plasticity burnishing, (c) ultrasonic peening, (d) shot peening and (e) laser shock peening	21

Figure 2.16 Schematic representation of laser shock peening	22
Figure 2.17 Effect of grain size on strength of a material	23
Figure 2.18 Magnesium grain refinement by alloying	24
Figure 2.19 Microstructure of AZ91 with (a) cavity and (b) crack propagating inter dendritic and trans dendritic	24
Figure 2.20 SEM images of fatigue crack growth at different loading on AM50 (a) $\sigma_{max}$ 128 MPa, TZ150 8C, NZ4109, (b) plastic slip vestiges near crack tip at $\sigma_{max}$ 125 MPa, TZ150 8C, NZ5819 and (c) notch shape at $\sigma_{max}$ 128 MPa, TZ150 8C, NZ4260	25
Figure 2.21 Microstructure of (a) AZ31B, (b) AZ31B treated with HIFR and (c) cross sectional microhardness of as received and HIFR treated sample	25
Figure 2.22 Fatigue characterization of AM60 processed by ECAP	27
Figure 2.23 Microstructure of Mg-Al alloy with increase in Al content	29
Figure 3.1 Flow chart for experimental procedure followed to conduct the experiments and testing	33
Figure 3.2 Cast AM80 rods in as received condition	34
Figure 3.3 Machined sample of AM80 to execute ECAP	34
Figure 3.4 (a) Sectional view ECAP split die with heating coils and plunger, (b) Material flow mechanism during ECAP	35
Figure 3.5 ECAP setup	36
Figure 3.6 ECAP processed sample with processed sample. (a) Split die (b) split die with sample insertion and (c) processed sample with plunger	36
Figure 3.7 ECAP processed sample	37
Figure 3.8 LSP setup (a) Schematic view of LSP setup, (b) view of work table, and (c) Laser pulsed spot of diameter 0.2 mm with overlapping parameter	37
Figure 3.9 ECAP+LSP proceeds sample for material characterisation	38
Figure 3.10 Mechanical disc polishing machine	39

Figure 3.11 (a) Optical microscope (Ziess, Aixolab A1), (b) Scanning electron microscope (JEOL JSM- 7100F)	39
Figure 3.12 Sample preparation for TEM (a) dimpling machine and (b) Ion beam milling machine	40
Figure 3.13 TEM facility (TEM-JOEL-JEM-2100)	41
Figure 3.14 X-ray diffraction unit (Panalytical-X'Pert <sup>3</sup> )	41
Figure 3.15 Tensile test sample details	43
Figure 3.16 Shimadzu universal testing machine	43
Figure 3.17 Wear testing machine (Pin on disc Tribometer, Ducom)	44
Figure 3.18 Agilet G200 Nanoindenter	45
Figure 3.19 (a) Locations of Nano indentation carried out on ECAP and ECAP+LSP processed sample, and (b) zoomed view of data points	46
Figure 3.20 Confocal microscope (Olympus LEXT 4000)	46
Figure 3.21 (a) Schematic representation of Fatigue sample description and (b) Stress ratio curve	47
Figure 4.1 Optical microstructures of AM80 alloy (a) as-cast, (b) homogenised at 350 °C for 24 hours	49
Figure 4.2 Optical images of AM80 alloy, ECAP processed at 275 °C (a) 1 pass, (b) 2 pass, (c) 3 pass, (d) 4 pass, (e) zoomed view of 4 pass.	50
Figure 4.3 SEM image with EDX data of as-cast sample	51
Figure 4.4 SEM image with EDX data of homogenised sample	52
Figure 4.5 SEM image with EDX data of 1-pass ECAP processed sample	52
Figure 4.6 SEM image with EDX data of 2-pass ECAP processed sample	53
Figure 4.7 SEM image with EDX data of 3-pass ECAP processed sample	54
Figure 4.8 SEM image with EDX data of 4-pass ECAP processed sample	54
Figure 4.9 XRD profile of (a) as-cast (b) ECAP 2P and (c) ECAP 4P samples	55

Figure 4.10 Tensile strength of ECAP processed AM80 alloy under different passes	56
Figure 4.11 Comparison of yield strength, tensile strength and elongation of samples	57
Figure 4.12 SEM Image of fracture surface for as-cast sample (Tensile)	58
Figure 4.13 SEM Image of fracture surface of 1-pass ECAP processed sample (Tensile)	59
Figure 4.14 SEM Image of fracture surface for 2-pass sample under route B <sub>C</sub> (Tensile)	60
Figure 4.15 SEM Image of fracture surface for 3-pass sample under route BC (Tensile)	60
Figure 4.16 SEM Image of fracture surface for 4-pass sample under route B <sub>C</sub> (Tensile)	61
Figure 4.17 SEM Image of fracture surface for near surface zoomed view of 2-pass sample Route B <sub>C</sub>	62
Figure 4.18 TEM image of ECAP 2-pass processed under route B <sub>C</sub> with SAED pattern	63
Figure 4.19 TEM image of ECAP 2-pass processed under route B <sub>C</sub> and LSP processed with 8 GWcm <sup>-2</sup> (100 % of coverage) with SAED pattern	64
Figure 4.20 TEM image of ECAP 2-pass processed under route B <sub>C</sub> and LSP processed with 8 GWcm <sup>-2</sup> (200 % of coverage) with SAED pattern	65
Figure 4.21 TEM image of ECAP 2-pass processed under route B <sub>C</sub> and LSP processed with 8 GWcm <sup>-2</sup> (300 % of coverage) with SAED pattern	66
Figure 4.22 XRD patterns of AM80 alloy at different stages of processing for grain refinement	67
Figure 4.23 Tensile stress-strain behaviour of ECAP processed AM80 with LSPwC at different percentage of coverage	68
Figure 4.24 SEM Image of fracture surface for LSPwC with 100 % coverage of 2-Pass ECAP processed route B <sub>C</sub> samples	69

Figure 4.25 SEM Image of fracture surface for LSPwC processed with 200% coverage of ECAP 2-Pass processed route B <sub>C</sub> samples	70
Figure 4.26 SEM Image of fracture surface for LSPwC processed with 300 % coverage of 2-Pass ECAP processed route B <sub>C</sub> samples	70
Figure 4.27 Indenter marks after executing the tests on 2-pass ECAP processed sample	71
Figure 4.28 shows the data extracted from nano indentation experiment for ECAP 2-pass processed AM80 sample. (a) Load V/s displacement curve, (b) Hardness along the depth and (c) modulus along the depth	72
Figure 4.29 Load V/S displacement plot at different processing stage	73
Figure 4.30 Hardness measurement of AM80 sample at different processing stage	74
Figure 4.31 Schematic representation of effect of nano-indentation on grain refinement.	75
Figure 4.32 Characterization of modulus of AM80 at different processing stage	76
Figure 4.33 Confocal microscopic image of (a) ECAP processed and polished with SiC paper, surface treated with LSPwC (b) 100, (c) 200, (d) 300 % of coverage	77
Figure 4.34 Roughness (R <sub>a</sub> ) measurement of peened samples	78
Figure 4.35 Formation of dents (permanent deformation) on the surface	78
Figure 4.36 (a) Friction coefficients and (b) wear rate of ECAP processed 2-Pass sample under route B <sub>C</sub> additionally surface treated with LSPwC AM80 alloy	79
Figure 4.37 SEM images of worn surfaces of (a)ECAP processed 2-Pass sample under route B <sub>C</sub> (b) ECAP processed with LSPwC 100% coverage (c) 200% coverage (d) 300% coverage and (e) EDS image of worn surface with elemental mapping	80
Figure 4.38 Schematic representation of co-ordinate system for measurement of d space for measuring residual strains	81
Figure 4.39 shows the diffraction peaks extracted from Xpert pro, at $2\theta = 60$ to $66^\circ$ , $\phi = 0$ and $\psi = -40$ to $40^\circ$	82



Figure 4.40 Lattice spacing $d$ against $\sin^2\psi$ for (a) $\phi = 0^\circ$ , (b) $\phi = 45^\circ$ , and (c) $\phi = 90^\circ$ for ECAP processed sample at surface	84
Figure 4.41 variation of residual stress with depth of penetration for different processing condition	85
Figure 4.42 Fatigue life of AM80 alloy at different processing stage	87
Figure 4.43 Fractured specimens after fatigue testing	87
Figure 4.44 Effect of compressive residual stresses during fatigue loading	88
Figure 4.45 Fracture topography of as cast AM80 alloy due to fatigue failure	89
Figure 4.46 Fracture topography of 2-pass ECAP processed at route B <sub>C</sub> AM80 alloy due to fatigue failure	90
Figure 4.47 Fracture topography of 2-pass ECAP+LSP 100% coverage processed at route B <sub>C</sub> AM80 alloy due to fatigue failure	91
Figure 4.48 Fracture topography of 2-pass ECAP+LSP 200% coverage processed at route B <sub>C</sub> AM80 alloy due to fatigue failure	91
Figure 4.49 Fracture topography of 2-pass ECAP+LSP 300% coverage processed at route B <sub>C</sub> AM80 alloy due to fatigue failure	92
Figure 4.50 surface defects observed at fracture topography of 2-pass ECAP+LSP 200 and 300 % coverage processed at route B <sub>C</sub> AM80 alloy	92

## ABBREVIATIONS

A	Area
AM	Aluminium-Manganese
ASTM	American Society for Testing and Materials
AZ	Aluminium-Zinc
BCC	Body Centered Cube
CNC	Computer Numerical Control
CRSS	Critically Resolved Shear Stress
ECAE	Equal Channel Angular Extrusion
ECAP	Equal Channel Angular Pressing
EDX	Energy Dispersive X-ray Analysis
ELS	Elongated Laminar Structure
$E_r$	Elastic Modulus
FCC	Face Centered Cube
H	Hardness
HAGB	High Angle Grain Boundary
HCP	Hexagonal Close-Packed
HIFR	High-frequency impacting and rolling
HRC	Hardness Rockwell C
LSP	Laser Shock Peening
LSPwC	Laser Shock Peening without Coating
MSP	Main Slip Plane
Nd:YAG	Neodymium-Doped Yttrium Aluminum Garnet

OM	Optical Microscope
$P_{\max}$	Maximum Load
S	Slope of Unloading Curve
SAED	Selected Area Electron Diffraction
SEM	Scanning Electron Microscope
SPD	Severe Plastic Deformation
TEM	Transmission Electron Microscope
UTM	Universal Testing Machine
$W_{\text{Elastic}}$	Work done by elastic deformation
$W_{\text{Plastic}}$	Work done by plastic deformation
$W_{\text{Total}}$	Work done by total deformation
XRD	X-Ray Diffraction

## SYMBOLS

$\gamma$	Shear strain
$\epsilon_N$	Equivalent strain
$N$	Number of passes
$\tau_{CRSS}$	Critically resolved shear stress (CRSS)
$\sigma_{app}$	Applied stress
$\Lambda$	Angle between slip direction and force direction
$\Theta$	Angle between force and slip plane
$\cos(\lambda)\cos(\theta)$	Schmid factor (m)
$\sigma_y$	Yield stress
$\sigma_0$	Friction Stress
$K_y$	Constant of Yielding / Locking parameter
$d$	Grain Size
$Z$	Zener Hollomon Parameter
$Q$	Activation energy for deformation
$R$	Gas constant
$\dot{\epsilon}$	Strain rate
$T$	Temperature
$\phi$	Channel angle
$\Psi$	angle of curvature

# CHAPTER 1

## INTRODUCTION

### **1.1 Importance of material**

Processing of materials is a key factor for achieving desired properties of material. As the world is progressing towards light weight, eco-friendly and more stable structural materials for engineering applications, it is necessary to understand the behaviour of new materials, possessing high strength, high reliability, less corrosion and eco-degradability. Magnesium (Mg) is the lightest metal among all non-ferrous structural metals. It possesses high specific strength, good castability and machinability, high damping and dimensional stability, naturally degradable, recyclable and bio-compatible (Alaneme and Okotete 2017). Limitation of Mg is, its low strength at room temperature, highly reactive, low melting point and lesser fatigue and creep resistance (Kulekci 2008; Mordike and Ebert 2001). Apart from the above limitations, it has HCP structure, which bound the ductility of material, due to limited number of slip system. Hence, cold working is very crucial (Chapuis, 2014). Aluminium (Al) is one of the common alloying elements in commercial Mg alloys, which enhances ductility and hardness. Addition of Manganese (Mn) to Mg-Al based alloy increase corrosion resistance and creep strength, which also helps to reduce Iron (Fe) based impurities in alloy (Friedrich and L.Mordike 2006).

### **1.2 Grain refinement**

Grain refining is one of the proven methods to increase strength of material (Nieh and Wadsworth 1991). Grain refinement can be achieved by different methods, like, accelerating cooling rate during solidification, introduce rare earth elements while casting (Pan et al., Chen, 2016; Pourbahari et al., 2018), and severe plastic deformation (SPD). SPD is a top down technique to achieve ultra-fine grains by inducing strain, without significant dimensional changes (Azushima et al. 2008). There are many SPD techniques established in the past two decades, and ECAP is one of the simplest methods (Ruslan et al., 2006). Many investigations were carried out on AZ and AM series of Mg alloy for grain refinement and strengthening through ECAP (Vinogradov et al., 2017).

### **1.3 Surface treatment**

Surface treatment (Modification) is the process to generate high dislocation density in the near surface layer. These dislocations cause plastic deformation, which influence formation of residual stresses on surface topography which can be achieved by different methods. One of the most proven methods is applying external load to induce local plastic deformation, when load is released, these deformation leads to accumulation of compressive residual stresses on surface. Shot peening, laser peening and ultrasonic peening are the most common methods for inducing compressive residual stresses at near surface. In shot peening, tiny hard spherical balls are bombarded on the substrate at high velocities, which leads to small indentation and results in compressive residual stresses on the surface. Laser and ultrasonic peening work on same principle but indentation is created due shock waves, and shock waves are generated due to pulsed laser beam or ultrasonic vibrational source.

### **1.4 Laser Shock Peening**

Laser Shock Peening (LSP) is an effective surface modification technique to induce compressive residual stresses, which enhances fatigue life, wear resistance and corrosion resistance. Pulsed laser beam is used to generate discontinuous laser shocks for particular interval of time. These laser shocks are converted into stress waves and induce plastic deformation on surface. Plastic deformation can be controlled by changing amplitude of stress waves by changing intensity of Laser beam (Montross et al., 2002). Recently, Wu et al., (2018) investigated the effect of LSP on pure titanium under different temperatures. Micro hardness was increased by grain refinement, and significant improvement in tensile strength and plasticity was observed.

### **1.5 AM series of magnesium alloy**

Light weight AM series magnesium alloys draw more interest due to their superior properties like, resistance to corrosion and improved mechanical behaviour, compared to other Mg alloys. Gopi et al., (2016) processed AM70, AM80 and AM90 magnesium alloys, by ECAP, upto 4 passes and analysed the results, which indicated grain refinement on bulk solid. Study of surface modification on ECAP processed AM alloy was very interesting, as there was large reduction in grain size at surface layer, during

each ECAP passes, because of high deformation. These inelastic deformations on surface, delay crack initiation and propagation, which results in improved fatigue life. Grain boundary is a crucial parameter in crystalline materials for determining most of the properties. Study of these grain boundaries and changes in their parameters are attractive in current era, for improving material properties, and hence, it is named as grain boundary engineering. Grain boundaries are the defects, generated due to misorientation between adjacent grains and has been categorised as low angle grain boundaries, which having misorientation angle less than  $15^\circ$  and high angle grain boundaries. This technique is successfully used to analyse improvement in strength, creep, weldability and stress corrosion cracking, which are resulted by thermal (heat treatment), mechanical (SPD) and thermomechanical processes (Tan et al., 2008). Present work contains the characteristic features of AM80 alloy, processed through ECAP under route B<sub>C</sub>, followed by surface treated using LSP. Processed samples are tested with microscopic and mechanical tests to investigate the effect of ECAP and LSP together. Some interesting findings are observed, such as tailoring of grain size, increase in strength and ductility, increase in fatigue life and wear resistance. Here, it was tried to establish an eco-friendly, light weight, strong and sustainable material through mechanical processing (SPD method) by achieving grain refinement. Experimental method, results and discussions are presented at different chapters of the thesis.

## CHAPTER 2

### LITERATURE REVIEW

#### 2.1 Introduction

Magnesium (Mg) has an atomic number 12, placed in group 2 alkaline earth materials in periodic table, having density  $1.738 \text{ g/cm}^3$ , electron configuration  $1s^22s^22p^63s^2$ . It is the eighth most abundant element in earth's crust, and third most abundant ion dissolved in sea water, after sodium and chlorine. Mg occurs naturally in oxidized state, extracted by silico-thermic Pidgeon process (China, 80% of production) and electrolysis. British chemist Sir Humphry Davy extracted Mg from mixture of magnesia and mercuric oxide in 1808.

#### 2.2 Crystallographic aspects of Mg

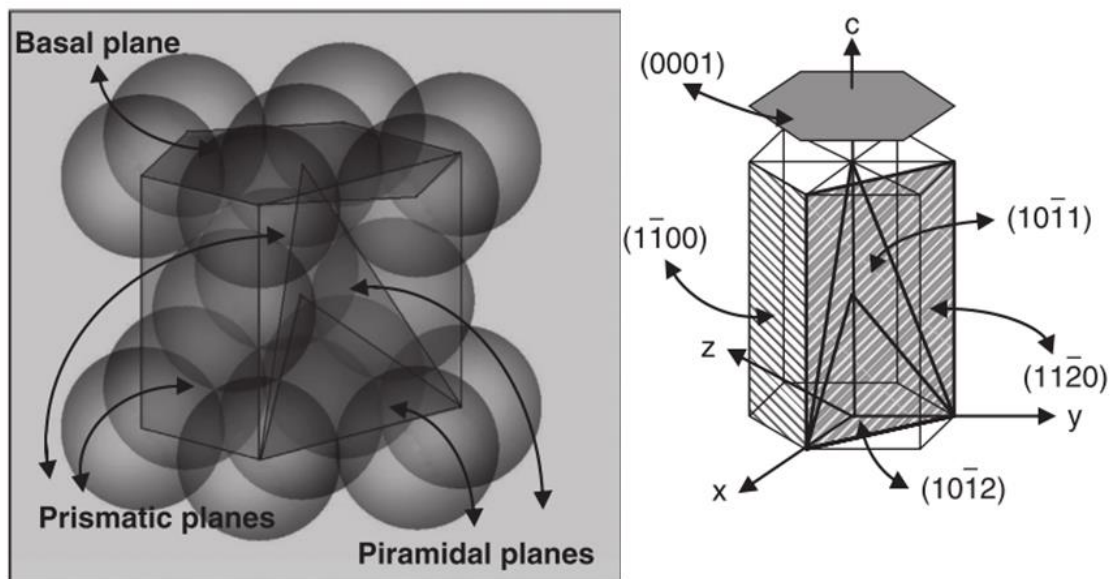


Figure 2.1 Hexagonal close-packed (HCP) crystal lattice and major planes of Mg (Pekguleryuz et al., 2013)

Mg has hexagonal close packing crystal (HCP) structure, shown in figure 2.1, with lattice parameter  $a=3.18 \text{ \AA}$  and  $c=5.19 \text{ \AA}$ . Stacking faults are planar defects, bounded by partial dislocations and are generated during deformation, which results in grain refinement. Mg has claimed uniquely, among other HCP structures, for its isotropic behaviour (thermal and elastic constants). Modulus of Elasticity is 45 GPa is very low, compared to other competitors (Al alloys and steel). Mg can be plastically deformed at



room temperature for very small deformations due to its limited ductility. It has only three slip systems and doesn't meet Von Mises Criterion for plastic deformation, which requires minimum of five independent slip systems. Limitations of slip systems were compensated by activation of twins, which leads to deformation of crystal along c-axis, till the prismatic and pyramidal slip systems get activated. Stacking fault energy for basal slip is about  $10 \text{ mJm}^{-2}$ , and it is very small compared to prismatic slip system. To achieve cross slip, Mg is to be processed at a high temperature of atleast  $225 \text{ }^\circ\text{C}$  (Obara et al. 1973). Increase in temperature increases more cross slip systems.

Critical resolved shear stress (CRSS) influences mechanical deformation (Kim et al., 2012). CRSS is a shear stress component, maximum at direction of slip, to initiate slip in grains. CRSS is related with Schmid law and is related to dislocation nucleation. Schmid Law is represented by

$$\tau_{CRSS} = \sigma_{app} \cos \lambda \cos \theta \quad (2-1)$$

Where

$\sigma_{app}$  = Applied stress

$\lambda$  = Angle between slip direction and force direction

$\theta$  = Angle between force and slip plane

$\cos(\lambda)\cos(\theta) = m$  = Schmid factor

Crystals, having highest Schmid factor, start yielding first, and CRSS can be achieved when  $\lambda$  and  $\theta$  become zero. Based on single crystal experiment, CRSS value of basal slip is 5 MPa, extension twinning is 10 MPa, prismatic slip is 20 MPa, pyramidal slip is 40 MPa and concentration twinning had 70-80 MPa (Chapuis & Driver, 2011). Deformation of Mg starts with basal slip at room temperature, once CRSS reaches 0.1 % of strain, twinning begins followed by basal slip. At some point, slip precedes and saturates rapidly and allows twinning to proceed. Schmid factor for non-basal planes is 1.5-2.0 times higher than basal plane due to its texture (Pekguleryuz et al. 2013). Both slips operate together, hence, non-basal slips are started due to plastic incompatibility in the vicinity of grain boundaries. Sliding of grain boundaries leads to 8 % of total strain at room temperature (Koike et al. 2003). Further, deformation occurs due to twinning and continuation of deformation leads to breakdown of grains and sub grains. The CRSS of  $\langle c+a \rangle$  slip is high at room temperature, and decreases quickly with

increase in temperature. (Brown et al. 2005; Agnew et al. 2003; Muránsky et al. 2010; Barnett et al. 2004).

### 2.3 Introduction to Grain Size Modification

Mechanical and physical properties of crystalline materials depend on factors like, grain orientation, grain boundaries and texture of grain. Average grain size of material plays important role, according to Hall-Petch Equation (Nieh and Wadsworth 1991).

$$\sigma_y = \sigma_0 + K_y d^{-1/2} \quad (2-2)$$

Where

$\sigma_y$  = Yield stress

$\sigma_0$  = Friction Stress

$K_y$  = Constant of Yielding / Locking parameter

$d$  = Grain Size

Frictional stress ( $\sigma_0$ ) increases with decrease in temperature,  $K_y$  is the yield strength, which measures localized stress needed to unlock dislocations held in grain boundaries and yielding can be transmitted to next grain (Dieter et al. 1962). From equation 2.2, it is found that yield strength increases with decreases in grain size. This relation given a big impact on tailoring grain size for specific applications. Hence, by achieving fine and ultra-fine grains, material will possess better strength.

Metals and their alloys, which having BCC and FCC crystals, show impressive increase in tensile strength, with loss of ductility, due to reduction in grain size. Mg (HCP) shows contrasting result with respect to BCC and HCP. Increase in tensile strength, with increase in ductility was reported by many authors (Vinogradov et al. 2017). According to most of the authors, increase in strength was achieved by introducing dislocations inside the grains and mobile dislocation at grain boundaries. Activation of non-basal slip systems at vicinity of grain boundaries minimises the formation of twins at finer grains, which requires high stress. Alternative deformation modes such as, grain boundary sliding under particular combination, strain rate and temperature leads to super elasticity and increase in flow stress (Kim, Park, and Chang 2012). St. John et al. 2005, reviewed the literatures on grain refinement of Magnesium alloys, with and without Al. Role of Zirconium was discussed for grain refinement and it showed better

result in absence of Al. Understanding grain refinement with Al was difficult, as it interacts with other impurities.

## 2.4 Severe Plastic deformation (SPD)

In the field of materials and engineering, SPD is a one of the attractive procedures to produce bulk nano grained and ultrafine-grained structures from past three decades. Dislocation glides and twinning are the major contributions for grain refinement in FCC. Temperature (T) and strain rate ( $\dot{\epsilon}$ ) were the process variables to control the nature of grain refinement during plastic deformation, and it is related by Zener Hollomon Parameter.

$$Z = \dot{\epsilon}^{-Q}/RT \quad (2-3)$$

Q is the activation energy for deformation, and R is a gas constant. Deformation at high strain rate and low temperature, causes higher values of Z, leads to high stacking fault energy and deformation, controlled by slip (dislocation activity) (Tao and Lu 2009). High angle grain boundaries (HAGBs) are induced due to non-equilibrium grain boundaries during plastic deformation, and these are the basic aspect for structural characterisation by dislocation activity (Valiev et al., 2000). Another mechanism is, grain refinement by twinning, which shows the formation of multiple deformation twins inside the coarse grain.

## 2.5 Classification of SPD

From the available literature, grain refinement by SPD showed potential advantage with formation of sub micro and nano scale grains. There are many SPD procedures reported from across the world to achieve grain refinement. Hence, it is classified based on the processing methods (Bagherpour et al., 2018) and are as follows:

### 2.5.1 Equal channel angular pressing

ECAP is sub divided into different methods, based on processing route, and some of the important ECAP SPD techniques are shown in figure 2.2. (a) Basic ECAP procedure, (b) Con-shearing process, (c) Continuous confined strip shearing, (d) ECAP–conform, (e) Integrated conventional tandem rolling with ECA deformation, (f)

Equal-channel angular pressing in parallel channels, (g) Equal channel angular swaging, (i) Rotary-die equal channel angular pressing and (j) T-shaped equal channel angular pressing.

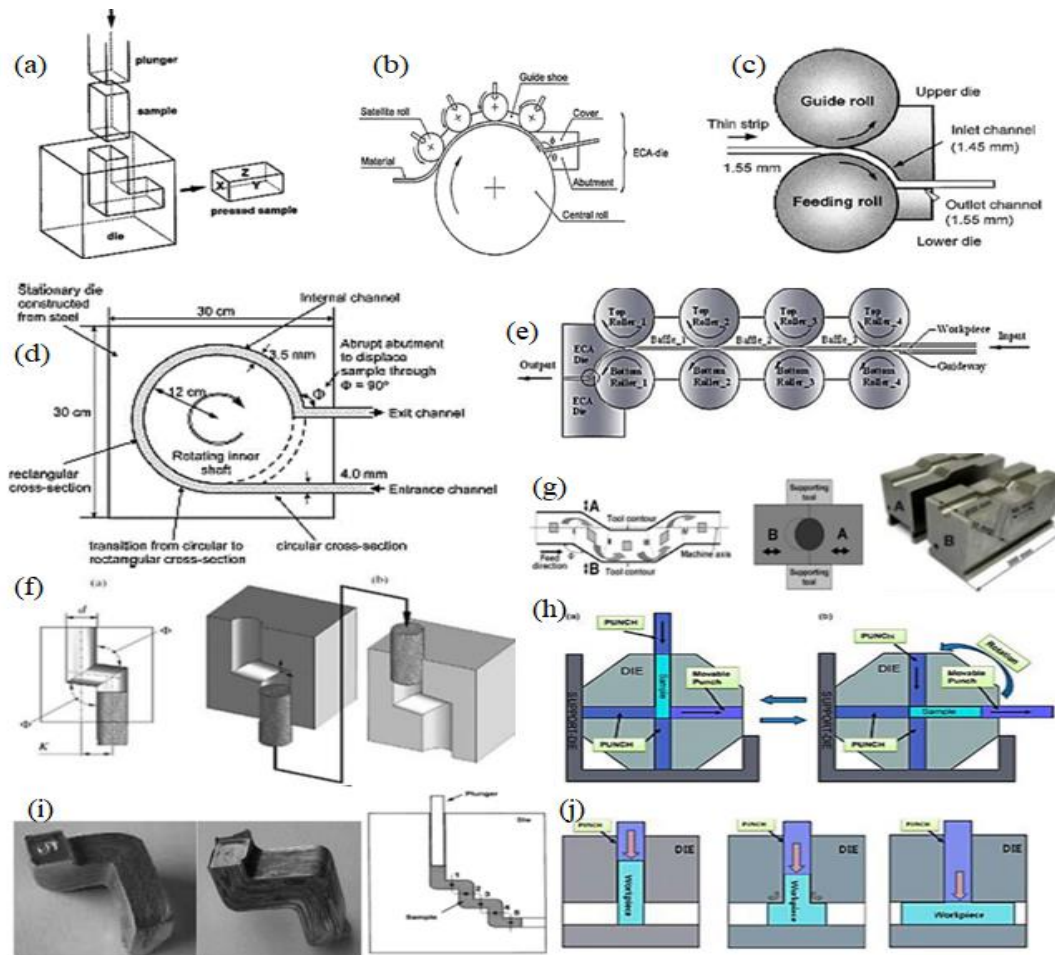


Figure 2.2 Classification of SPD technique based on ECAP method (Bagherpour et al. 2018)

### 2.5.2 Torsion/shear under high pressure

High Pressure Torsion (HPT) has high efficiency in grain refinement, but it has a limitation with sample size in deformed condition. Classification was reported based on processing sample geometry and some of them which are shown in figure 2.3 are (a) High pressure torsion, (b) High pressure shearing, (c) HPT for ring specimen, (d) Continuous high- pressure torsion for bars/rods, (e) high pressure tube twisting, (f) rotation torsion and (g) friction stir processing.

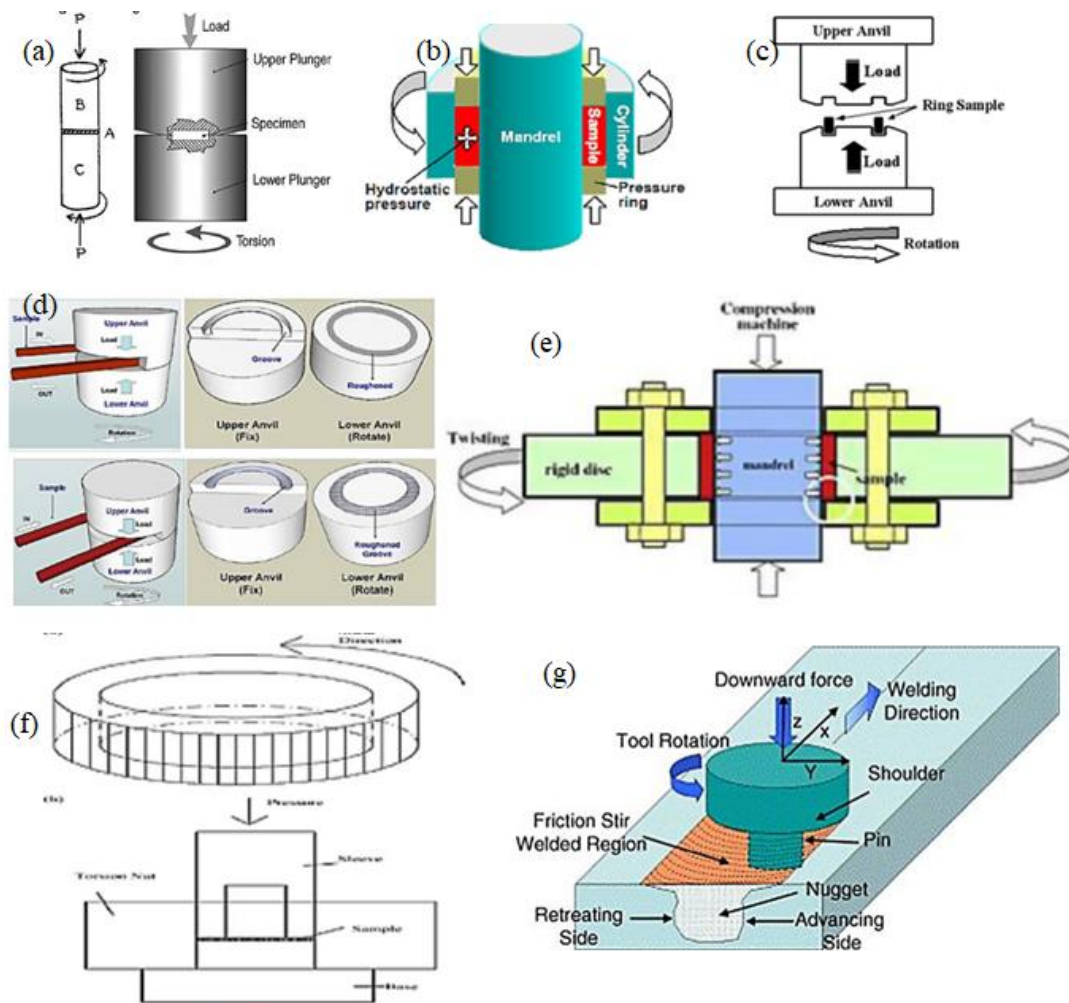


Figure 2.3 Classification of SPD technique based on torsion/shear under high pressure method (Bagherpour et al. 2018)

### 2.5.3 Direct/indirect extrusion

Sample were pushed through fixed geometrical die, where sample get deformed plastically, but final geometry of sample is same as initial one. This can be achieved by using direct or indirect die. Some of the SPD techniques based on direct/indirect method are shown in figure 2.4. (a) Twist extrusion, (b) Elliptical cross-section spiral equal-channel extrusion (c) off axis twist extrusion, (d) plastic flow machining, (e) spin extrusion, (f) compound extrusion and (g) alternate extrusion.

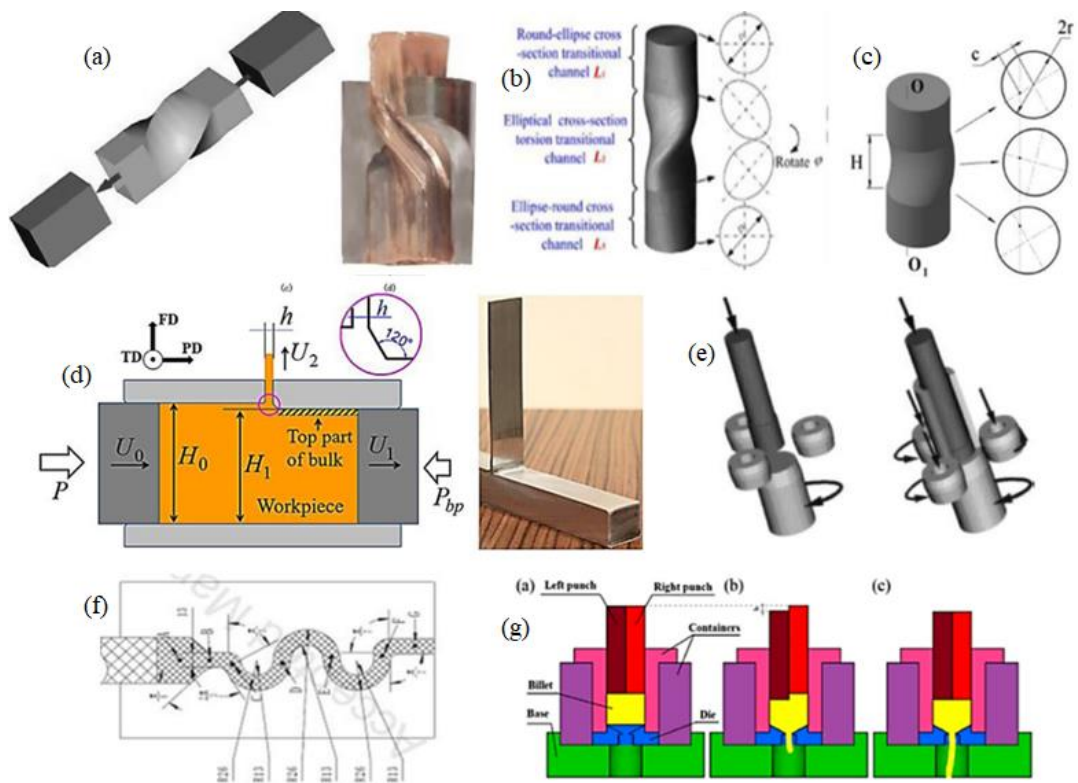


Figure 2.4 Classification of SPD technique based on direct/indirect extrusion method (Bagherpour et al. 2018)

#### 2.5.4 Pressing/forging method

Here, the samples are forged in open/closed die repeatedly on different faces of the sample. This procedure is suited for imposing large strain on samples. Some of the forging methods used for grain refinement through SPD technique are shown in figure 2.5. (a) Multi axial forging (Closed die), (b) Multi axial forging (open die), (c) Constrained groove pressing, (d) Accumulative channel-die compression bonding, (e) Alternate pressing & multi-axial compression, (f) Orbital rotary forging and (g) Continuous variable cross-section recycled extrusion.

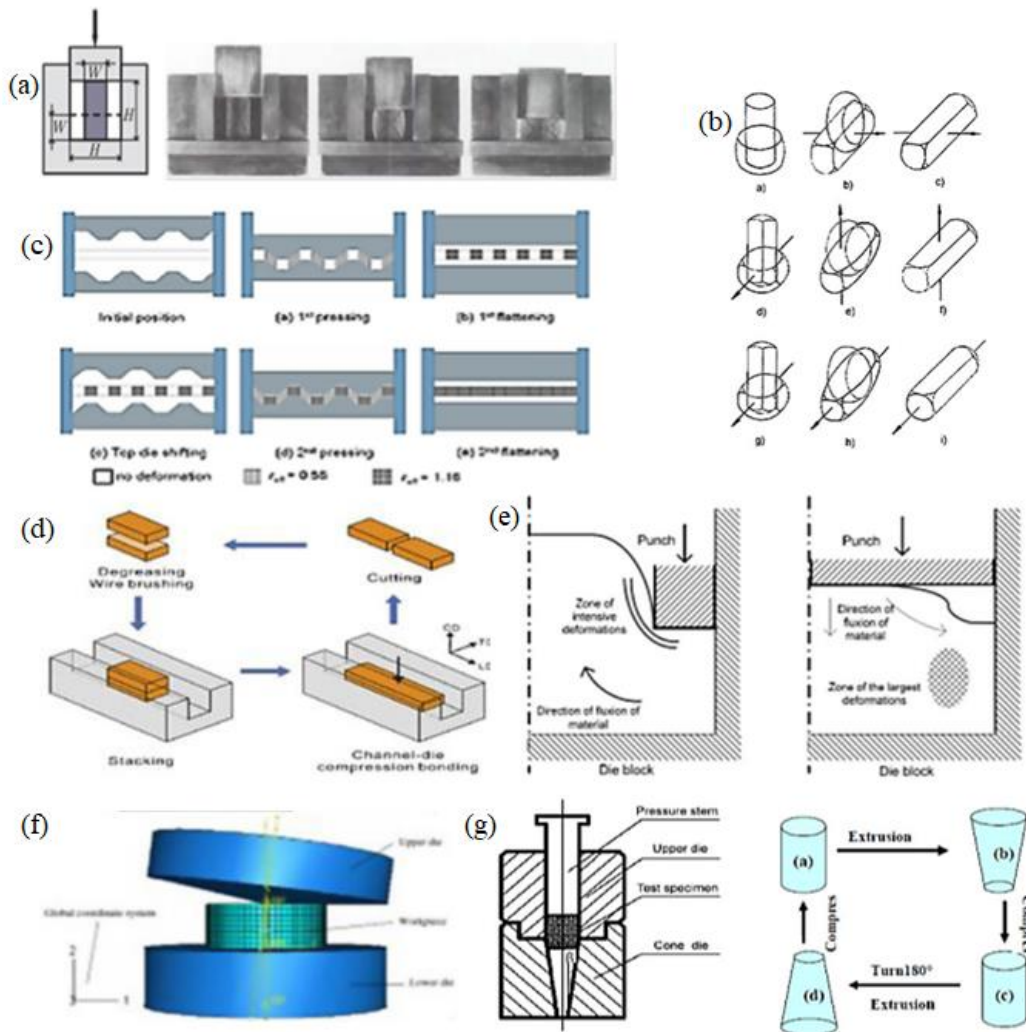


Figure 2.5 Classification of SPD technique based on pressing/forging method (Bagherpour et al. 2018)

### 2.5.5 Roll Bonding

Roll bonding is a well-known procedure to bond sheet metals through SPD technique. Plastic deformation was induced in between two metal sheets to bond each other by applying compressive load, and there was a formation of ultra-fine grains due to large strain during process. Different roll bonding techniques are shown in figure 2.6. (a) Accumulative roll-bonding, (b) Repetitive corrugation & straightening, (c) Asymmetric rolling, (d) Continuous cyclic bending, and (e) Accumulative spin bonding.

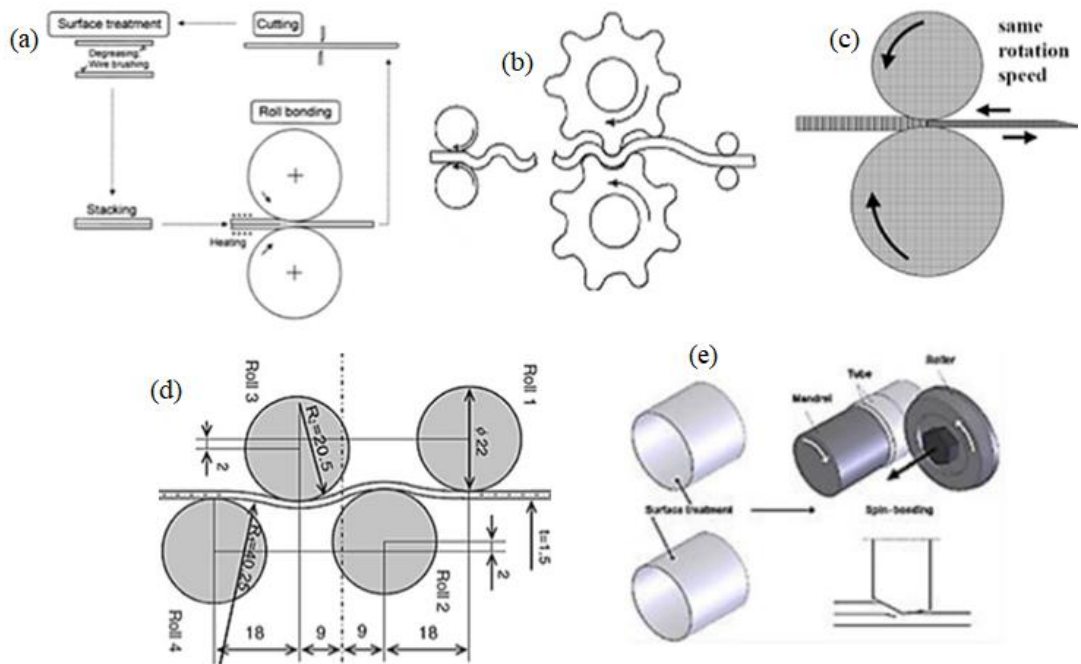


Figure 2.6 Classification of SPD technique based on rolling method (Bagherpour et al. 2018)

### 2.5.6 Combined SPD techniques

To achieve homogeneity and more refined grains, two SPD techniques are combined in a single die. Large strain accumulation was expected due to combined deformation. Some of the combined SPD technique used for grain refinement is shown in figure 2.7. (a) Torsional-equal channel angular pressing, (b) Twist channel angular pressing, (c) ECAP forward extrusion, (d) Expansion equal channel angular extrusion, (e) KOBO method and (f) Torsion extrusion.



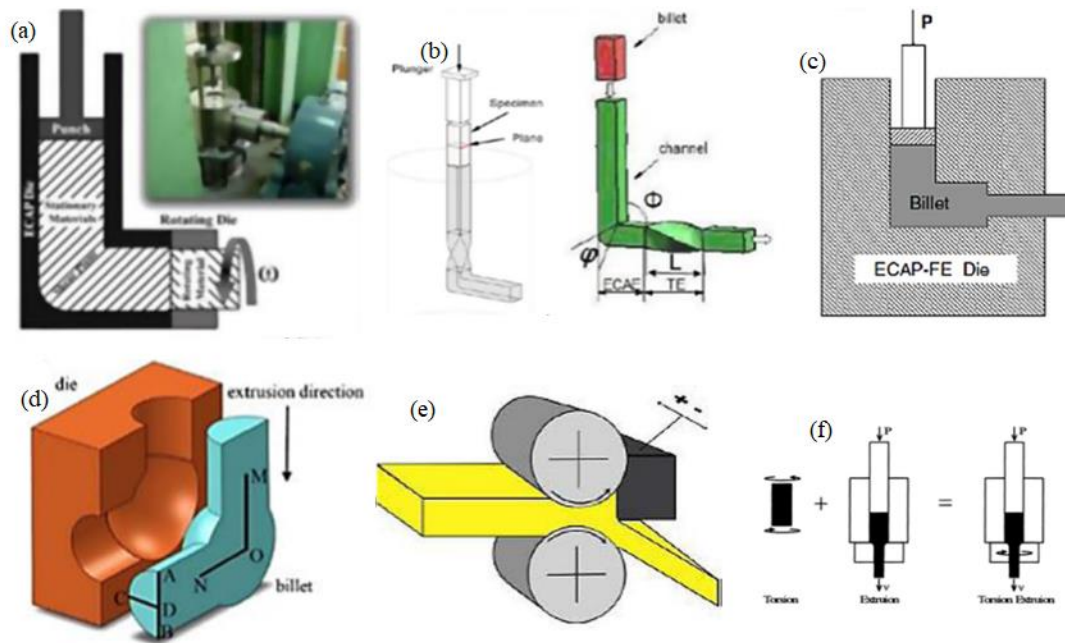


Figure 2.7 Classification of SPD technique based on rolling method (Bagherpour et al. 2018)

## 2.6 Applications of SPD

SPD requires large investments to commercialize the process, and it has limitation with respect to material, dimension, material waste and many more. According Honeywell Electronic Materials (USA), for physical vapour depositions, ECAE method was used to scale up the production of sputtering targets to retain strength and ductility. This method was assured to work on low alloyed, high purity material, such as, Cu, Ti and Al, in manufacturing of sputtering targets (Ferrasse et al., 2008). In bio medical implants, such as knee, hip, dental implants, SPD processed Ti and its alloys are used, because Ti alloys possess high corrosion resistance and intrinsic bio-capability. Pure Ti possesses low strength and fatigue life, which had restriction to load bearing implants. Ti-6Al-4V was used as reinforcement implant material, in most of the cases, but it has a risk of toxicity, because of the presence of alloying elements. Two implant having diameter 2.0 and 2.4 mm of Ti, processed for ultra-fine grains was installed to a patient, and showed good results. Metal crowns were fixed on the installed implants after six weeks (Smolin et al. 2014).

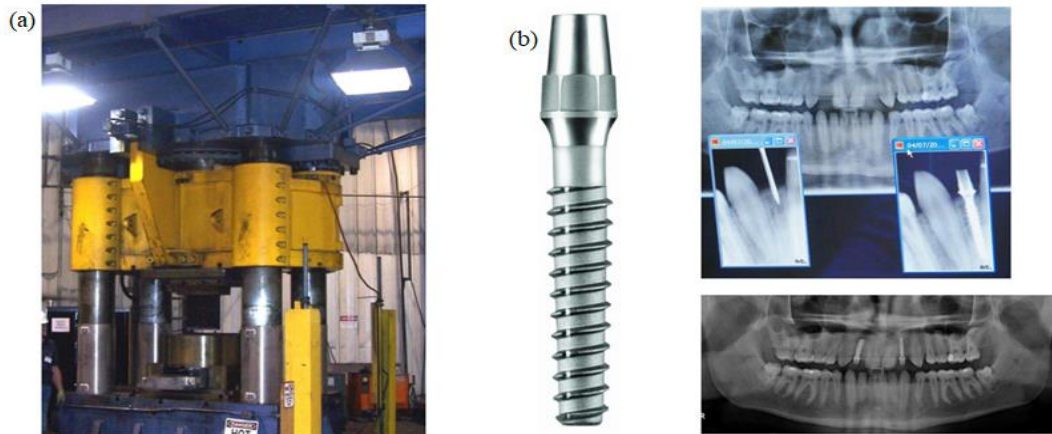


Figure 2.8 (a) Commercial ECAE die with 4000 ton capacity (Honeywell Electronic Material-2008) (Ferrasse et al. 2008) and (b) ECAP processed pure Ti dental implant, used to install metal ceramic crown (Smolin et al. 2014)

## 2.7 Equal channel angular pressing (ECAP)

Segal (1980) introduced high strain in metal billets by simple shear. Potential advantages of ECAP were documented in early 1990s, where production of ultra-fine grains with unique characterization were attracted by scientific community. Figure 2.9 (a) shows schematic ECAP die with channel abrupt angle  $\Phi = 90^\circ$ , and curvature angle  $\Psi = 0^\circ$ . When samples are processed through die, simple shear was expected. Due to imposed deformation, no change in cross section was observed, after pressing. ECAP was characterized by several parameter such as, strain imposed while pressing, slip system during operation and shearing patterns.

### 2.7.1 Strain Imposed during ECAP

Large abrupt strains were imposed during ECAP, at  $\Psi = 0$ , element abcd passes through theoretical shear plane, which deform, as shown in figure 2.9 (b-1) to element a'b'c'd' Shear strain,  $\gamma$  is given as

$$\gamma = \cot(\Phi/2) \quad (2-4)$$

Using similar approach, shear strain  $\gamma$  at  $\Psi = \pi - \Phi$  (figure 2.9 (b-2)) and  $\Psi =$  arbitrary value in between 0 and  $\pi - \Phi$  are.

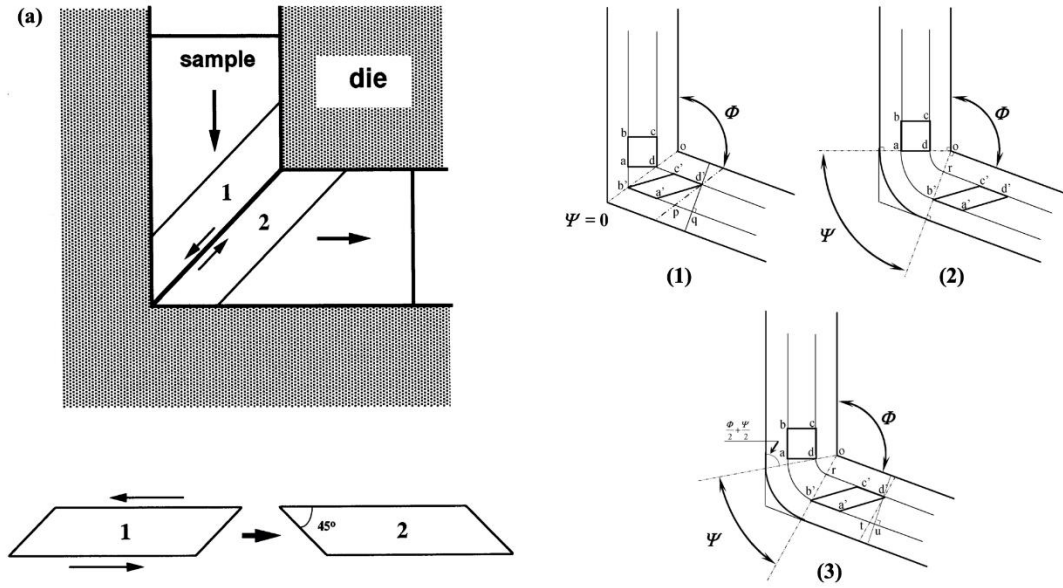


Figure 2.9 (a) Principle of ECAP, shear plane inside the die, acting on specimen: element 2 is transposed of element 1 due to shearing inside the die (Horita et al. 2010). (b) ECAP with different arc of curvature at point of intersection: (1) (a)  $\Psi = 0$ , (2)  $\Psi = \pi - \Phi$  and (3)  $\Psi = 0 < (\pi - \Phi)$  (Ruslan et al., 2006)

$$\gamma = \Psi \tag{2-5}$$

$$\gamma = 2 \cot(\Phi/2 + \Psi/2) + \operatorname{cosec}(\Phi/2 + \Psi/2) \tag{2-6}$$

Equivalent strain after N passes  $\epsilon_N$  was expressed in general form as

$$\epsilon_N = \frac{N}{\sqrt{3}} [2 \cot(\Phi/2 + \Psi/2) + \operatorname{cosec}(\Phi/2 + \Psi/2)] \tag{2-7}$$

Characterization of equivalent strain  $\epsilon_N$ , with different intersection angle  $\Phi$  from 45 to 180°, for angle of curvature 0 to 90° is shown in figure 2.10 for 1 pass ECAP.

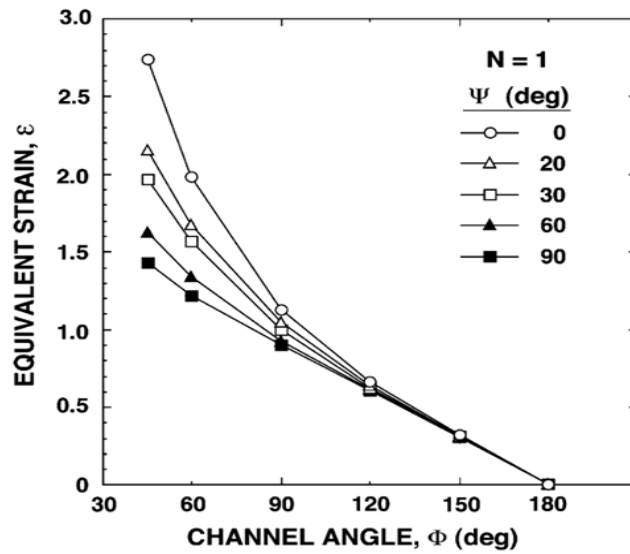


Figure 2.10 Characterization of Equivalent strain  $\epsilon_N$ , with angle of intersection  $\Phi$  and curvature angle  $\Psi$  (Ruslan et al., 2006)

### 2.7.2 Processing routes of ECAP

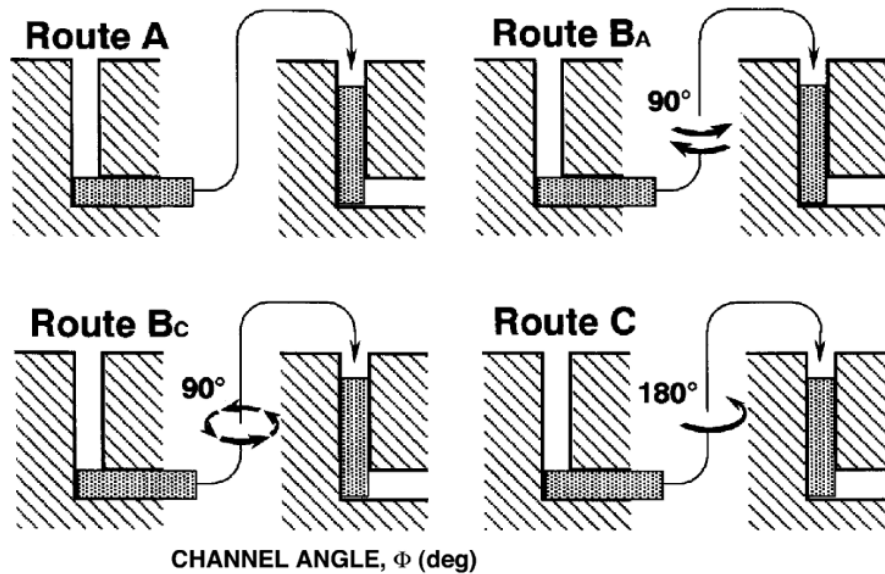


Figure 2.11 Different routes of ECAP processing (Horita et al. 2010)

Four standard routes (figure 2.11) were identified for ECAP processing, which induce different slip systems for grain refinement. In route A, sample was pressed without rotation at successive pass. In routes B<sub>A</sub>, B<sub>C</sub> and C, samples were rotated by 90° alternatively, rotated 90° in same direction and rotated by 180°, respectively.

Combination of routes are also possible to achieve good efficiency, and may lead to poor refinement based on selected routes.

### 2.7.3 Slip system associated with different processing routes

Slip planes associated with different processing routes are shown in figure 2.12 (a), Planes labelled as 1 to 4, are the slip planes corresponds to 4 passes. With route C, shearing occurs in same plane with successive passes, and shear direction is reversed after each pass. Hence, route C is termed as redundant strain process, and restoration of strain occurs at every alternate (even) passes. Route B<sub>C</sub> also showed same behaviour at every alternative pass, such as slip in first pass is cancelled by third pass and slip in second pass is cancelled by 4<sup>th</sup> pass. Route A and B<sub>A</sub> are not redundant, because, two different shearing planes are intersecting at 90°, and four different routes were intersecting at 120° respectively (figure 2.12 (b)).

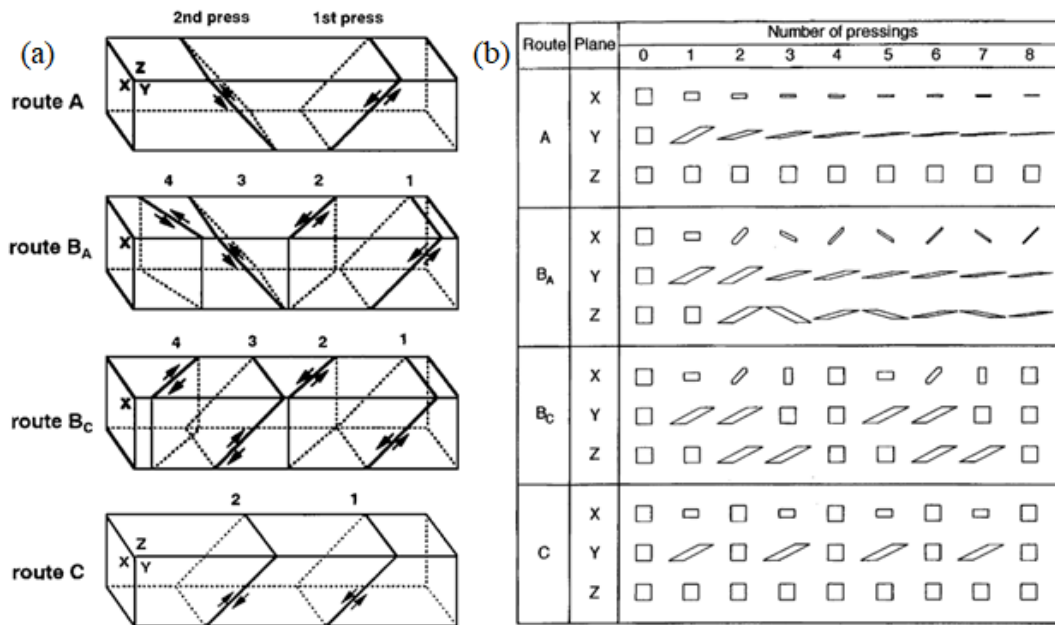


Figure 2.12 (a) slip planes associated with different routes for ECAP processing and (b) flow of slip planes under different processing routes (Horita et al. 2010)

### 2.7.4 Factors affecting ECAP

Channel angle  $\Phi$ , angle of curvature  $\Psi$ , strain rate  $\dot{\epsilon}$ , operating temperature  $T$  and influence of back pressure are the major influential factors on ECAP experiments. Factors, other than back pressure, will be explained in different section of this chapter.

Back pressure enhances the homogeneity of grains and workability of processed samples, which avoids the formation of cracks at sample surface.

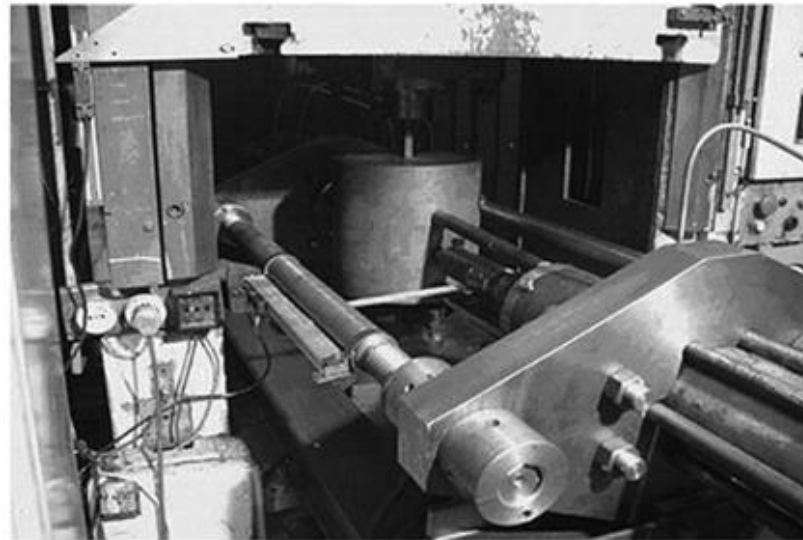


Figure 2.13 Experimental die setup with back pressure setup, two punches were used in setup where the first punch is used for the pressing the sample inside the die, and second punch controls the back pressure (Ruslan et al., 2006)

### 2.7.5 Mechanism of grain refinement

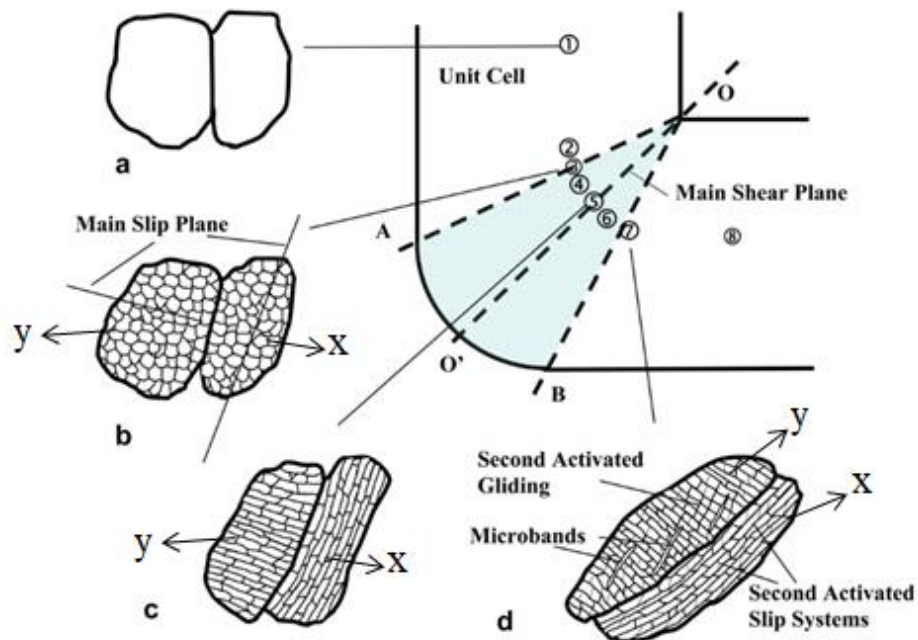


Figure 2.14 Schematic representation of evolution of microstructure during first pass (Xue et al., 2007)

In figure 2.14(a), grains before reaching the main slip plane (MSP) maintains zero deformation, as it advances to shearing area, many random dislocations are induced. Application of further strain, leads to formation of isotropic dislocation cell as shown in figure 2.14(b). After this stage, grain refinement initiates differently for each grain, based on its initial orientation. In figure 2.14(b), activation of slip plane for right grain (x) starts early, which is close to MSP, and activation of slip plane for left grain (y), starts at higher angle of MSP. These active planes cause integration of cell walls, straighten and self-organized gliding occurs along primary slip planes. It leads to construction of elongated laminar structure (ELS), these gliding of dislocations group wipes out the dislocations from original cell walls and leads to thinning of ELS boundaries by further deformation (figure 2.14 (c)). After formation of initial laminar structure, spacing between the laminar structures was stable and constant, due to which the refinement of spacing becomes harder with further deformation. For left grain (y), shear deformation along MSP initiate the slip in planes, which are closely aligned to MSP, and represents the change in slip activity, compared to right grain in figure 2.14(d). Initial ELS were segmented by ELS parallel to newly initiated slip and/or secondary microbands, and this is more efficient for refining substructure than right grain.

## **2.8 Surface Modification**

Surface topography is an important parameter for structural performance, material surface can be modified for different aspects, such as fatigue performance, corrosion resistance, roughness and many more. Mechanical surface treatments are based on cold working treatments at surface levels, which causes elasto-plastic deformations. Residual stresses were induced and surface layers were work hardened. Importance of surface modification is to enhance functionality of a component by changing surface characteristics. Fatigue cracks typically, initiate at surface under cyclic loading. Surface roughness, residual stress, hardness, surface microstructure and its properties were major factors for crack initiation and propagation while failure. Some of the surface modification techniques are shown in figure 2.15.

Deep rolling generates plastic deformation, by inducing deeper and larger compressive stress on surface, by application of contact pressure from a hydrostatically controlled roller. Surface roughness was improved, which was better than other surface

modification techniques. Burnishing is a similar process, where the tool diameter is smaller and produces better surface finish.

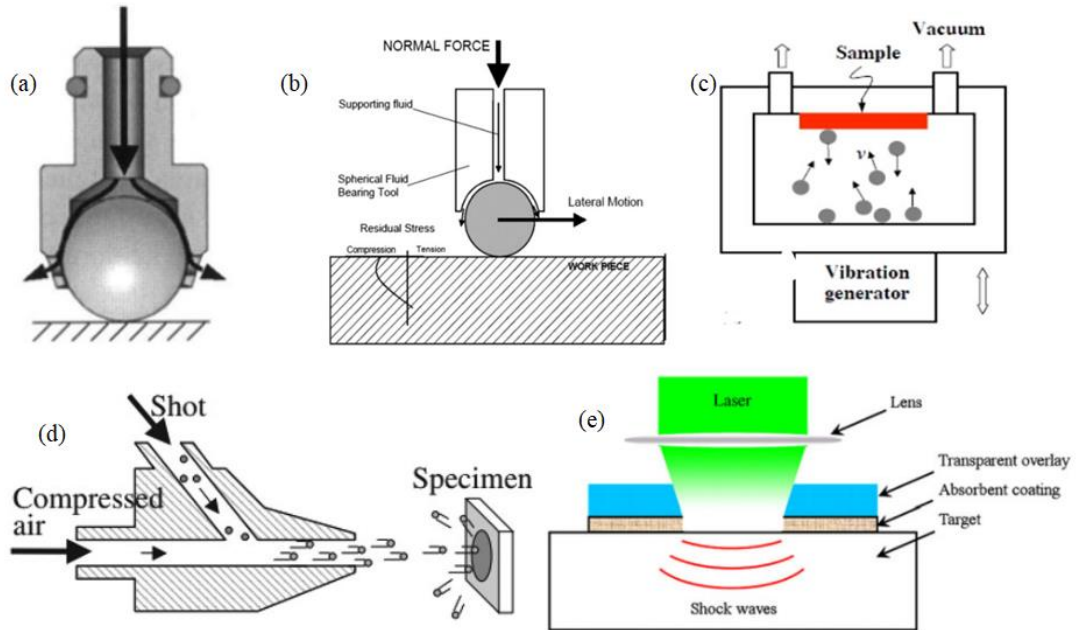


Figure 2.15 Surface modification techniques (a) Deep rolling, (b) low plasticity burnishing, (c) ultrasonic peening, (d) shot peening and (e) laser shock peening (Zhang et al., 2019)

Shot peening is a well-known method of inducing compressive residual stress in a material surface and it will contribute to increase in fatigue strength. It is a cold working process, where tiny hard spherical balls are bombarded on target material to create surface indentation. These indentations are formed due to local plastic deformation, and induce compressive residual stresses in surface. Indentation shape and residual stresses distribution are different from static indentation to dynamic indentation (Kobayashi et al. 1998). An ultrasonic vibration with certain amplitude is applied on work piece with spherical media. Intensity of surface modification depends on frequency, amplitude and diameter of media used for peening. Sample surface is uniformly processed by force applied through ultrasonic tool and generates nanostructured layer.

## 2.9 Laser shock peening

Figure 2.16 shows the schematic representation of laser shock peening. When small area of metallic surface is exposed to laser beam (produced by Nd-glass with high energy) pulse for short duration, surface layers melt and vaporize transiently. This



results in generation of high temperature (greater than 10,000 °C) and high pressure plasma (in the range of several GPa). These pulsed high pressure plasma induces intensified shock waves for shorter duration, and creates elasto plastic deformations (Mixte et al., 1995). As the laser beam passes through absorptive layers, most of the energy was absorbed by opaque layer and very thin layer of top surface of material get vaporized: surrounded thermal effects has neutralized and remain part of energy is added to plasma and its start expanding rapidly. These expansions are converted into high pressure shock wave for inducing deformations.

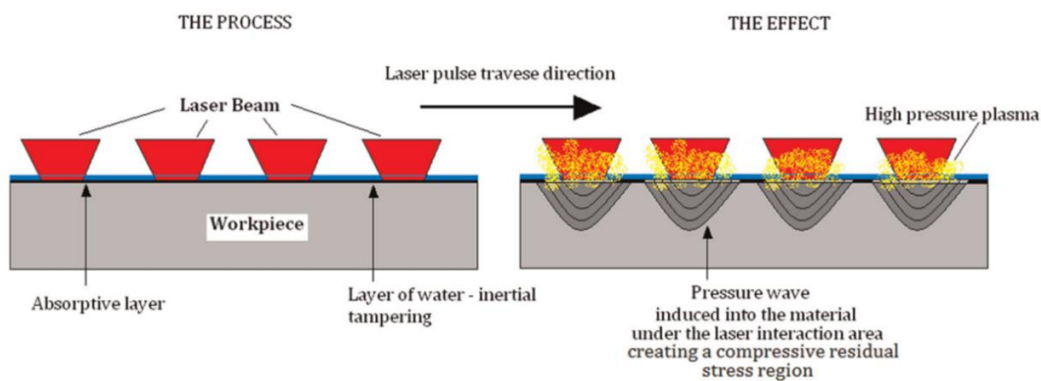


Figure 2.16 Schematic representation of laser shock peening (Shukla et al. 2014)

## 2.10 Advantages of plastic deformation

Materials, exposed to working environments, have tendency to corrode and this corrosion rate enhances in presence of tensile residual stresses. As LSP induces compressive residual stresses at surface, it prevents stress corrosion cracking and improves reliability of component. Work hardening, at surface layers enhances hardness and improves wear resistance at surface layer, LSP has more advantages with impact zone and size. An induced compressive residual stress enhances fatigue life by delaying the crack initiation at surface.

LSP has more penetration capacity to induce deeper residual stresses, compared to shot peening, hence more delay in failure of components. It doesn't have any physical contact during operation, and there is no wear and tear of tool. Accuracy of LSP is more as it works with computer controller, which leads to minimal defects.

## 2.11 Literatures

Nieh and Wadsworth (1991) explained the effect of Hall Petch Equation for nano grains. It was well proven that, as grain size decreases, strength and hardness increase. Some of the investigations are reported in favour of Hall Petch Relation and some

adverse to it. In reality, strength cannot be increased infinitely by decreasing grain size and it cannot exceed the theoretical value. Relaxation process, at grain boundaries of a critically small grains, leads to decrease in strength (figure 2.17). As grain size decreases, it reaches the size where individual grain cannot support more than one dislocation. In other view, when grain size approaches zero, it changes crystalline to amorphous, and no more grain boundary strengthening, and amorphous material shows lesser strength compared to crystalline material.

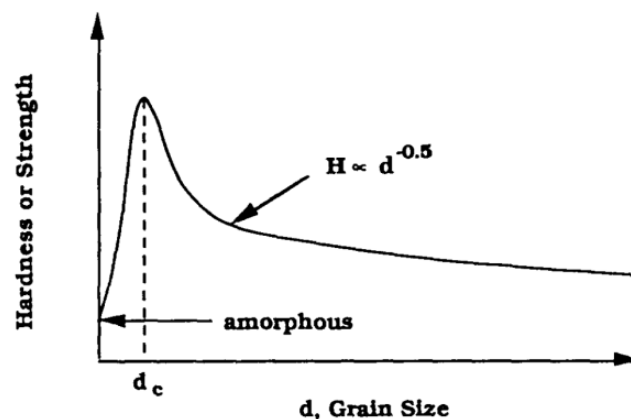


Figure 2.17 Effect of grain size on strength of a material (Nieh and Wadsworth 1991)

Lee et al., (2000) investigated the effect of Al, Zr, Sr, Si and Ca on magnesium. Addition of 5% weight of Al reduces grain size of Mg, and there was not much change in grain size, with further increase in Al content. Effect of addition of Sr (Strontium) was studied on low and high content of Al on Mg alloy- Low Al alloy showed positive effect of grain refinement, but, high Al content (Mg-9Al) doesn't offer any change in grain size. Zr (Zirconium), Si (Silicon), and Ca (calcium) showed efficient grain refinement and was achieved by controlling grain growth (figure 2.18). Particles added during alloying, or secondary phase formed, due to alloying components, acts as a nucleants for formation of grains. Increase in nuclear density enhances the quality of grain refinement.

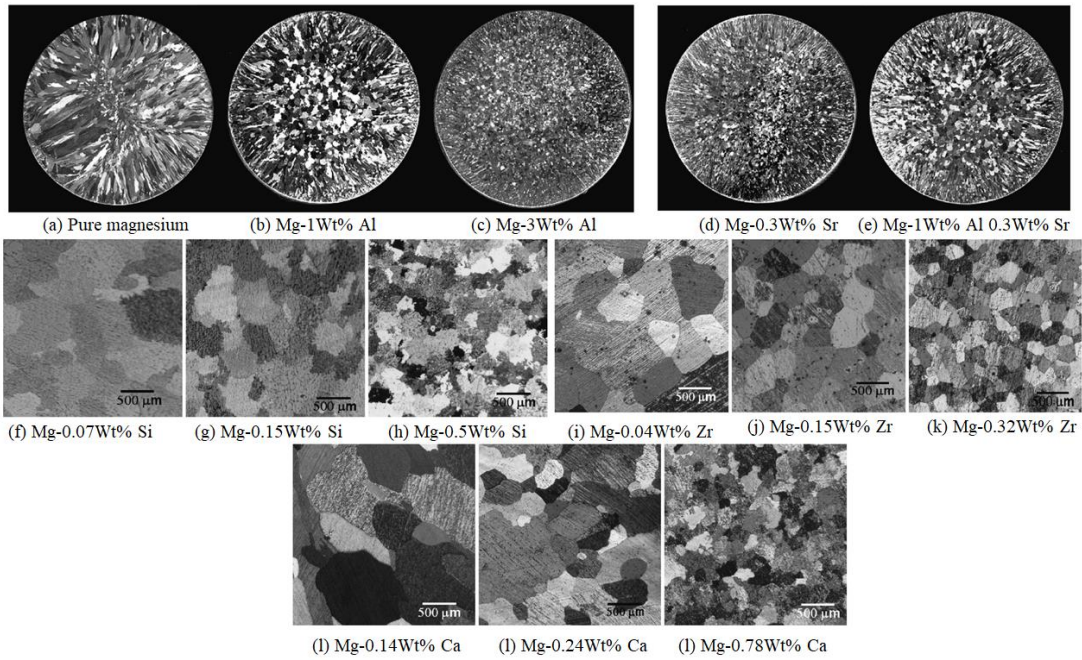


Figure 2.18 Magnesium grain refinement by alloying (Lee et al., 2000)

Eisenmeier et al. (2001) investigated the behaviour of cyclic load on magnesium alloy (AZ91), cast in vacuum die. Fatigue test was executed between constant strains ( $1.4 \times 10^{-3}$  and  $2 \times 10^{-2}$ ), at room temperature and at  $130^\circ \text{C}$ . Microstructures of fractured surface were investigated, which revealed crack initiation, at cavities or extreme surface, and propagated through trans-dendritically and inter-dendritically. Cracks were closed at small compressive mode and opens at tensile mode of cyclic load (figure 2.19).

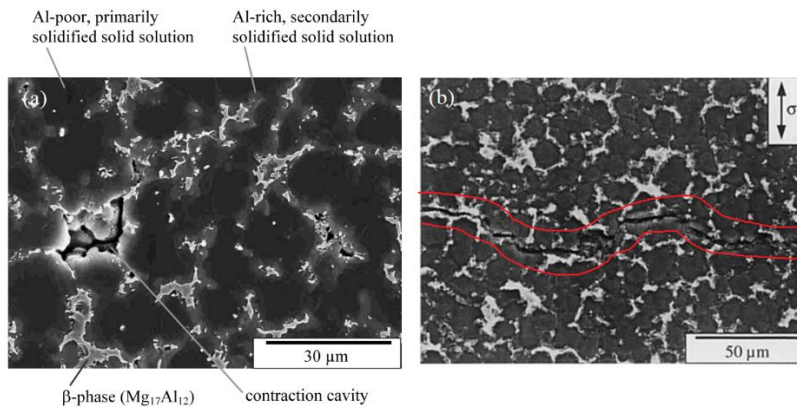


Figure 2.19 Microstructure of AZ91 with (a) cavity and (b) crack propagating inter dendritic and trans dendritic (Eisenmeier et al. 2001)

Wang and Fan (2006) investigated cracking mechanism of small fatigue cracks on AM50 magnesium alloy. Experiments were carried out at different temperature and vacuum pressure. Crack growth rate increased with increase in temperature, which was propagated through dendritic and interdendritic cells (figure 2.20).

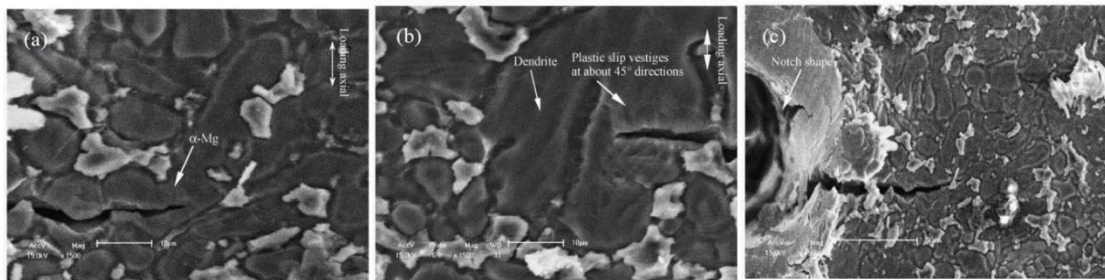


Figure 2.20 SEM images of fatigue crack growth at different loading on AM50 (a)  $\sigma_{max}$  128 MPa, TZ150 8C, NZ4109, (b) plastic slip vestiges near crack tip at  $\sigma_{max}$  125 MPa, TZ150 8C, NZ5819 and (c) notch shape at  $\sigma_{max}$  128 MPa, TZ150 8C, NZ4260 (Wang and Fan 2006).

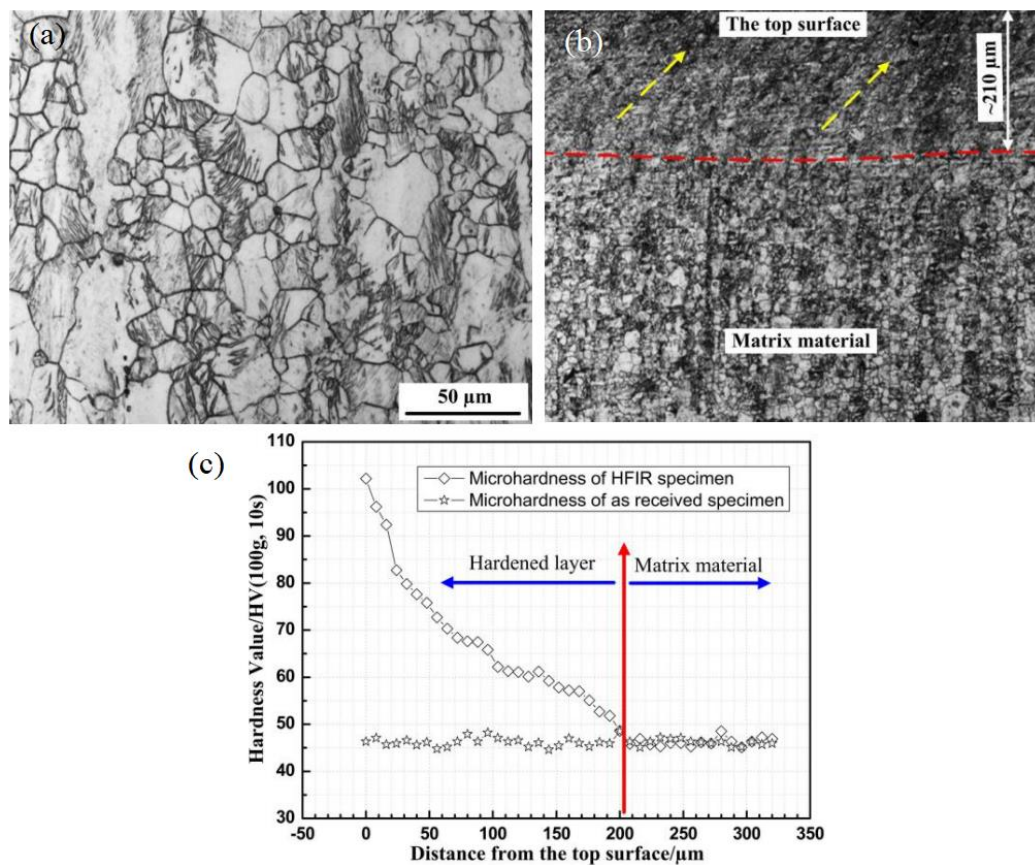


Figure 2.21 Microstructure of (a) AZ31B, (b) AZ31B treated with HIFR and (c) cross sectional microhardness of as received and HIFR treated sample (Zhao et al., 2017)

Zhao et al., (2017) processed magnesium alloy AZ31B by HFIR (High frequency impact and rolling) to gain differential nanograined surface. HFIR was carried out on samples of uneven equiaxed grains, with an impacting frequency of 27 kHz, amplitude 7.0  $\mu\text{m}$ , rotating sample at speed of 110 rev/min. Effects of HFIR were analysed through fatigue testing at room temperature and stress ratio (R) of 0.5. Grain refinement, work hardening, compressive residual stress, smooth surface and average grain size of 20 nm and 28 % of increase in fatigue were observed after HFIR, at near surface (figure 2.21).

Gopi et al., (2016, 2017a, 2017b) extensively worked on AM series magnesium alloys and characterized for microstructure and strength after processing using ECAP under route B<sub>C</sub>. Grain size reduced from 100  $\mu\text{m}$  for as-received to 1  $\mu\text{m}$ , after 4 passes. EBSD analysis revealed change in misorientation angle and occurrence of high angle grain boundaries, due to ECAP. Samples after 2 passes of ECAP showed highest tensile strength, because of grain boundary strengthening. Higher ECAP passes showed reduced strength, which was because of dynamic recrystallization. Wear studies revealed decrease in co-efficient of friction, with increase in ECAP passes and was verified by hardness test.

Kulyasova et al. (2009) investigated microstructures and fatigue properties of AM60 Magnesium alloy processed by ECAP and found grain size reduced to less than 1  $\mu\text{m}$ . Tensile strength increased to 310 MPa, without losing ductility and fatigue endurance limit increased by 70 %. TEM investigations revealed additional twinning and grain growth before fatigue tests,  $\gamma\text{-Al}_{12}\text{Mg}_{17}$  showed fatigue induced twinning.

Biswas et al. (2011) investigated experimentally, the evolution of microstructure and texture, during extrusion of pure magnesium and AM30 magnesium alloy and characterized by EBSD and X-ray diffraction. During initial stages, grain size of 1000 and 200  $\mu\text{m}$ , were observed, and they were refined to 18.6 and 10.4  $\mu\text{m}$  in extruded rod samples. There were high fraction of low angle grain boundaries and diffused high angle grain boundaries. Same texture was observed for both (rod and tube) samples, with basal plane along the periphery of pole figure.

Akbaripannah et al. 2013 investigated fatigue behaviour and crack propagation rate of AM60. Grain size reduced from 19  $\mu\text{m}$  to 2.3  $\mu\text{m}$ , after 6 passes of ECAP at 220 °C.

Yield strength and ultimate strength increased till 2<sup>nd</sup> pass and start decreasing with higher number of passes. Strength reduced due to softening effect of texture anisotropy. Good fatigue behaviour was observed after 2<sup>nd</sup> pass of ECAP and concluded that 2 pass ECAP specimen was the better choice, compared to multiple pass ECAP sample of AM60, for fatigue applications. Striation type and brittle type patterns were observed in fractography test of 2<sup>nd</sup> pass ECAP sample, and it was shown that bi-modal grain structure was present because of the presence of coarse and fine grains (figure 2.22).

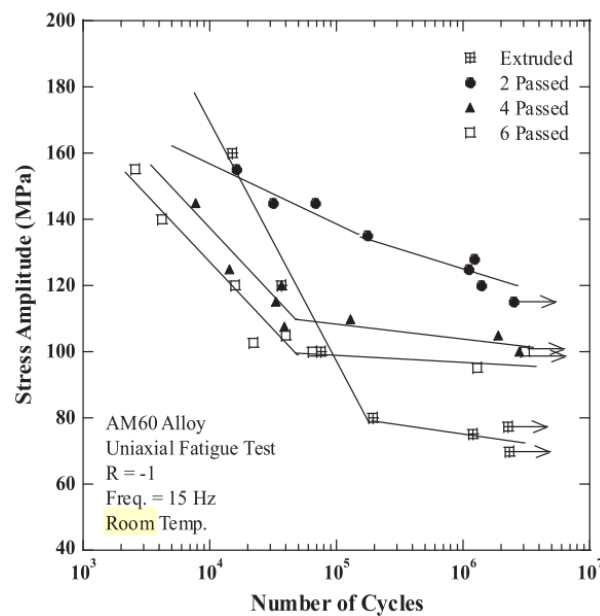


Figure 2.22 Fatigue characterization of AM60 processed by ECAP (Akbaripannah et al. 2013)

Peyre et al. 1996 worked on laser peening to demonstrate improvement in fatigue behaviour of aluminium alloys. Laser peening was compared with shot peening, for high cyclic fatigue behaviour, on aluminium. Intense laser sources having energy density greater than 1 GWcm<sup>-2</sup> was used for peening of Al2Si, A356 and 7075 alloys. Residual stresses were measured by hole-drilling method for both shot peening and laser peening. Peened surfaces showed superior hardness compared to non-treated surface. Laser peened surface showed better penetration of residual stresses. Fatigue life of laser peened surface promised better life compared to shot peened.

Wagner 1999 studied mechanical surface treatments to induce high dislocation densities in near-surface region by shot peening, roller burnishing and deep-rolling on

Ti, Al and Mg alloys. All mechanical surface treatments resulted in changes in surface roughness, which increased in near surface dislocation density and development of residual stresses. Surface roughness accelerated crack initiation and there was no effect on crack propagation. Cold work accelerated crack propagation, but no effect on crack initiation. Residual compressive stresses had minimum effect on crack initiation, but very large advantage to stop crack propagation. Mg alloy AZ80, processed by shot peening, showed improved fatigue life, at low intensity of peening. Increase in shot peening intensity, showed more crack nucleation.

Hammersley et al. 2000 reviewed laser processing on surfaces, pre-stressed to improve fatigue life of components. Solid state lasers produced short pulses of energy in the form of beam. Neodymium doped glass exhibited better combination of high energy short pulse for peening applications compared to Co<sub>2</sub> lasers. Surfaces, treated with black coating, enhanced laser absorption co-efficient and produces good results. Plasma shock wave produced, due to impact of laser pulses, induced compressive stresses on surface. These pulses can be overlapped to achieve better results in controlled manner and laser peening had better depth penetration compared to shot peening.

Yoo et al. 2001 explained the importance of non-basal slip systems in hexagonal close packing (HCP). Critical situation occurred when C-axis of crystalline grain was oriented parallel to the direction of uniaxially applied stress and was named as “hard orientation”. Non-basal  $\langle c+a \rangle$  pyramidal slip and/or deformation twinning were required for deformation. Hence, any HCP crystal allowing pyramidal slip  $\langle c+a \rangle$ , obeyed Von Mises Criterion for homogeneous plastic deformation. Stacking fault energies for basal, prism and prismatic systems influenced non basal slip.

Dahle et al. 2001 reviewed grain size of Mg-Al alloy for different Al percentage (figure 2.23). Most of the Mg alloys were based on Mg-Al content for their proven compatibility, cost effective and showed good mechanical properties. Increase in Al content resulted in the formation of dendritic structure. Grain size was dependant on cooling conditions, alloy composition and type of nucleant particles present.

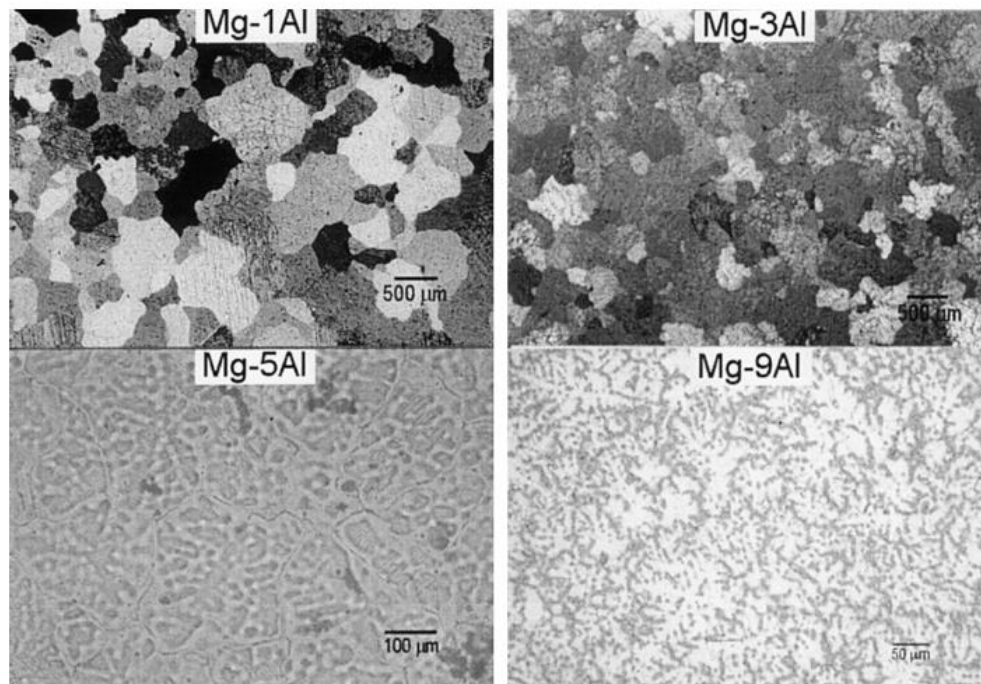


Figure 2.23 Microstructure of Mg-Al alloy with increase in Al content (Dahle et al. 2001)

Yamashita et al. 2001 conducted experiments to evaluate strength of Mg and Mg-Al alloy at room temperature, processed by SPD. ECAP was chosen as the simplest method of SPD and it can be executed at elevated temperature, and pressing was done at different temperature (200 °C, 300 °C and 400 °C). ECAP, at low temperature, resulted in fine grains, and at high temperature, resulted in coarse grains. As the number of passes increased, grain size reduced, because of dynamic recrystallization with improved strength and ductility.

Koike et al. 2003 investigated tensile behaviour of rolled AZ31 sheets at different temperatures from room temperature to 523 K. There were some locations on the alloy, having fine grains, showing increased elongation (47%) at higher temperature compared to room temperature. Grain refinement had positive effect on grain boundary sliding (GBS) in nano scaled grains. GBS strain was calculated from the measured surface step height, and its temperature dependence was analyzed by a Dorn-type constitutive equation. Fracture strain increased with increase in temperature and decreased tensile strength. Surface morphology was explained by considering the effects of GBS and proved that increase in temperature increased GBS.



Barnett et al. 2004 studied the effect of grain size varies between 3  $\mu\text{m}$  to 23  $\mu\text{m}$  Mg-3Al-1Zn alloy. Role of twinning was observed at room temperature. With the help of slip domination at higher temperatures, stress flow behaviour switched from compression to tension, due to activation twinning. As temperature increases, yield strength decreases, and becomes constant in both tension and compression, due to activation of prismatic/pyramidal slip systems. CRSS dropped rapidly, due to which compression strength increased with decrease in grain size at room temperature, which may be due to change in degree of twinning. Reverse 'Hall Petch' effect was observed at high temperature compression.

Valiev et al. 2006 discussed the development of ECAP during last two decades and further discussed the effect of ECAP on grain structure of different materials. Role of all fundamental and experimental parameters of ECAP process was demonstrated and effects were reported. Shear mechanisms of grains were explained and the effects of channel angle  $\Phi$  and curvature angle  $\Psi$  were discussed. Effect of strain rate was one of the key parameters to achieve good results. ECAP, at elevated temperatures, is needed for HCP structures to activate additional slip systems. Further, ECAP of metal matrix composites was discussed.

Hong et al. 2008 discussed computational modelling of shot peening as elasto-plastic, with discrete elements method being used for multiple impacts. Axis-symmetric FE model was developed to avoid computation time and validated with Meguid et al. 1999. Hong reported good agreement with the results obtained by Meguid, which were more realistic. Effect of process parameters of shot peening with simulations were studied. Discrete element modelling of shot stream was simulated to study multiple shot impacts. Data of each shot was accumulated, before and after collision.

Bagheri et al. 2009 reviewed the effect of shot peening process to achieve nano crystalline surface and its importance. Fatigue fracture, fretting fatigue, wear and corrosion are the sources for engineering failure, which are rooted at the surface. All these parameters showed better improvement after inducing nano crystalline indentations through shot peening. Hence, shot peening is one of the promising methods to induce nano crystalline surface. Impact energy of the shot at contact of material had significant impact on inducing nano crystals and multiple impacts proven better results.

Easton et al. 2016 discussed recent trends in grain refinement of light metals and alloys, nucleant particles, alloying elements (solute), and their distribution in liquid metal, density of distribution. Effects of solidification process with different cooling models were discussed. Inoculation is normal process in metal casting industries, which led to impurities, local defects and formation of particle agglomerates. Main advantage of inoculation is grain refinement and is achieved by introducing external form of energy to liquid or semisolid state of alloy at certain level of frequency (dynamic solidification). Use of synchrotron real time, x-ray observation on nucleation and grain growth techniques are discussed.

## **2.12 Motivation for proposed work**

By observing the existing literature, light weight material still possess big challenges in terms of applications due to limited strength and reliability. It has been observed that, light metals and alloys have big advantages with respect to non-metallic composites at space, aerospace, bio medical industries and many more, as it directly proportional to inertia of the system.

- Mg is at-present, the lightest engineering metal, having advantage with respect to its specific strength. But, it has limitation due to its low mechanical strength at room temperature. Hence, further processing is required to improve strength.
- Grain size in metals and its alloys possesses a great role in characterizing its properties. Recent studies on grain size refinement and texture tailoring, proves advantageous in mechanical properties according to Hall-Petch equation.
- SPD technique such ECAP, refines the grain effectively throughout the specimen and there is a advantage of change in mechanical behaviour of processed material.
- AM series of Mg alloys offers excellent mechanical properties, corrosion resistance and ease of castability. Detail study on mechanical behaviour of AM series was studied by (Gopi et al., 2016; 2017a; 2017b).
- Surface treatment to induce compressive residual stress on substrate will enhance the surface hardness and delay in crack propagation.
- Combination of light alloy, Grain refinement and surface treatment will lead to better engineering material.

### **2.13 Objectives of Research**

The main objective of the research work is to combine two different SPD techniques to tailor the grains in AM80 alloy. Based on proposed work, there are many sub objectives and listed below.

- Microscopic studies on ECAP processed sample to investigate the effect of grain refinement.
- Mechanical characterization on ECAP processed sample to investigate the effect of grain refinement.
- Microscopic studies on ECAP and LSP processed sample to investigate the effect of grain refinement.
- Mechanical characterization on ECAP and LSP processed sample to investigate the effect of grain refinement.
- Characterization the effect of ECAP and LSP on residual stresses of material.

## CHAPTER 3

### METHODOLOGY

The procedure followed to execute the objectives of research is described here. Figure 3.1 shows the flow chart indicating the steps involved in conducting the experiments in the present work. Flow chart provides a brief idea about list of experiments and testing followed to carry out the proposed research work.

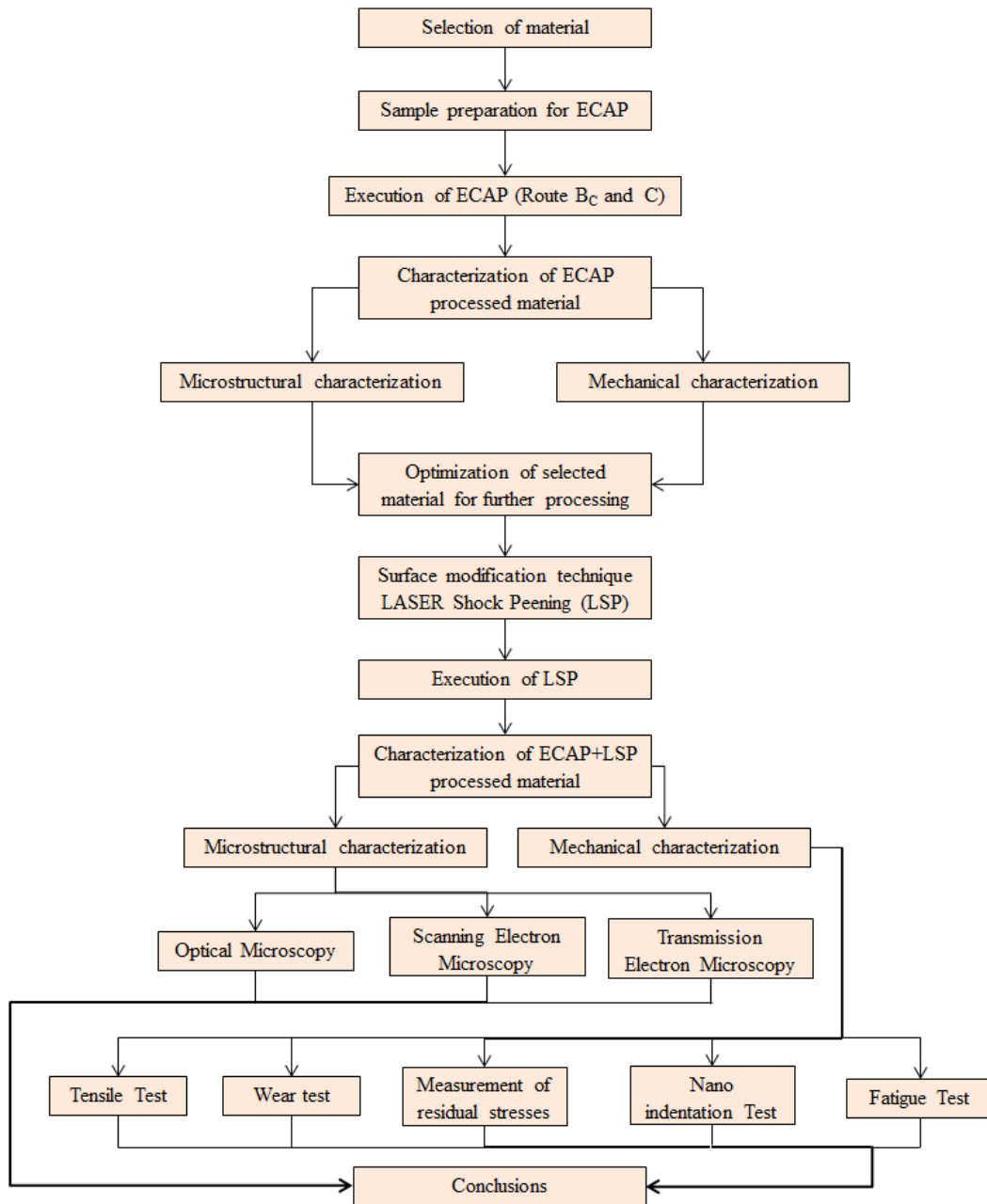


Figure 3.1 Flow chart for experimental procedure followed to conduct the experiments and testing

### 3.1 Material

Cast AM80 alloy was procured in the form of circular rod of diameter 20.0 and length 115.0 mm from Venuka Engineering, Hyderabad. Nominal composition of the alloy is shown in Table 1.

Table 1 Nominal Composition of AM80 Mg alloy (Wt.%)

Elements	Al	Mn	Fe	Cu	Zn	Mg
Wt.%	8.23	0.45	0.48	0.67	0.21	Balance



Figure 3.2 Cast AM80 rods in as received condition

As-received rods (figure 3.2) were homogenized for 24 hours at 350 °C, air cooled to room temperature after homogenization. Samples were further machined to diameter of 15.8 mm and length 97.0 mm (figure 3.3) for executing ECAP.

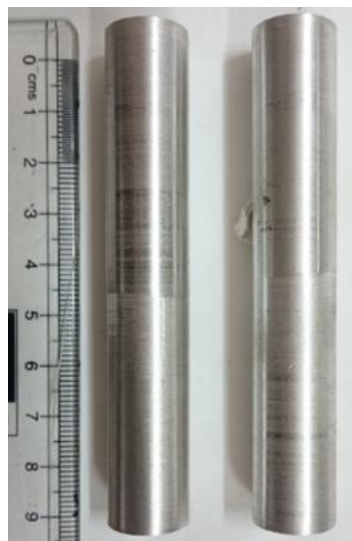


Figure 3.3 Machined sample of AM80 to execute ECAP

### 3.2 ECAP die setup and working procedure

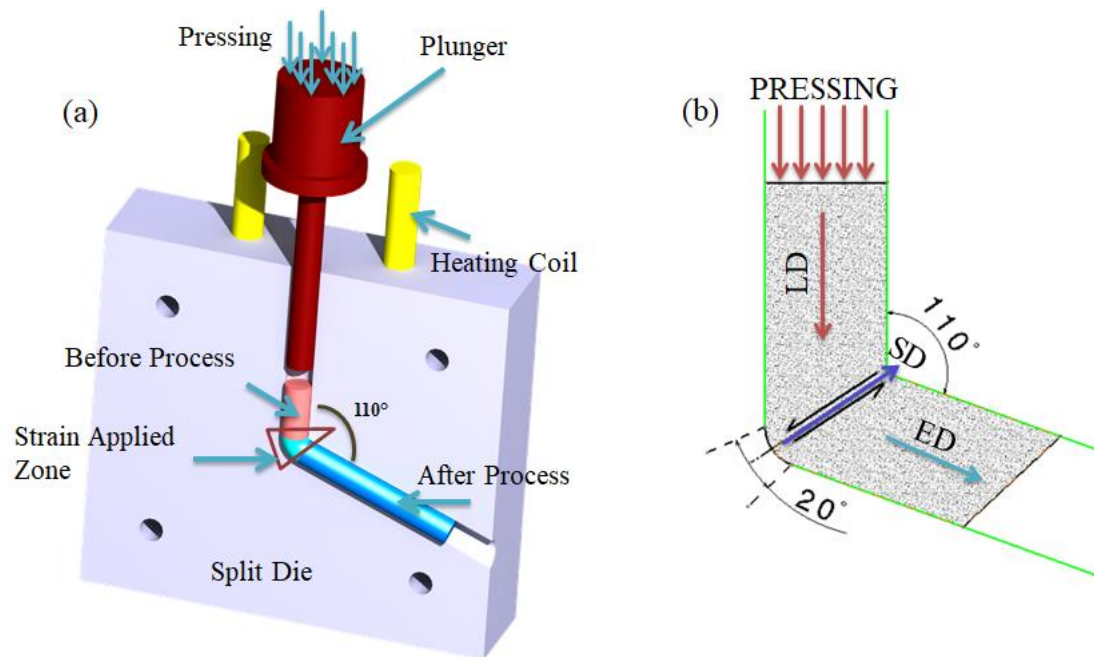


Figure 3.4 (a) Sectional view ECAP split die with heating coils and plunger, (b) Material flow mechanism during ECAP

Figure 3.4 (a) shows the schematic sectional view of ECAP split die with plunger, made of hard steel. It consists of two internal channel of diameter 16.0 mm, intersected at centre at an angle of 110°, separate holes are made to insert heating coils. Figure 3.4 (b) shows the schematic of material flow during ECAP, 40 Ton capacity hydraulic universal testing machine (UTM) was used for pressing.

### 3.3 Execution of ECAP

Magnesium alloy AM80 samples were lubricated (or dressed) with Molybdenum disulphide ( $\text{MoS}_2$ ) and inserted at inlet channel of die, heating coils were switched on to obtain required temperature ( $275^\circ\text{C}$ ). After reaching the required temperature, plunger was descended at inlet channel and pressed with a deformation rate of 0.5 mm. Die was disassembled to remove the sample. For higher passes, ECAP processed samples were dressed again, and rotating the sample by  $90^\circ$  with respect to longitudinal axis, between two subsequent pass, while inserting into angular channel of the die (route B<sub>C</sub>). This process was repeated for upto four passes, and complete setup is shown in figure 3.5.

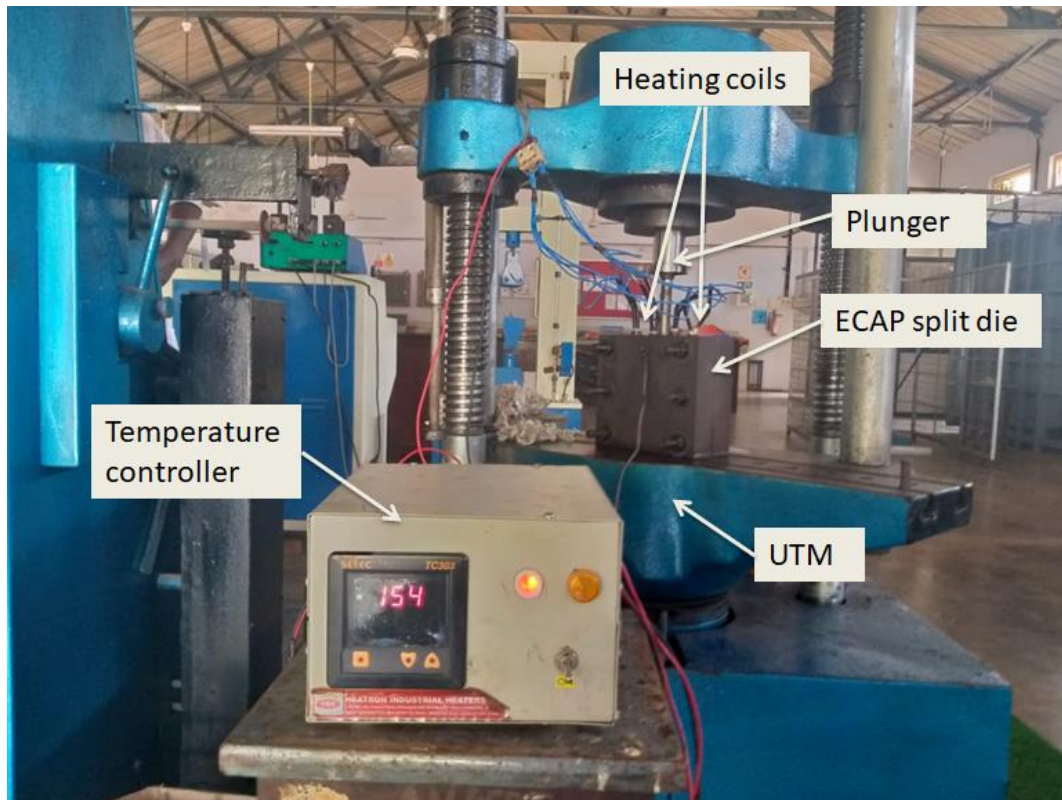


Figure 3.5 ECAP setup

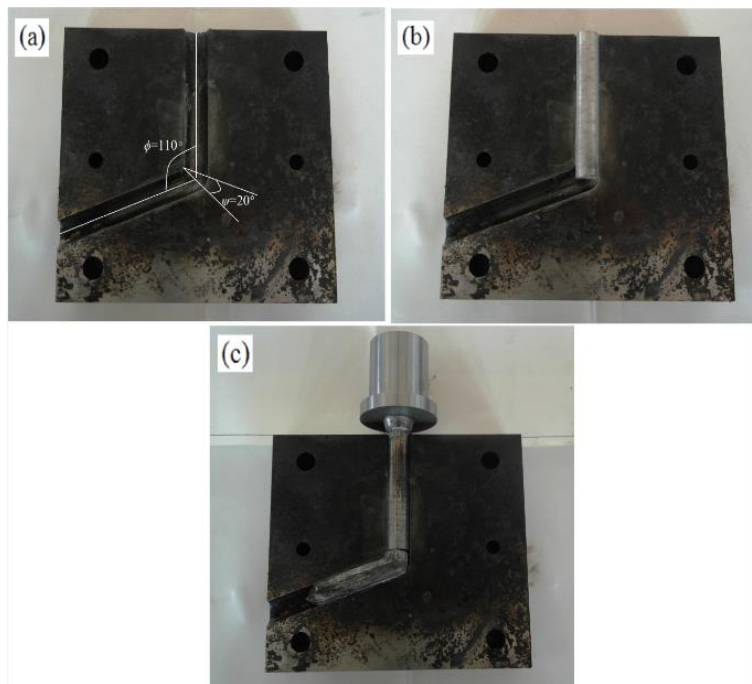


Figure 3.6 ECAP processed sample with processed sample. (a) Split die (b) split die with sample insertion and (c) processed sample with plunger



Figure 3.7 ECAP processed sample

### 3.4 Laser shock peening

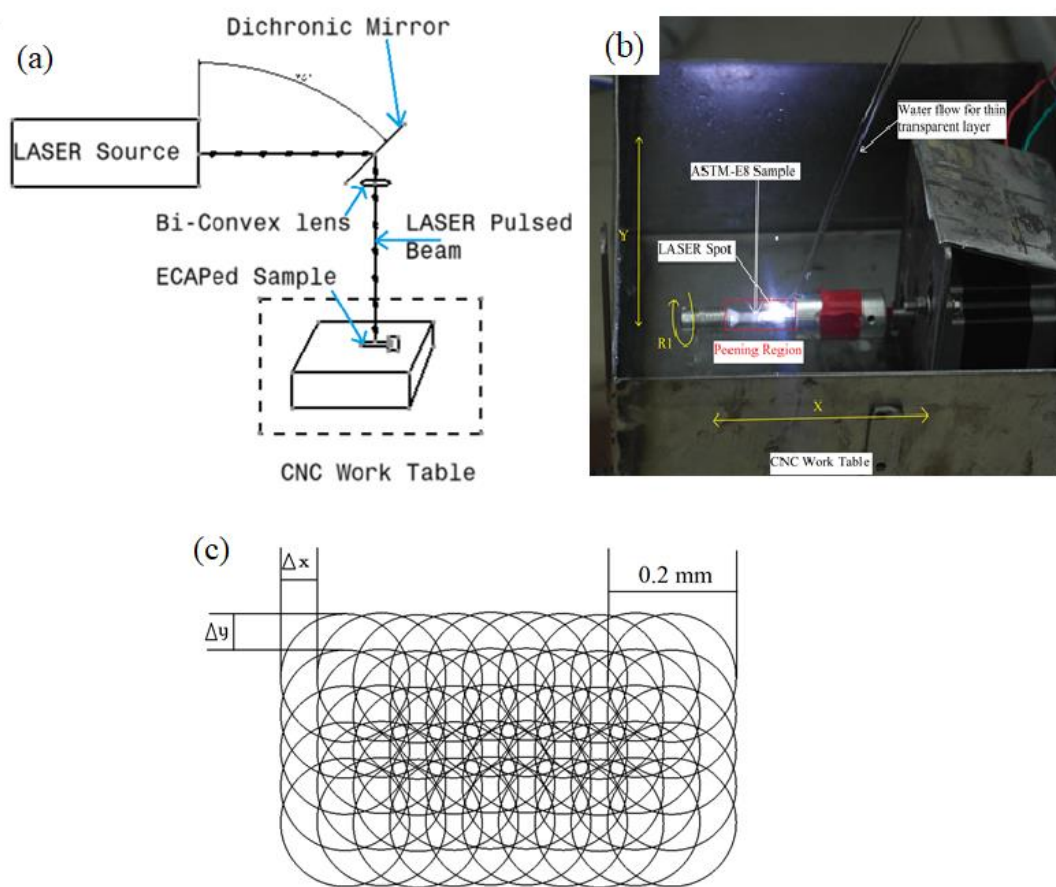


Figure 3.8 LSP setup (a) Schematic view of LSP setup, (b) view of work table, and (c) Laser pulsed spot of diameter 0.2 mm with overlapping parameter

LSP is surface modification procedure; hence, it carried out at after ECAP. Nd:YAG Laser, operated at wavelength 1064 nm with pulse duration of 10 ns, was used for LSP. Dichromic mirror was used to deflect the beam followed by convex lens, with a focal length of 758 mm (figure 3.8 (a)). Resulting beam had a spot diameter ( $D$ ) of 0.2 mm. Samples were placed on CNC controlled workstation to achieve required X, Y



(Translation: for plane samples) and X, R<sub>1</sub> (Translation and Rotation: for ASTM E-8 Samples) motions. Continuous water flow was supplied to achieve thin transparent layer on peened surface (figure 3.8 (b)). Peening area was covered with 70 % overlap ( $\Delta x, \Delta y, \Delta R_1 = D*0.3$ ), and peening was repeated for 100, 200 and 300 % of coverage at 8GWcm<sup>-2</sup> (figure 3.8 (c)). Figure 3.9 shows, processed sample after ECAP+LSP.



Figure 3.9 ECAP+LSP processed sample for material characterisation

### 3.5 Material characterization

Cross sections of as-cast and homogenised samples were extracted by cutting samples across the length. Cross-section of ECAP processed samples were extracted at middle portion, to avoid inhomogeneity through slow cutting metallurgical saw, and later polished with silicon carbide abrasive paper by machine polishing (figure 3.10) using emery papers of FEPA grade (ISO 6344) P100, P300, P600, P900, P1200, P1500, and P2000, followed by cloth polishing with diamond paste (0.25  $\mu\text{m}$ ) to obtain mirror finish at surface. Cross section of LSP processed samples were extracted by cutting the sample normal to peened surface to observe the peening effect, and further polishing was done with silicon carbide paper and diamond polishing. Picral acetate (4.5 grams of picric acid, 10 ml of acetic acid, 70 ml of ethanol and 10 ml of distilled water) was used as etchant to obtain metallographic information. Surface of polished samples were immersed in freshly prepared picral acetate for 3 to 5 s, washed with distilled water, cleaned with acetone and dried using air blower.



Figure 3.10 Mechanical disc polishing machine

### 3.5.1 Microstructure Characterization



Figure 3.11 (a) Optical microscope (Zeiss, Axiolab A1), (b) Scanning electron microscope (JEOL JSM- 7100F)

Microstructures were observed under optical microscope (OM), scanning electron microscope (SEM) and transmission electron microscope (TEM) and analysed. ZEISS-AXIOLAB A1 optical microscope (figure 3.11 (a)) was used to extract the microstructural images at different magnification, and images were analysed through

software to understand the grain behaviour at different level of processing. As the objective is to induce grain refinement, optical microscopic examinations are not sufficient to analyse the microstructures. SEM-JEOL JSM 6380LA (figure 3.11b) was used for further investigate grain structure. Energy dispersive x-ray spectroscopic results were extracted to analyse material composition. SEM was also used to study fracture behaviour of samples after destructive testing.

To understand further grain refining mechanisms, samples were analysed using TEM (figure 3.13), but sample preparation was quite challenging due to surface treatment, and expecting results near the surface. ECAP and ECAP+LSP processed samples were investigated by TEM, as the as-cast and homogenised sample possess larger grains. Sample preparation include following steps: cut the required portion of sample under slow speed diamond cutter to a thickness less than 0.5 mm, punching the sample to a diameter of 3 mm, thinning of the samples to a thickness of 100  $\mu\text{m}$  using silicon carbide paper of 1000 grade, and dimpled (figure 3.12 (a)) to achieve a thickness of around 10 – 15  $\mu\text{m}$ , before subjecting to ion beam polishing (figure 3.12 (b)) (Gatan-PIPS 691), perforations are made on the sample. LSP peened sample possess higher surface roughness at treated region, hence slow polishing has to be done. As magnesium is highly reactive with water, ethanol with diamond paste of 0.5  $\mu\text{m}$  is used during polishing and dimpling. TEM analysis was executed to observe ultrafine grains, dislocations and selected area electron diffraction (SAED).



Figure 3.12 Sample preparation for TEM (a) dimpling machine and (b) Ion beam milling machine

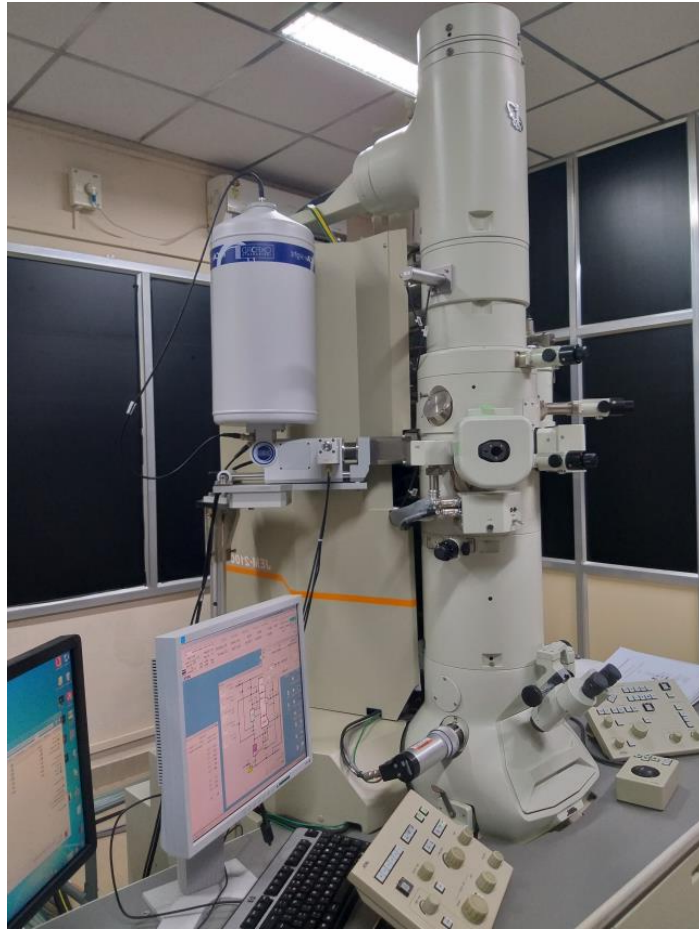


Figure 3.13 TEM facility (TEM-JOEL-JEM-2100)

### 3.5.2 Material phase and residual stress analysis using X-ray diffraction



Figure 3.14 X-ray diffraction unit (Panalytical-X'Pert<sup>3</sup>)

X-ray diffraction (XRD) analysis has been carried out to know the phases present in material. XRD peaks were observed at different inclination angles, with a step size of 0.001, with Cu K- $\alpha$  having wavelength of 1.54 Å, with a scan rate of 2°/min at room temperature. As SPD process results in huge deformation, it is very important to analyse residual stress existing in the sample before and after processing.

LSP is a well establish procedure to induce compressive residual stresses at surface level. Hence, estimating existing residual stress at every stage of process is necessary. Panalytical-X'Pert<sup>3</sup> (figure 3.14) is used to extract the X-ray Diffraction peaks. Incident x-rays at surface which follows Bragg's law ( $\lambda=2d \sin\theta$ ), induce diffraction peaks at stress free level, and these peaks will be shifted and broaden, based on the stresses present at the surface. Change in d-spacing is measured, which gives strain data, which is converted on stress value-based Hooke's law. Residual stresses diminished along the depth from surface. Perchloric acid and methanol in the ratio of 20:80, was used as electrolyte for electro polishing, and successive layers were removed for further measurement of residual stress.

### **3.6 Mechanical properties evaluation**

#### **3.6.1 Tensile characterization**

As-cast, homogenized and ECAP processed samples upto 4 pass were tested for tensile strength using Shimadzu AG-X plus<sup>TM</sup> (100 kN), Universal Testing Machine, with deformation rate of 0.2 mm/min. All tests were executed at room temperature (~25 °C), and samples were prepared according to ASTM-E8 (ASTM 2009) standards, with gauge length of 16.0 mm. Highest strength was observed in samples processed by ECAP for 2 passes and explained in section 3.7.4. These samples were further prepared according to ASTM-E8 (length 16.0 and dia 4.0 mm), treated with LSP on effective region, and tensile properties were established.

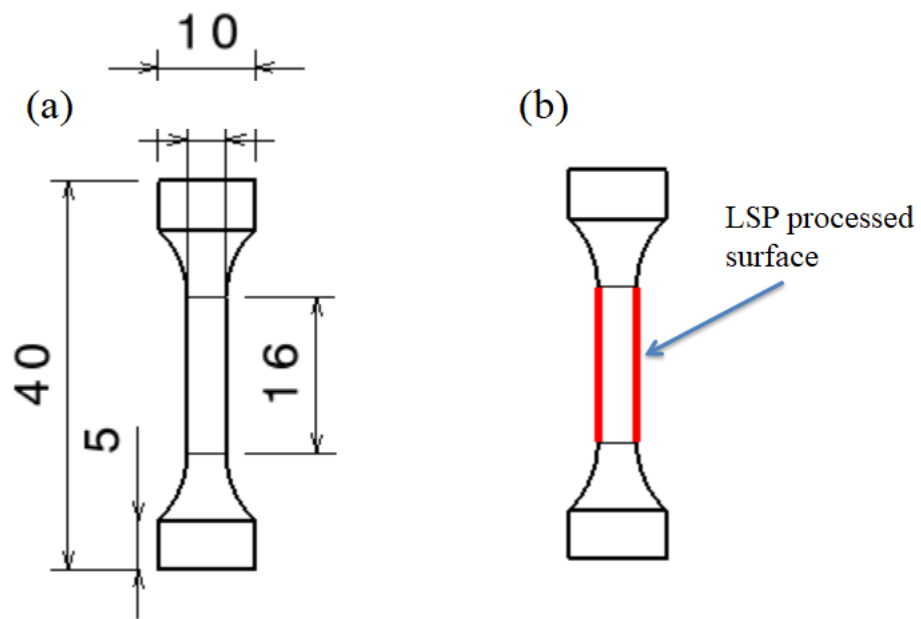


Figure 3.15 Tensile test sample details



Figure 3.16 Shimadzu universal testing machine

### 3.6.2 Wear characterization



Figure 3.17 Wear testing machine (Pin on disc Tribometer, Ducom)

As the material is exposed to routine wear environments, it is necessary to examine wear characteristics of samples to differentiate ECAP and LSP effect. Samples, having diameter of 6.0 and length 28.0 mm, were prepared according to ASTM G99-05, which were extracted from middle portion of ECAP processed specimen (to avoid inhomogeneity). LSP was performed on one face of the sample. As peening progressed, surface roughness increased. Peened surfaces were analysed for wear. DUCOM-TR-20LE-PHM 400 CHM 600 (figure 3.17) pin-on-disc Tribometer (figure 3.17) was used to estimate the wear behaviour of ECAP and LSP processed samples at room temperature. EN31 steel hard (65 HRC) polished disc was used as sliding surface, and the experiment was conducted for 2500 m, sliding speed of 3.0 ms<sup>-1</sup>, for a 40 N of load (Gopi. et al, 2017). Disc was cleaned by polishing using P1000 grade silicon carbide paper followed by acetone, to remove all the previous debris, before each trial. Worn surface of tested samples were examined by SEM to analyse the effect of ECAP and ECAP+LSP for wear mechanism.

### 3.6.3 Nano indentation



Figure 3.18 Agilet G200 Nanoindenter

As the proposed work deals with breakdown of large grains into small grains, it is very important to assess the mechanical properties in small scales. Nano indentation experiment was carried out using Agilet G200 (figure 3.18) to estimate hardness and elastic modulus at surface level. As specimens were processed by ECAP and LSP, it is important to examine the properties along the depth. TB15269 diamond tip is used for the indentation with penetration rate of  $10 \text{ nms}^{-1}$ , to a depth of indentation 600 nm, at strain rate of  $0.05 \text{ s}^{-1}$ . Figure 3.19 shows the location of experiment performed.

Table 1: Data points for measurement of hardness

Sl. No.	1	2	3	4	5	6	7	8	9	10	11	12
Data points	a	a-b	b-c	c-d	d-e	e-f	f-g	g-h	h-i	i-j	j-k	k-l
Distance ( $\mu\text{m}$ )	50	50	100	100	100	100	100	100	100	100	100	100



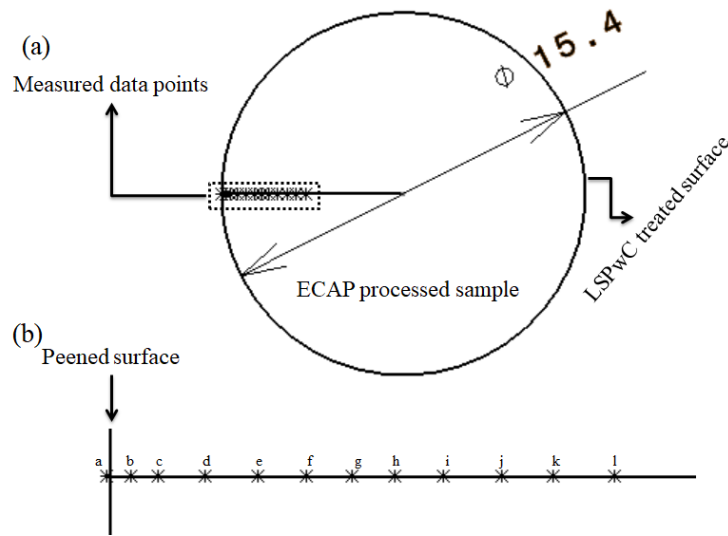


Figure 3.19 (a) Locations of Nano indentation carried out on ECAP and ECAP+LSP processed sample, and (b) zoomed view of data points

### 3.6.4 Surface roughness

LSP is a surface treatment procedure for inducing plastic deformation at surface level, which induces surface irregularities at processed region. It is necessary to study the irregularities for quality and performance of the surface. LSP was executed at 100, 200 and 300 % of coverage at energy density of  $8 \text{ GWcm}^{-2}$ . Surface roughness was measured using Confocal Microscope (Olympus LEXT 4000) (figure 3.20) and 3-dimensional surface image were extracted. In confocal microscope, series of images were extracted at different depth of focus, thereby forming a 3-dimensional image.

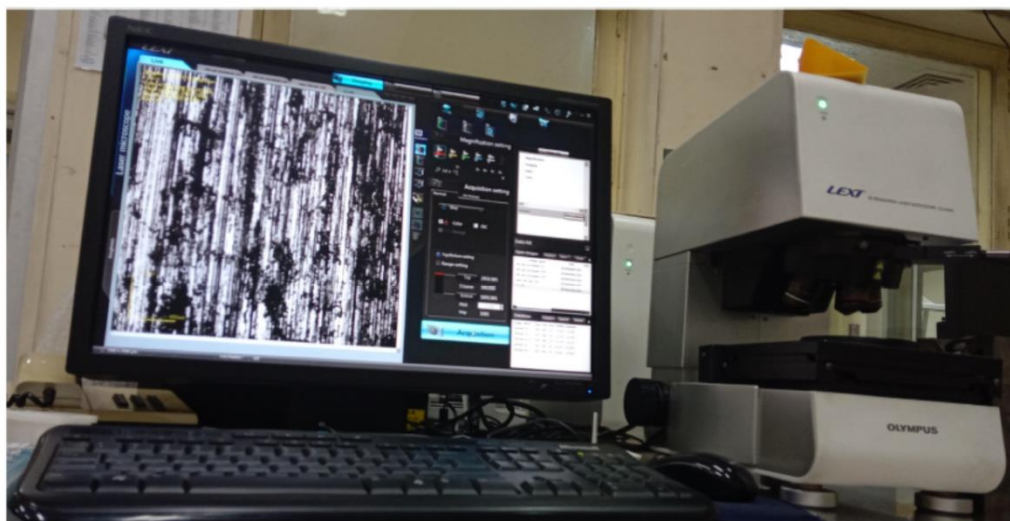


Figure 3.20 Confocal microscope (Olympus LEXT 4000)

### 3.6.5 Fatigue characterization

Fatigue specimens were prepared as per ASTM E-466 (ASTM 2015), and surface was processed by LSPwC as shown in figure 3.21(a). Low cycle fatigue tests are executed on servo hydraulic axial testing machine at room temperature, with a frequency of 15 Hz. Stress controlled methods were chosen with stress ratio of ( $R = \sigma_{\min}/\sigma_{\max}$ ) 0.125 (Fluctuating stress), with maximum stress of 120 MPa. This test was repeated on fatigue specimens, prepared at different stage of processing.

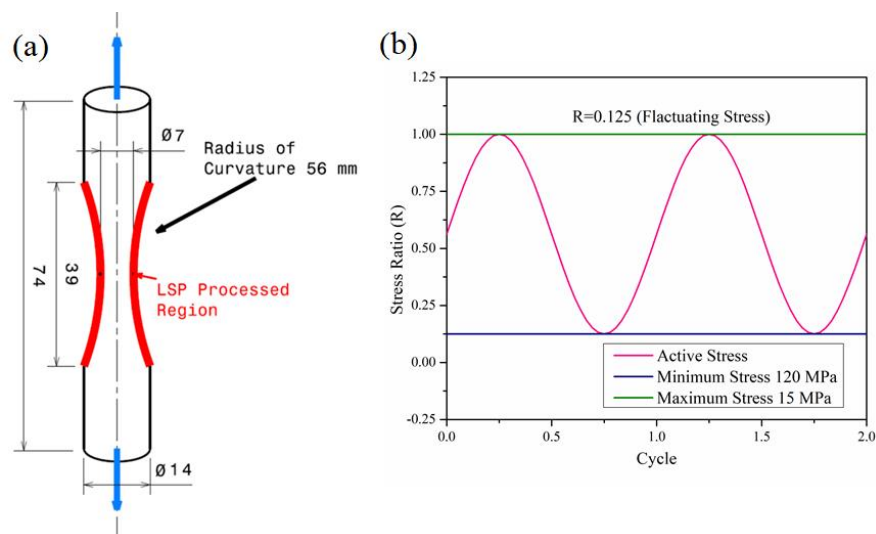


Figure 3.21 (a) Schematic representation of Fatigue sample description and (b) Stress ratio curve

## CHAPTER 4

### RESULTS AND DISCUSSIONS

#### 4.1 Equal channel angular pressing of AM80 alloy

AM80 alloy were received from supplier, and homogenized for 24 h at 350 °C. ECAP was executed using route Bc for upto four passes at 275 °C. Microstructures were analysed for as-received (cast), homogeneous and ECAP procesed samples using optical microscope, and SEM. XRD was conducted to indentify the phases in material. Tensile tests were conducted to examine the strength of material at different processing stage of processed samples.

##### 4.1.1 Microstructure analysis

Microstructures of as-cast and ECAP processed samples up to 4 passes are shown in figure 4.1 and 4.2. Solidification of molten metal was initiated with nucleation of Mg in the temperature range of 600-650°C and formation of eutectic phases at 437°C with Mg-Mg<sub>17</sub>Al<sub>12</sub>. Figure 4.1 (a) shows the microstructure of AM80 with  $\alpha$ -Mg dendrites, having secondary arms with six fold symmetry. Eutectic Mg<sub>17</sub>Al<sub>12</sub> and aluminium rich solid solution are distributed between secondary arms (Dahle et al., 2001). Figure 4.1 (b) shows the microstructure of homogenized sample, and it was executed to achive chemical homogeneity, which was arrested during solidification of molten metal, due to insufficint duration for optimal grain growth. Equiaxed grains with average grain size 100  $\mu$ m was observed, and average grain size was calculated using linear intercepts method (ASTM E112).

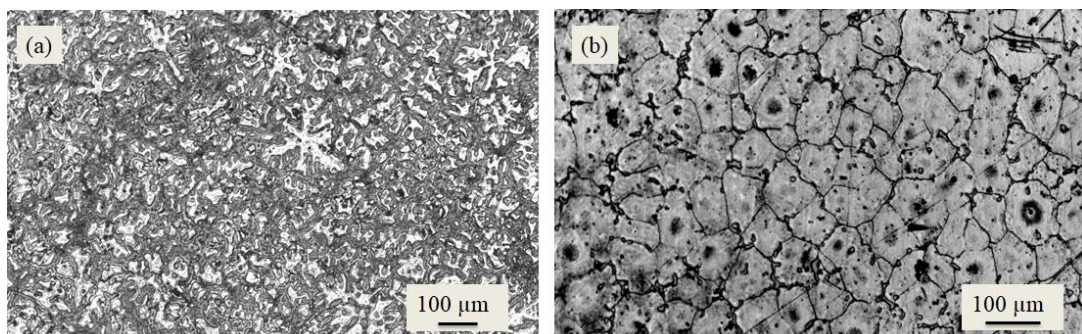


Figure 4.1 Optical microstructures of AM80 alloy (a) as-cast, (b) homogenised at 350 °C for 24 hours

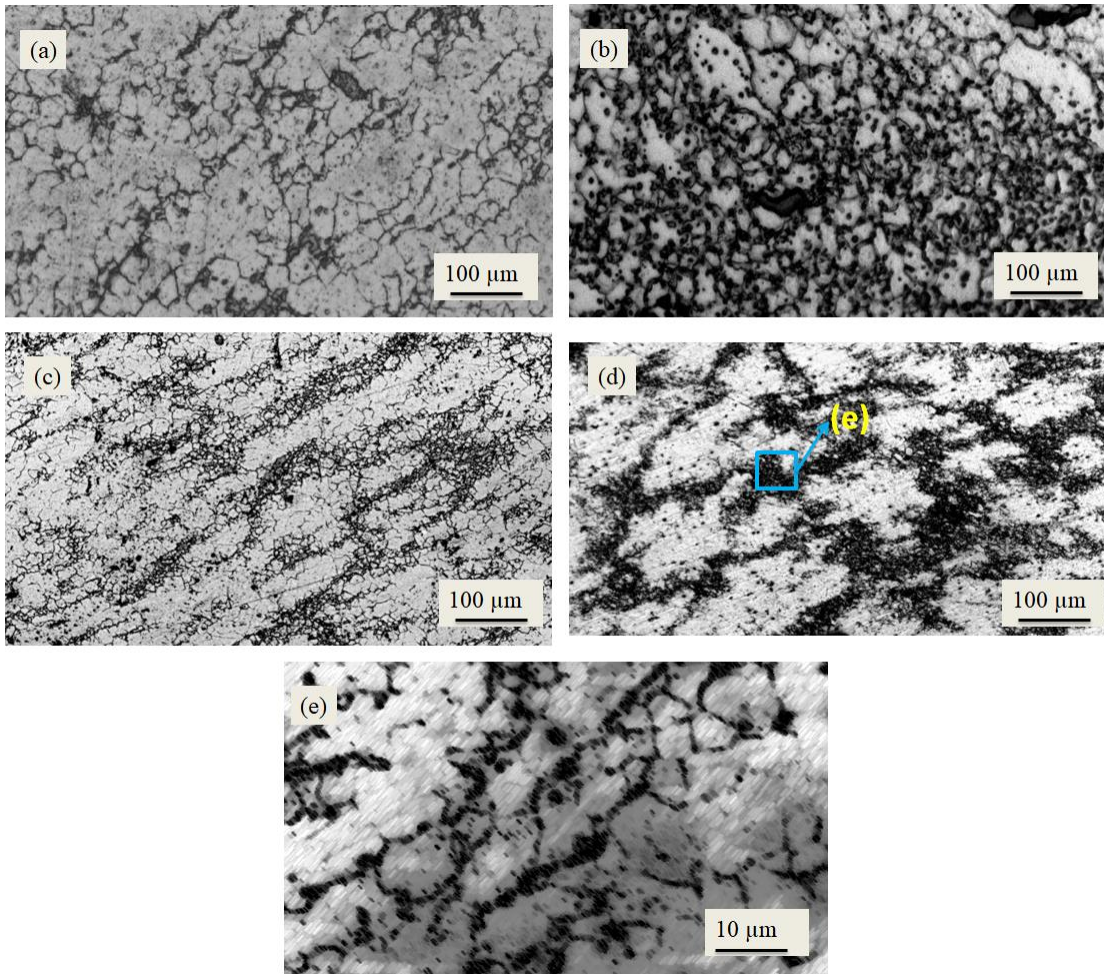


Figure 4.2 Optical images of AM80 alloy, ECAP processed at 275 °C (a) 1 pass, (b) 2 pass, (c) 3 pass, (d) 4 pass, (e) zoomed view of 4 pass.

Microstructures of samples processed by ECAP 1, 2, 3 and 4 passes are shown in figure 4.2 (a, b, c & d). After the first pass, large grains ruptured into many small grains, and are surrounded to larger grains, due to higher dislocation density, which creates bimodal structure (Akbaripanah et al. 2013b). Average grain size was found to be 65  $\mu\text{m}$ , 45  $\mu\text{m}$ , 8  $\mu\text{m}$  and 3  $\mu\text{m}$ , respectively, for samples processed by ECAP for 1, 2, 3 and 4 passes. Similar tendency of grain refinement was reported for AM30 magnesium alloy (Jahadi et al. 2014). AM80 possesses Mg as base material, having Hexagonal Close Packing (HCP) crystal structure with limited number of slip system. OM image revealed the existence of deformation twins which is necessary for plastic deformation in HCP structures (Christian and Mahajan 1995; Koike 2005). It was observed that higher ECAP passes contribute to severe grain refinement, due to the induction of repetitive dislocations of high density.

Most of the grains in the 2 pass samples are well refined, and heterogeneous, as grain size varies from 15  $\mu\text{m}$  to 50  $\mu\text{m}$ . This is one of the reasons for 2 pass ECAP specimen to have high strength (Figueiredo and Langdon 2010; Seipp et al. 2012). There is possibility of dynamic recrystallization during pressing or static recrystallization during the heating of specimen for pressing (Koike 2005).

#### 4.1.2 SEM analysis of ECAP processed samples

SEM generates images by scanning the surface by electrons in the form of focused beam, and surface topography was created by interaction of electrons on atoms existing at the surface.

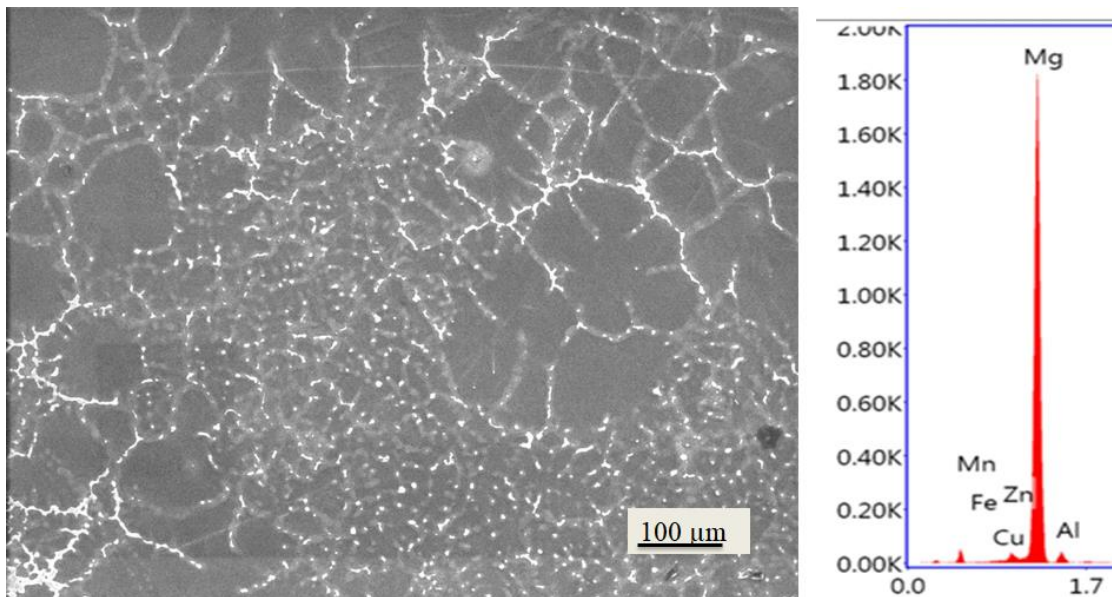


Figure 4.3 SEM image with EDX data of as-cast sample

Figure 4.3 shows SEM image of as-cast sample. Irregular grains with dendritic nature were observed, due to improper cooling (Easton et al. 2016). Addition of alloying element like Al and Mn creates secondary phases, which are present at grain boundaries, surrounded by  $\alpha$ -Mg. EDX revealed the chemical composition of as-cast material, which involves Mg as parent material, alloying elements as Al, and Mn and some impurities as Fe, Zn and Cu.

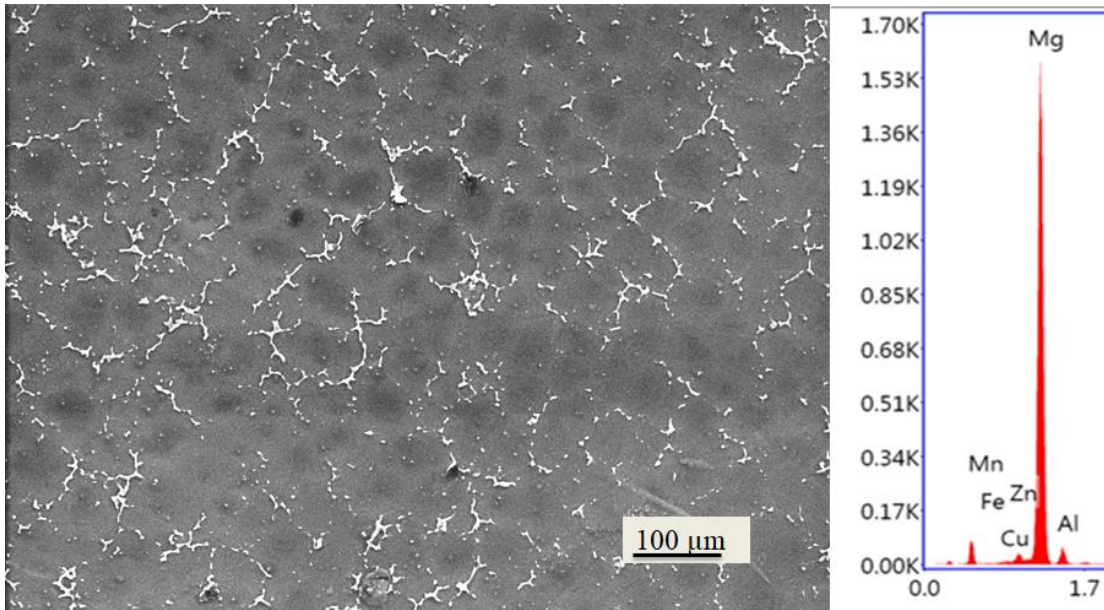


Figure 4.4 SEM image with EDX data of homogenised sample

Homogenisation were carried out for 24 h at 350 °C and naturally cooled to room temperature, to dissolve unwanted chemical inhomogeneity occurred during casting processes. SEM image in figure 4.4 revealed the modification occurred after homogenisation of as cast sample. Irregular dendritic grains are converted into new equiaxed grains, due to recrystallization, with average grain size of 100 μm.

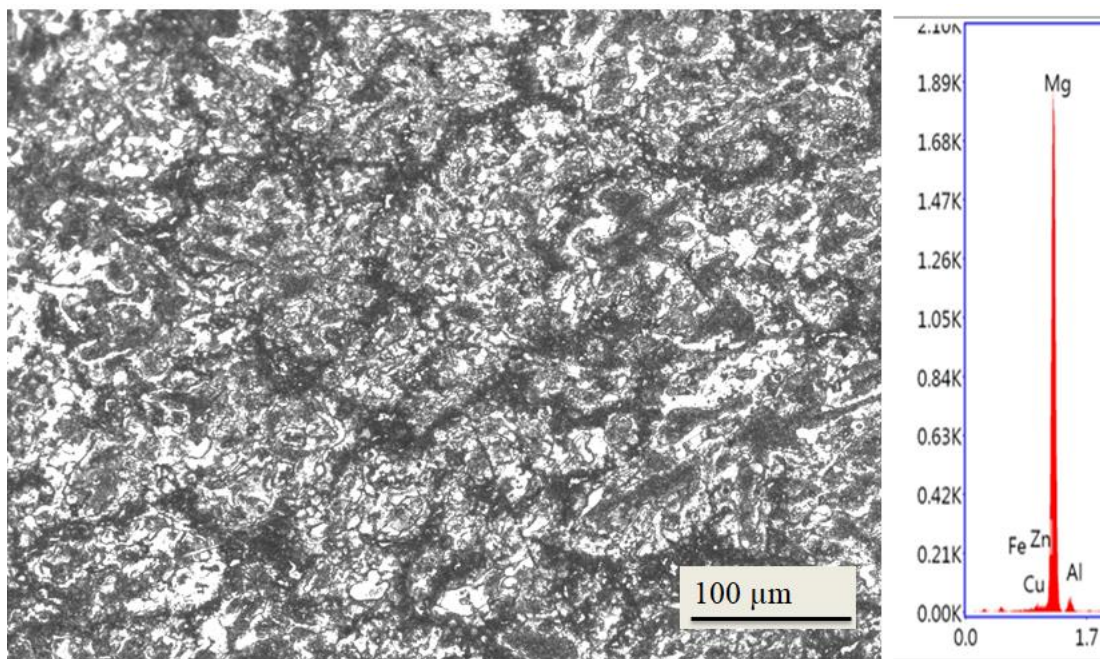


Figure 4.5 SEM image with EDX data of 1-pass ECAP processed sample

Figure 4.5 shows the SEM image with EDX data of 1-pass ECAP processed sample. Due to shearing action, at intersection of ECAP channels, grains were ruptured because of severe plastic deformation, which is assisted by multiple mechanisms operated together. These mechanisms include different slip systems, such as basal, prismatic and twinning. Temperature plays key role in the formations of grain refinement during ECAP. Some of the (prismatic & pyramidal) slip systems are assisted by temperature in Mg, but relapse from smaller grains to bigger grain (grain growth) occurred due to dynamic recrystallization. SEM image shows in-homogeneously ruptured grains across the sample. EDX data shows the chemical composition data of material at surface.

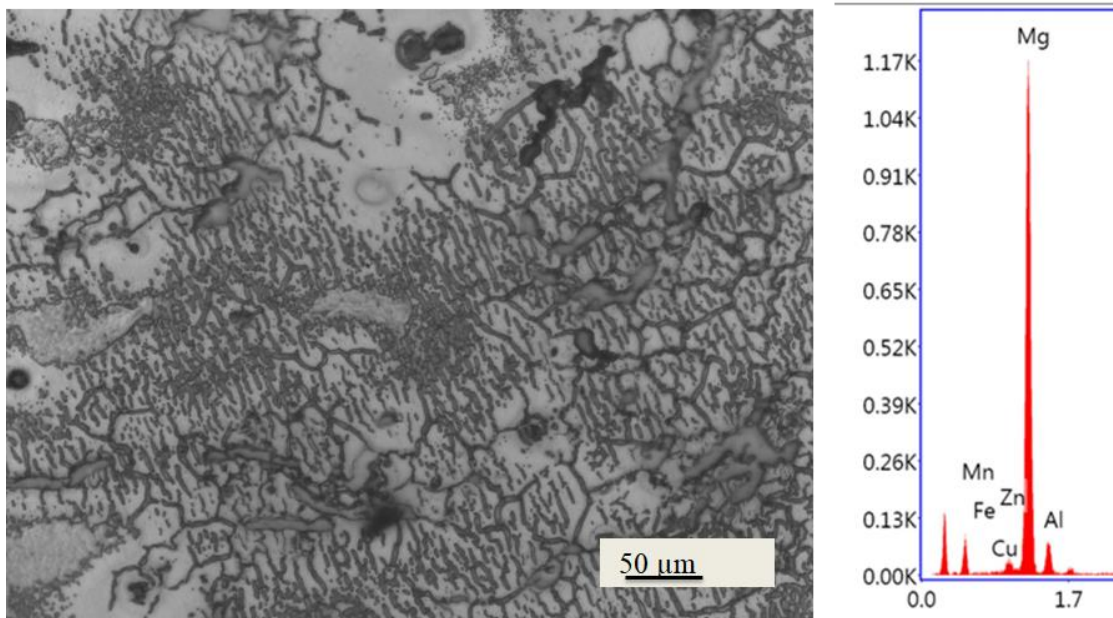


Figure 4.6 SEM image with EDX data of 2-pass ECAP processed sample

Figure 4.6 shows further grain refinement of AM80 alloy after 2<sup>nd</sup> pass. Refinement of coarse grains was observed with dislocation densities. Average grain size of 45 μm was observed, and there are many fine grains surrounded by coarse grains, with number of dislocations, being observed. The chemical composition of the sample at surface is represented in EDX data.

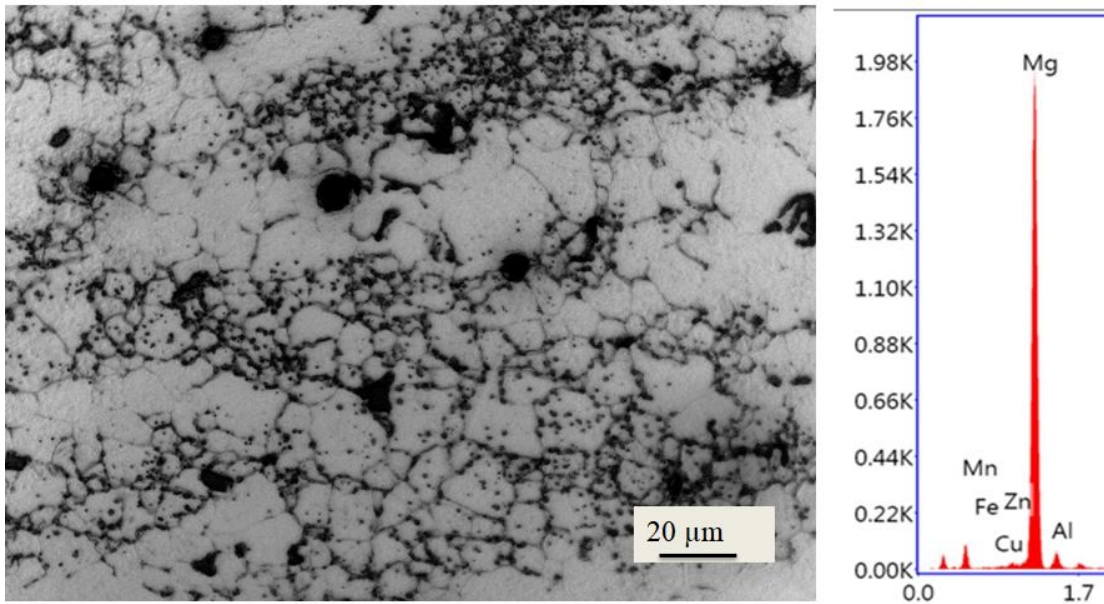


Figure 4.7 SEM image with EDX data of 3-pass ECAP processed sample

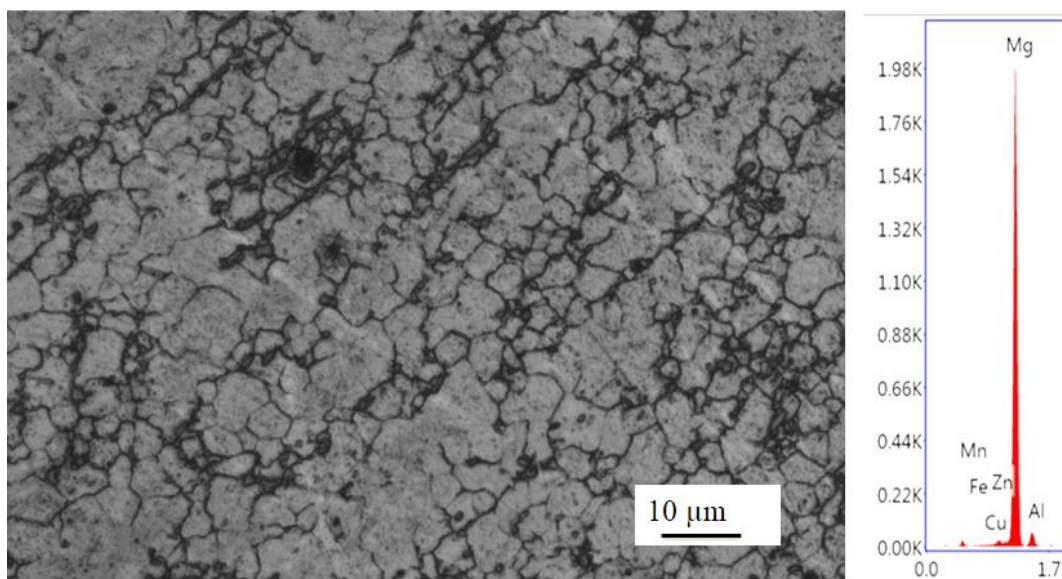


Figure 4.8 SEM image with EDX data of 4-pass ECAP processed sample

SEM images of three and four pass of ECAP processed samples are shown in figure 4.7 & 4.8. Average grain size after three and four passes was found to be 8 μm and 4 μm, respectively, with high percentages of dislocation densities. EDX data shows the inhomogeneity distribution of chemical composition of the samples.



### 4.1.3 X-Ray diffraction analysis

XRD results of as-cast, ECAP processed 2 and 4 pass samples are shown in figure 4.9, which shows intermetallic phases ( $Mg_{17}Al_{12}$ ,  $Mg_2Al_3$  and  $MnAl_6$ ) and variations in peak intensities were observed in as-cast, two and four pass samples. Change in peak intensity of precipitates of  $Mg_{17}Al_{12}$  and  $MnAl_6$  were increased at  $\sim 58^\circ$  and  $\sim 70^\circ$  for 2P sample. Hence, increase in mechanical properties was observed. Fluctuation in peaks was observed in  $(0002)$ ,  $(10\bar{1}0)$ ,  $(10\bar{1}1)$ ,  $(10\bar{1}2)$ ,  $(11\bar{2}0)$ ,  $(10\bar{1}3)$ ,  $(11\bar{2}2)$  and  $(20\bar{2}1)$  planes. These planes activate prismatic and pyramidal slip, and exhibits texture modification due to ECAP process. These texture modifications are because of generation of new grain boundaries during ECAP process, where the existing texture is removed by shear deformation of ECAP process and the texture is formed (refhaha).

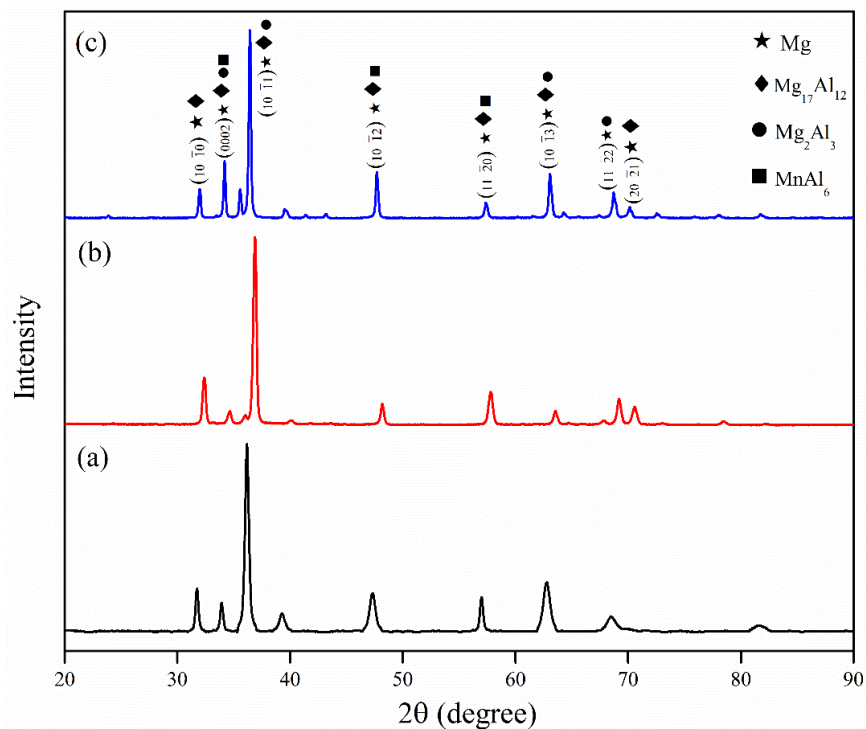


Figure 4.9 XRD profile of (a) as-cast (b) ECAP 2P and (c) ECAP 4P samples

Al and Mg have been important in developing advanced light weight composite materials, having combined HCP and BCC structures, for structural application. Dendritic grain structures of as cast samples showed improper diffusion of Mg and Al during casting process. Homogenization of samples at  $380^\circ C$  for 24 hours, accelerates the diffusion of atoms and provide enough time for sample to reach equilibrium

condition, where formation of  $Mg_2Al_3$ , and  $Mg_{17}Al_{12}$  were confirmed. (Kulkarni and Luo 2013). Precipitates of  $MnAl_6$  were also observed through XRD analysis.  $Mg_{17}Al_{12}$  phase softening was reported by Mathur et al., (2016), with respect to rise in temperature. Hardness of 3.5 GPa was measured at 25 °C, which was stable till 120 °C. Further rise in temperature to 278 °C, hardness dropped to 0.7 Gpa, which helped in executing ECAP at elevated temperature as  $Mg_{17}Al_{12}$  leads to low ductility.

#### 4.1.4 Tensile strength

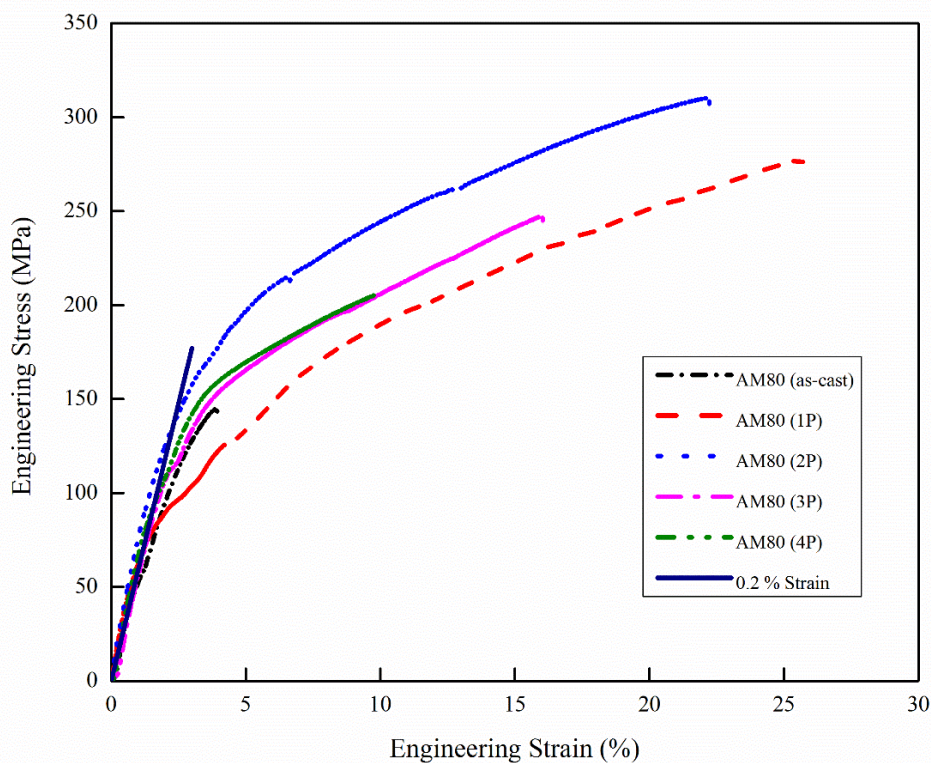


Figure 4.10 Tensile strength of ECAP processed AM80 alloy under different passes Stress strain curves of as-cast and ECAP processed AM80 samples are shown in figure 4.10. Failure of as cast sample was observed at 140 MPa. In 1 pass ECAP processed sample, UTS of 270 MPa were recorded. Maximum UTS of 310 MPa was observed after 2 passes of ECAP. Percentage elongation of 4 % and 25 % was recorded in 1 and 2 pass ECAP processed samples. Further, increase in ECAP passes for 3<sup>rd</sup> and 4<sup>th</sup> pass, percentage of elongation reduced. It was observed that YS and UTS increased during first and second passes and then decreases during the subsequent passes. Decrease in strength at higher passes of ECAP was because of weaker crystallographic texture (Kim

et al. 2003) and Schmid factor (Akbaripanah et al. 2013b). No physical yielding was observed during testing of sample, hence slope with ECAP 2-pass (slope similar to elastic limit) is drawn at 0.2 % of strain, and correspond yield strength was 145 MPa.

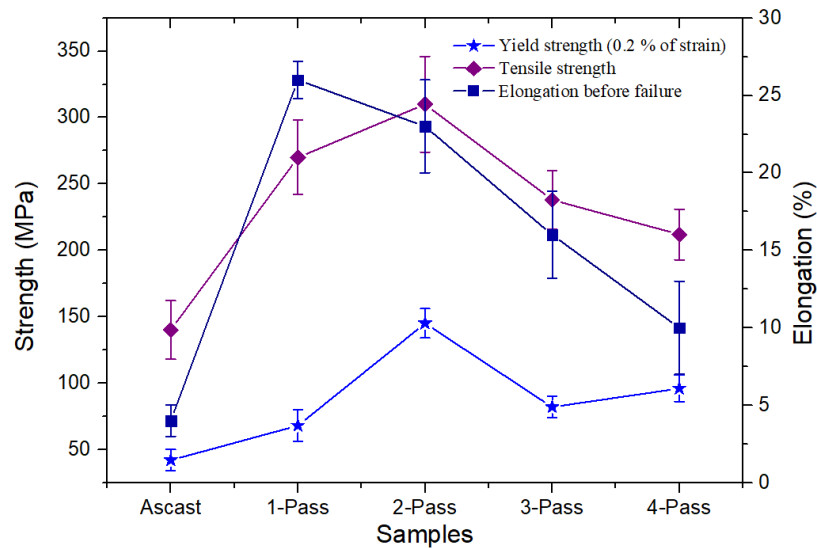


Figure 4.11 Comparison of yield strength, tensile strength and elongation of samples

Tensile tests are carried out for three sets, and figure 4.11 shows the comparison of yield strength, tensile strength and elongation of samples at different passes. Highest yield strength and tensile strength are observed at 2 pass ECAP processed samples, and highest elongation are observed at 1 pass ECAP processed samples. These change in elongation and strength are due to change of phases (Ritchie 1998).

#### 4.1.5 Fractography

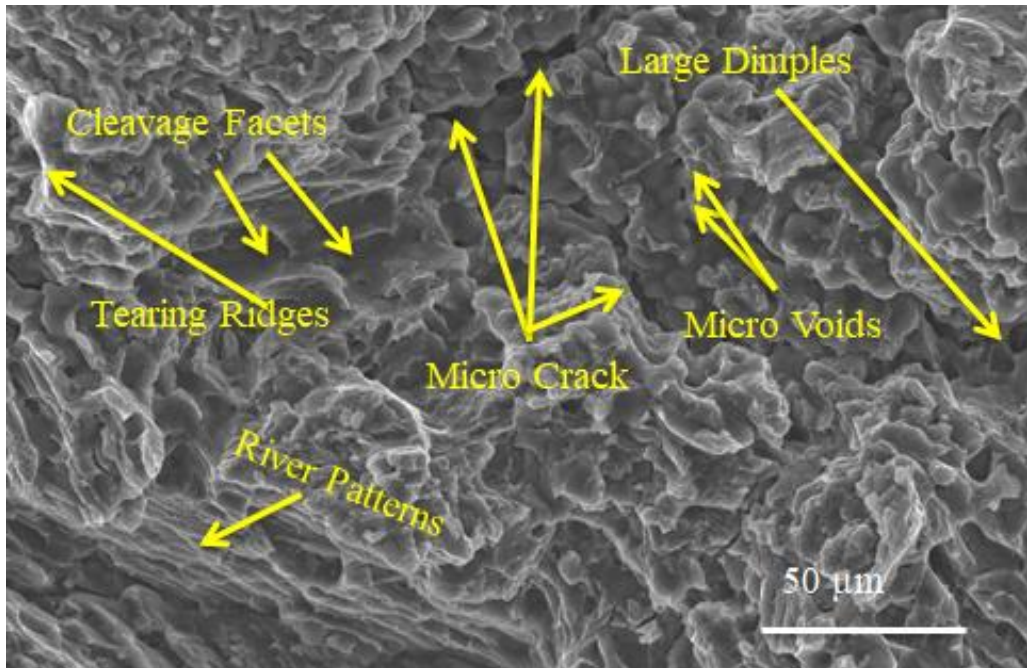


Figure 4.12 SEM Image of fracture surface for as-cast sample (Tensile)

Magnesium possess limited slip system for plastic deformation, because of HCP structure, at room temperature. Hence, fracture surface of as-cast sample revealed a brittle fracture, indicating cleavage as the principal fracture mode (Abbaschian et al. 2009). Figure 4.12 shows the fracture surface of as-cast sample. There are some undesired features, such as secondary cracks and micro-voids that are exposed to loading. There are some minor cracks that converge with main crack and forms tearing ridges. River flow pattern was observed on the surface which confirms trans-granular fracture indicating poor plastic deformation. River flow pattern was observed on the surface which confirms trans-granular fracture indicating poor plastic deformation. Fracture is characterized by cleavage facets, steps and rivers. Dimples are also visible in some regions, the combination of cleavage and dimples are observed along with undesired cracks. Fracture is a combination of brittle and ductile fracture and more dominated by brittle nature.

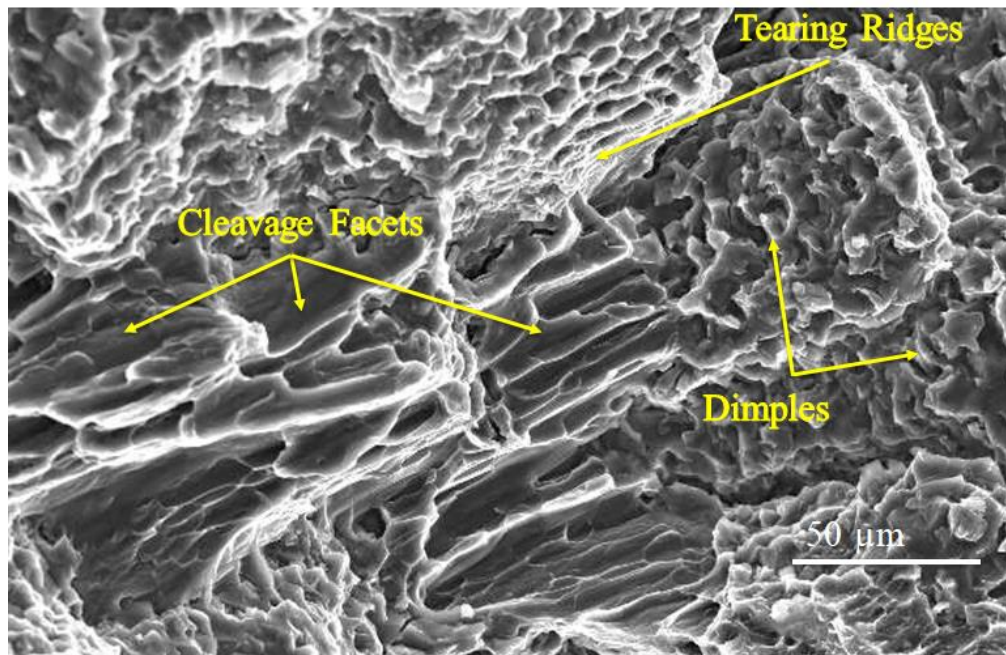


Figure 4.13 SEM Image of fracture surface of 1-pass ECAP processed sample (Tensile)

Figure 4.13 shows the fracture surface of 1-pass ECAP processed sample, failed under tensile loading. Combination of cleavage facets with dimples are observed. The dimples are formed due to large number of active nucleation site due to loading, and adjacent microvoids merge before formation of larger crack. Cleavage possess low energy fracture, and propagates along low indexed crystallographic planes (Handbook 1987).

Figure 4.14 show fracture surface of ECAP processed 2-pass sample under route B<sub>C</sub>, and fracture surface revealed the combination of ductile and brittle fracture. Cleavage steps were also found, followed by small trans-granular cracks. Direction of crack growth is decided based on coalescence of small cracks to main crack. From figure 4.2 (b), 2-pass sample, under route B<sub>C</sub>, showed bimodal structure, where small grains are surrounded by large grains and these leads to heterogeneous fracture surface having different sizes of dimples.

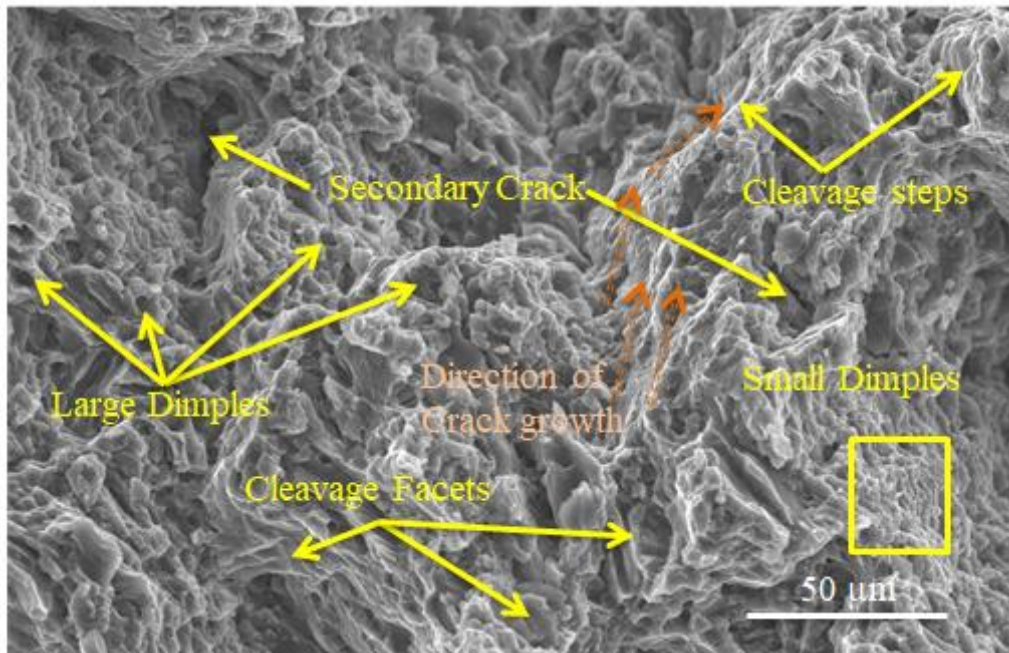


Figure 4.14 SEM Image of fracture surface for 2-pass sample under route B<sub>C</sub> (Tensile)  
 Small dimple causes more elongations compared to large dimples. This fracture surface consists of cleavage facets, steps, small dimples and large dimples with some secondary cracks, which influences combination of ductile and brittle nature.

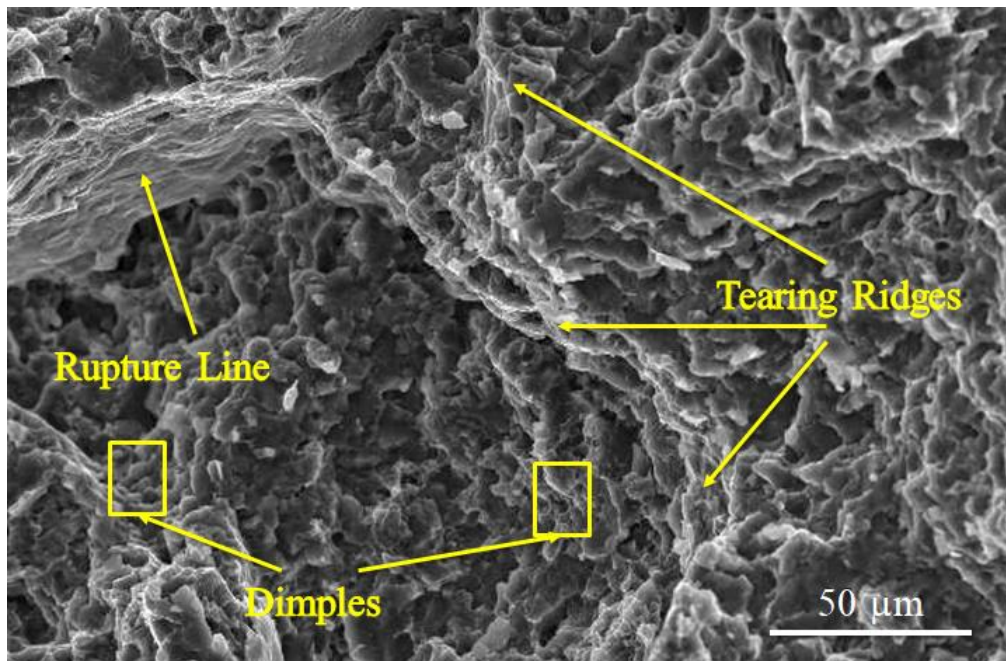


Figure 4.15 SEM Image of fracture surface for 3-pass sample under route BC (Tensile)

Figure 4.15 SEM Image of fracture surface for 3-pass ECAP processed sample under route BC. Here we can observe different shapes (conical, elongated) of dimples, which are governed by stress inside the material. Elongated dimples are formed due to tear or shear mode of fracture, and the depth of the dimple depends on microstructure and plasticity of material.

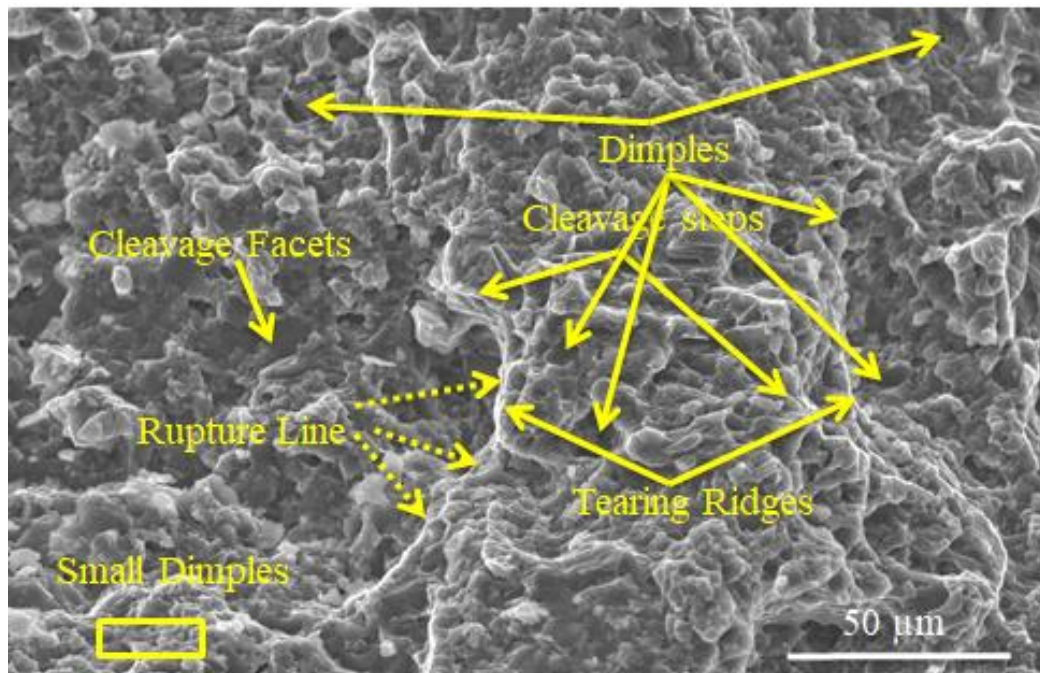


Figure 4.16 SEM Image of fracture surface for 4-pass sample under route B<sub>C</sub> (Tensile)

Figure 4.16 shows the fractured surface of ECAP processed 4-Pass sample, under route B<sub>C</sub>, with fine and homogeneous grains, compared to ECAP 2-pass sample. Fracture surface contains cleavage facets, steps, different sizes of dimples and no significant secondary cracks were present due to processing by ECAP route B<sub>C</sub> till 4 pass. Fracture behaviour is similar to route ECAP 2-Pass sample, having combination of ductile and brittle fracture with increase in percentage of elongation.

Ductility depends on number of active slip systems at working temperature, as Mg having hexagonal slip at base plane  $(0001) \langle 11\bar{2}0 \rangle$  and  $(10\bar{1}0) \langle 11\bar{2}0 \rangle$  as a secondary slip on non-basal face, constrains the ductility at low temperatures.

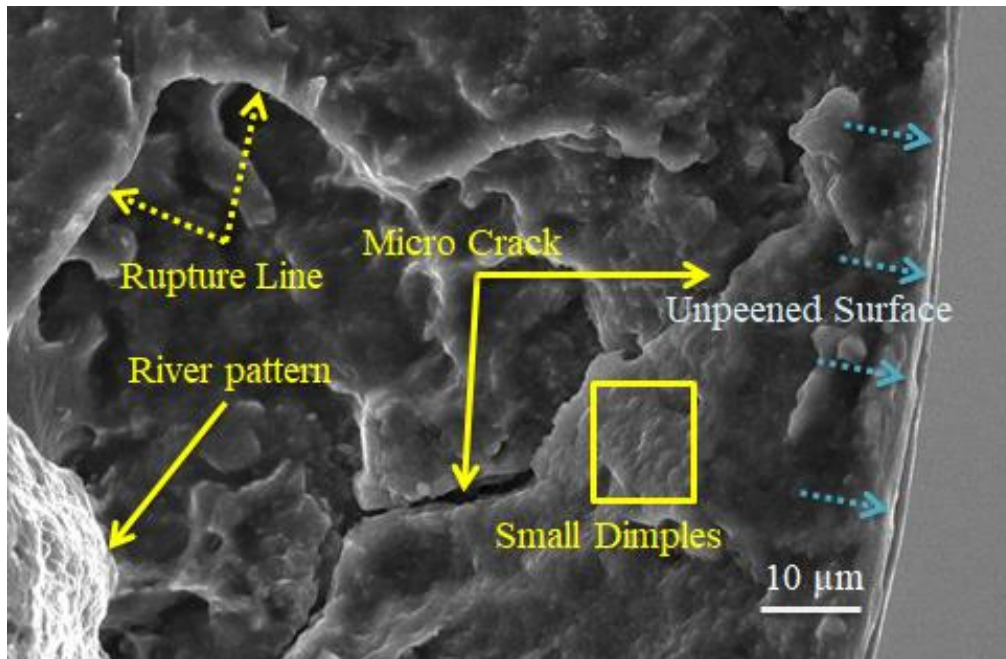


Figure 4.17 SEM Image of fracture surface for near surface zoomed view of 2-pass sample Route B<sub>C</sub>

This behaviour is also influenced by adding Al as alloying element (Mordike and Ebert 2001). Inter-metallics  $Mg_{17}Al_{12}$  (Cubic),  $Mg_2Al_3$  (Cubic) and  $MnAl_6$  (orthorhombic) have non hexagonal slips, hence ductility is improved. Ductile fracture had higher fracture strength compared to brittle fracture. Based on foregoing discussion, it is clear that 2 pass ECAP samples processed by route B<sub>C</sub> have desirable tensile behaviour and hence ECAP 2-Pass samples were used for further processing with LSPwC.

As the investigation of AM80, processed by ECAP till four pass were carried out, it was found that ECAP processed 2-pass sample under route B<sub>C</sub> showed best results compared to as-cast, homogenized, 1-pass, 3-pass and 4-pass. Hence AM80 processed with ECAP 2-pass were considered for the further grain refinement studies at surface level.

#### 4.2 Laser shock peening without coating carried on ECAP 2-pass processed samples

LSPwC was executed on ECAP processed 2-pass AM 80 alloy, and all the samples were surface polished by Silicon Carbide emery paper till 1500 grade before applying laser pulses.



#### 4.2.1 TEM analysis

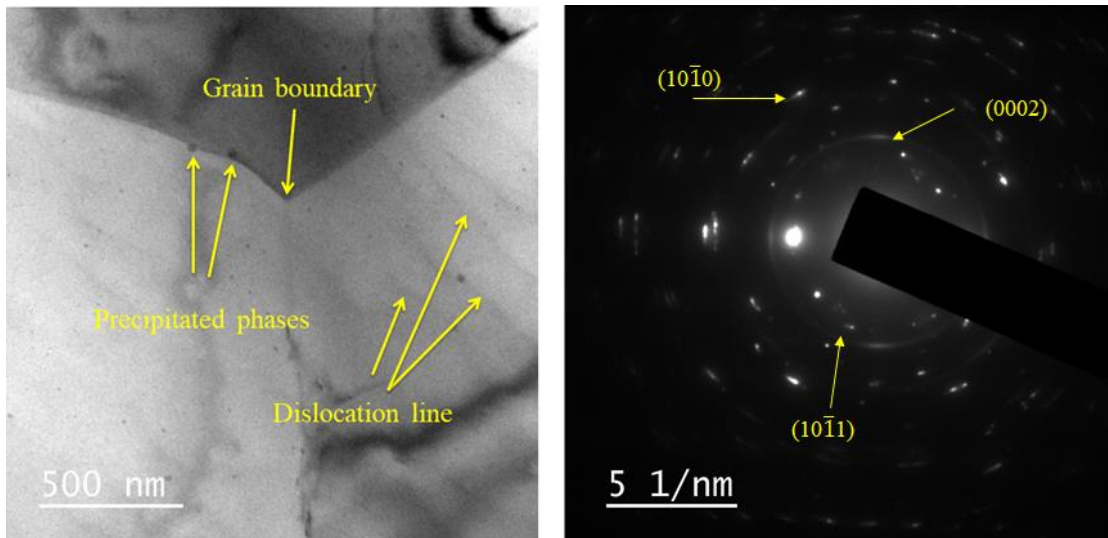


Figure 4.18 TEM image of ECAP 2-pass processed under route B<sub>C</sub> with SAED pattern

ECAP induces permanent deformation in materials due to shearing action, where arrangement of atoms changes their surroundings, based on degree of strain induced during deformation. Figure 4.18 shows the TEM image of ECAP processed 2-pass AM80 sample with SAED pattern. Grains were refined, with the occurrence of dislocation lines and precipitate phases. Full grains were not visible, because of the presence of large grains of size 45  $\mu\text{m}$  (figure 4.6), Plastic deformation occurred due to movement of dislocations, caused by slip and twinning in a crystal (Lavrentev 1975). Formation of twins and twin boundaries showed the influence of nucleation of dislocations and dislocation pile-up on increase in strength and ductility of crystal (Kochmann and Le 2009).

Figure 4.19 shows the TEM images of AM80 alloy processed by 2-pass ECAP, and LSP at 8  $\text{GWcm}^{-2}$  by 100 % of coverage (1 time). TEM sample was extracted from a region, approximately 50  $\mu\text{m}$  from the peened surface. Banded/elongated structure was observed, due to LSP at surface level, which is formed by plastic deformation at high strain rate. Figure 4.19 (a) shows high dislocation density with shear bands caused by LSP (Lainé et al. 2017). Precipitates were clearly visible and more compared to ECAP processed sample, and dislocation cells were dominated. Figure 4.19 (b) shows the nano-grains of average size of 90 nm formed during LSP.

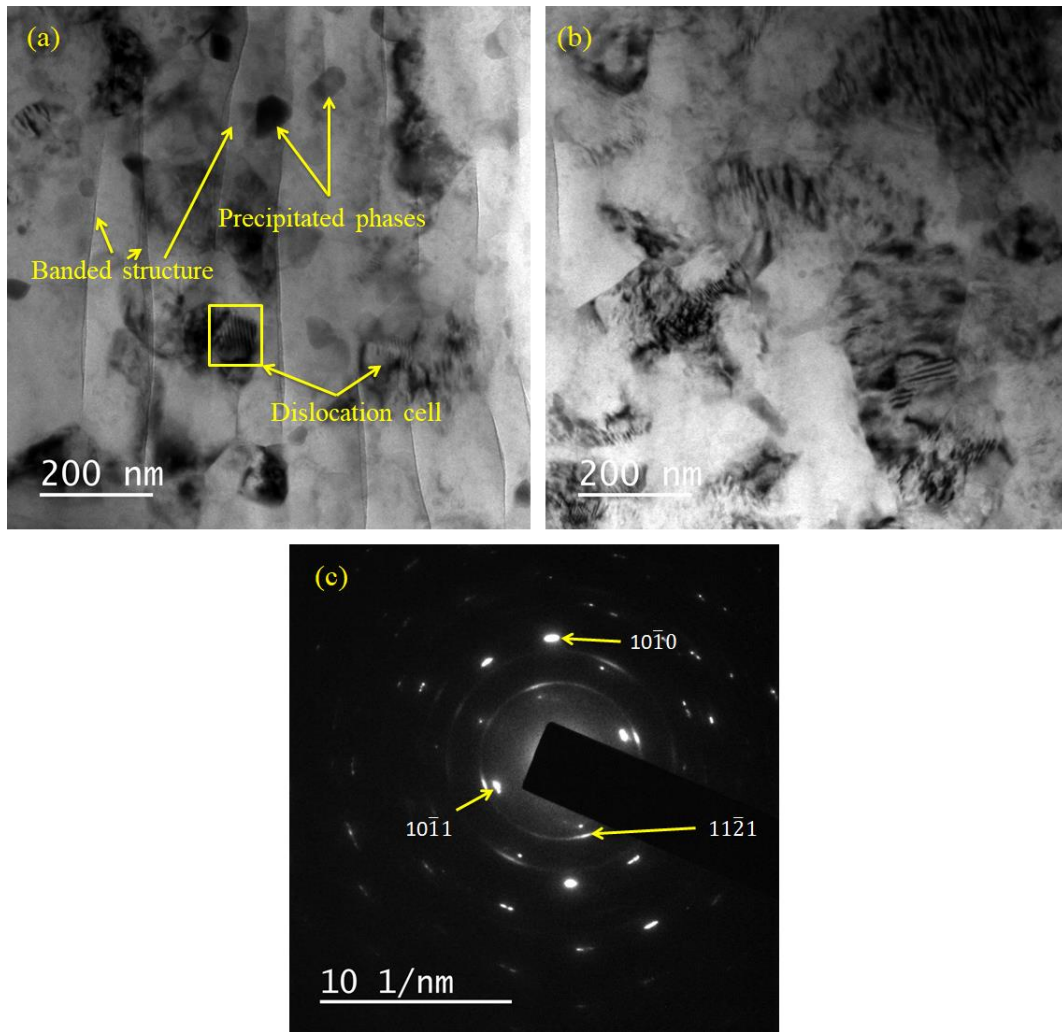


Figure 4.19 TEM image of ECAP 2-pass processed under route B<sub>C</sub> and LSP processed with 8 GWcm<sup>-2</sup> (100 % of coverage) with SAED pattern

LSP was repeated (2<sup>nd</sup> time) on samples, processed by LSP followed by ECAP to achieve 200 % of coverage. This causes repeated plastic deformation at surface and results in a distorted surface. Figure 4.20 shows the TEM image of sample processed by ECAP for 2 passes under route B<sub>C</sub> followed by LSP at 8 GWcm<sup>-2</sup> for 200 % coverage, with SAED pattern, Intersection of band structures was observed due to change in peening location during repetitive peening. Laser pulses may overlap at different percentage (not controlled) during second time. As mentioned, more deformation occurs at surface with the production of finer grains, compared to 100 % coverage of LSP (figure 4.19). The average grain size observed with 200 % of coverage is 30 nm (figure 4.20 (b)).

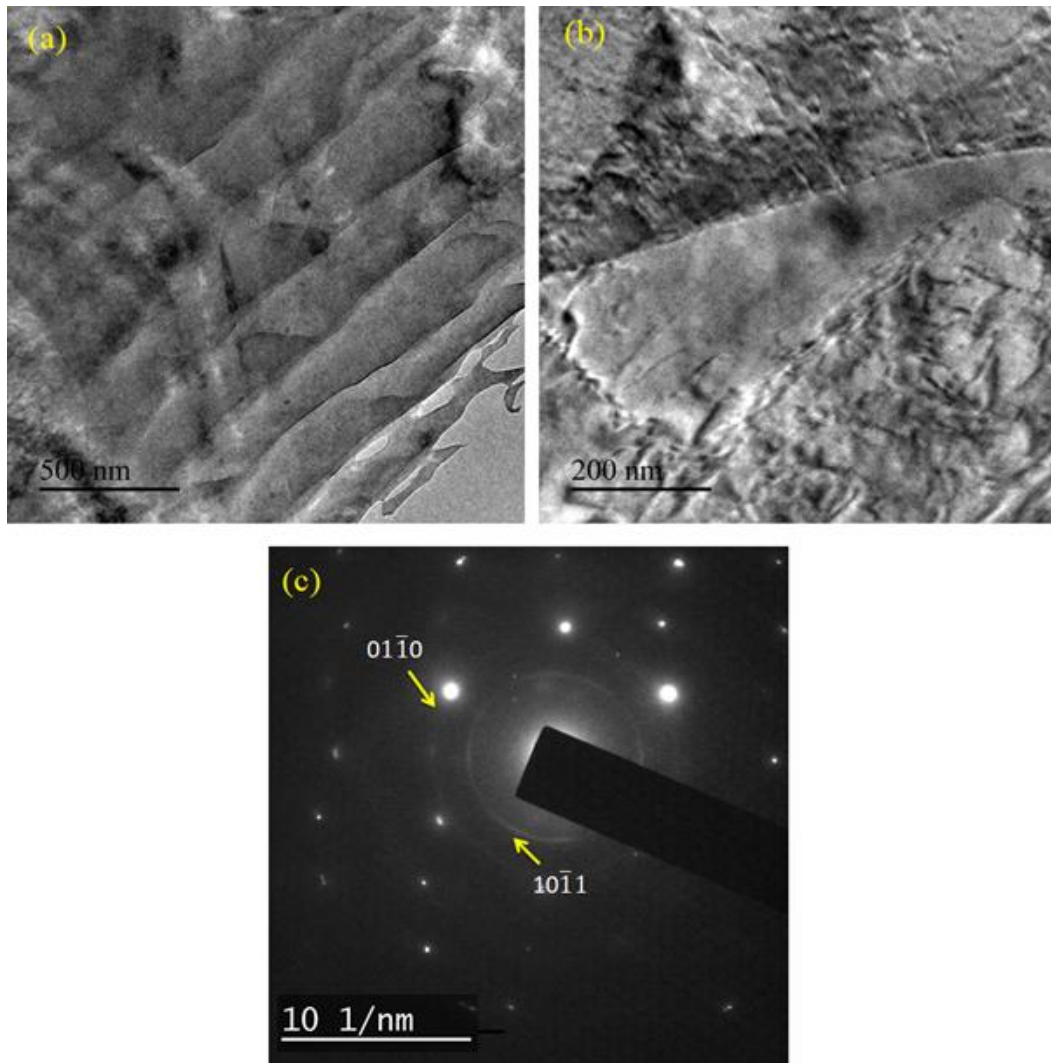


Figure 4.20 TEM image of ECAP 2-pass processed under route B<sub>C</sub> and LSP processed with  $8 \text{ GWcm}^{-2}$  (200 % of coverage) with SAED pattern

LSP is repeated third time, with same energy density ( $8 \text{ GWcm}^{-2}$ ) on samples of 200% to obtain sample of 300 % coverage. Figure 4.21 shows the TEM image of sample processed by ECAP for 2 passes followed by LSP at  $8 \text{ GWcm}^{-2}$  by 300 % coverage, with SAED pattern. Repetitive and over lapped band structures were visible in figure 4.21 (a), needle like grains, bit elongated grains were observed. Highly distorted grains were observed as in figure 4.21 (b). SAED pattern revealed the formation of sub grains in the order of nano meters, formed due to repetitive severe plastic deformation occurred during LSP at surface level.

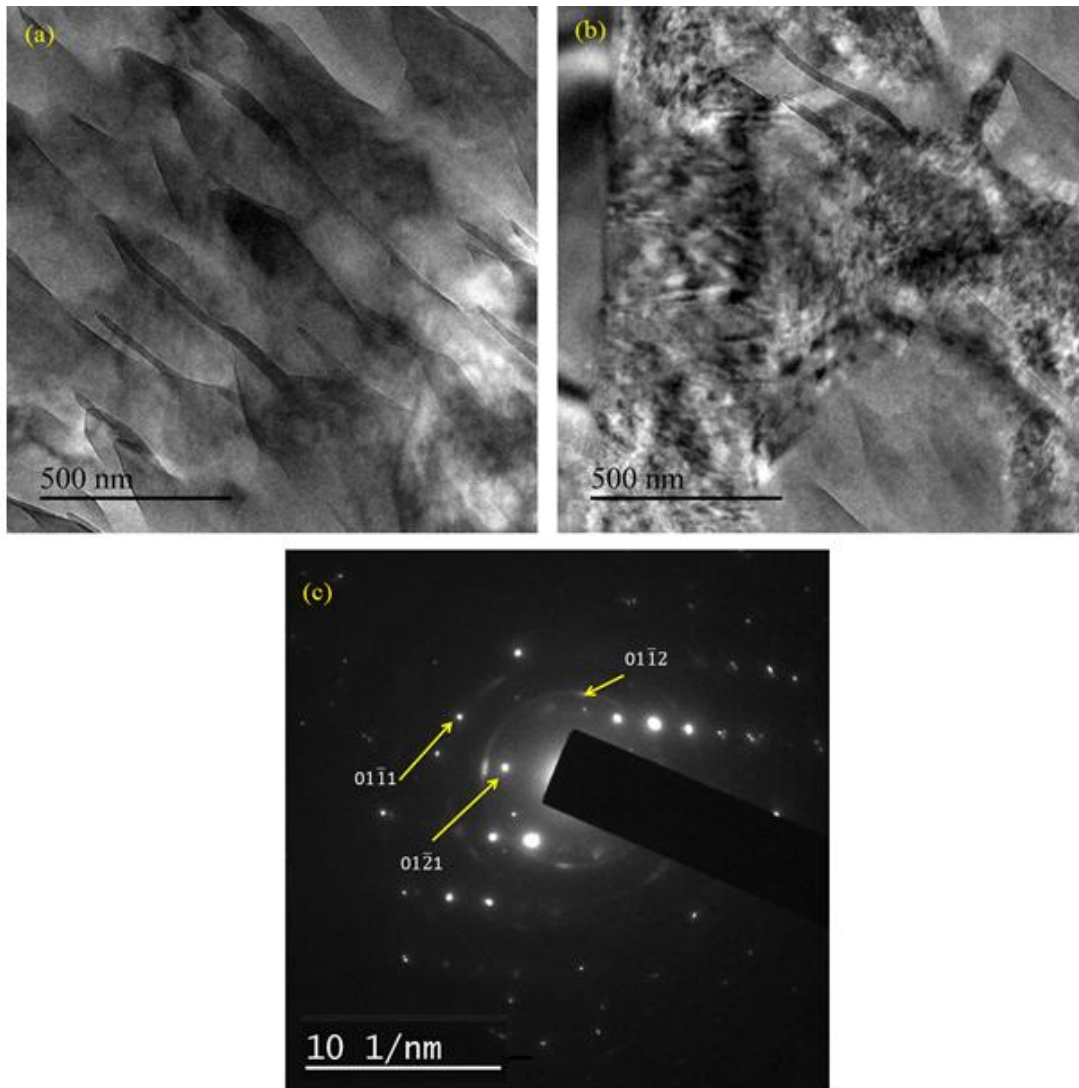


Figure 4.21 TEM image of ECAP 2-pass processed under route B<sub>C</sub> and LSP processed with 8 GWcm<sup>-2</sup> (300 % of coverage) with SAED pattern

#### 4.2.2 XRD Analysis

X-Ray diffractions were carried on AM80 alloy at different processing stage during LSP. PAN-analytical, X'pert<sup>3</sup> MRD system were used with step size of 0.03°, from 20 to 80° operated at 30 mA, 45 KV with continuous scan, at scan step time of 0.8 s. X-ray source of Cu-K  $\alpha$  having wavelength of 1.54 Å was used for extraction of diffracted peaks. Figure 4.22 shows the diffraction pattern of AM80 alloy at different processing stage.  $\alpha$ -Mg (JCPDS 00-001-1148) and intermetallic Mg<sub>17</sub>Al<sub>12</sub> (JCPDS 01-073-1148), Mg<sub>2</sub>Al<sub>3</sub> (JCPDS 00-029-0048) MnAl<sub>6</sub> (JCPDS 00-006-0665) peaks were observed. From XRD patterns, lack of symmetry was observed, with peaks at different stages of

processing. Peak at  $(2\theta)$   $38.3^\circ$  is considered for discussion, and difference in peaks were clearly distinguishable. Asymmetry (change in shape of peak) of peaks was observed due to change in relative strain and formation of nano crystalline at surface (Lojkowski et al. 2001; Umapathi and Swaroop 2018). As-cast samples showed intense peak at  $36.3$ , and there was small decrease in peak due to weakening the texture by introducing dislocations (refhaha). Further drop in peak were observed, with ECAP+LSPwC, because of induction of high dislocations and formation of nano crystalline grains.

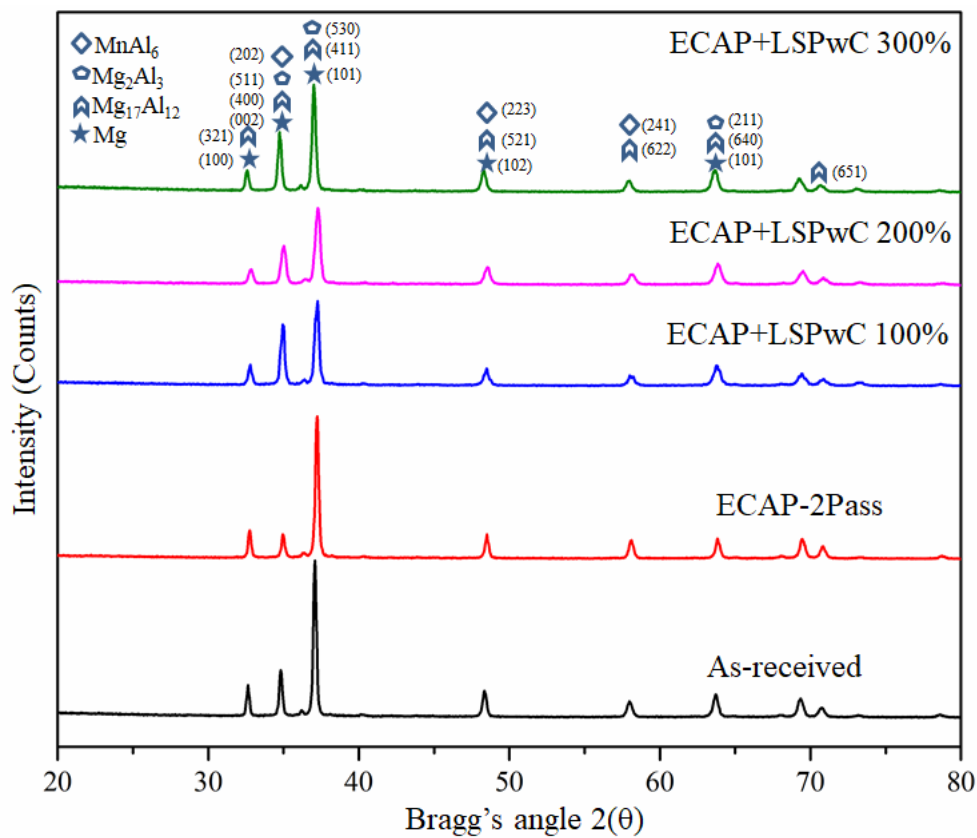


Figure 4.22 XRD patterns of AM80 alloy at different stages of processing for grain refinement

### 4.2.3 Tensile strength

Figure 4.23 shows the stress-strain behaviour of LSPwC processed AM80 samples, processed by ECAP for 2-pass as under route Bc. Energy density was kept constant as  $8 \text{ GW/cm}^2$ , and peening was performed at different coverages of 100 %, 200 % and 300 %. which enhances the tensile strength by small percentage (Wu et al. 2018). Considerable increase in tensile strength and ductility from ECAP to ECAP + LSPwC

processed samples was observed, with respect to percentage of coverage. Tensile strength improved because of grain refinement, as a result of plastic deformation, caused by high strain rate with the evaluations of twins and dislocations (Gencalp et al., 2016; Lu et al. 2010). Grain refinement enhances grain boundaries, facilitates dislocation accumulation capacity, leads to strengthening of material during tensile straining (Ma 2006). Difference in slope within elastic limit represents change in stiffness. LSPwC processed samples possess low stiffness, compared to ECAP processed sample, because of change in hardness at peened surface (Zhang et al. 2016). Distribution of  $Mg_{17}Al_{12}$  plays an important role in improving ductility, as it possesses brittle morphology in cast material, as  $\alpha$ -Mg is surrounded by coarse and reticular manner by  $Mg_{17}Al_{12}$ . Distribution of  $Mg_{17}Al_{12}$ , equiaxed and homogeneous in  $\alpha$ -Mg matrix, improves formability (Jing-yuan et al. 2012).

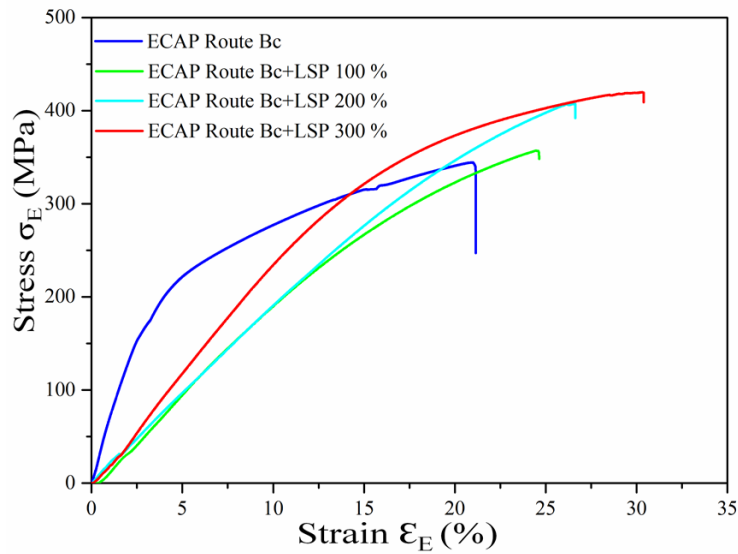


Figure 4.23 Tensile stress-strain behaviour of ECAP processed AM80 with LSPwC at different percentage of coverage

#### 4.2.4 Fracture analysis of tensile failure

Figure 4.24 shows the SEM images of fractured surface of ECAP processed 2-Pass sample, subjected to Surface modification with LSPwC of energy density  $8 \text{ GWcm}^{-2}$ . Surface treatment creates dents due to severe plastic deformation produced by shock waves (Gujba and Medraj 2014). Figure 4.17 shows fracture surface near the machined surface without LSP and nominal surface roughness was observed.

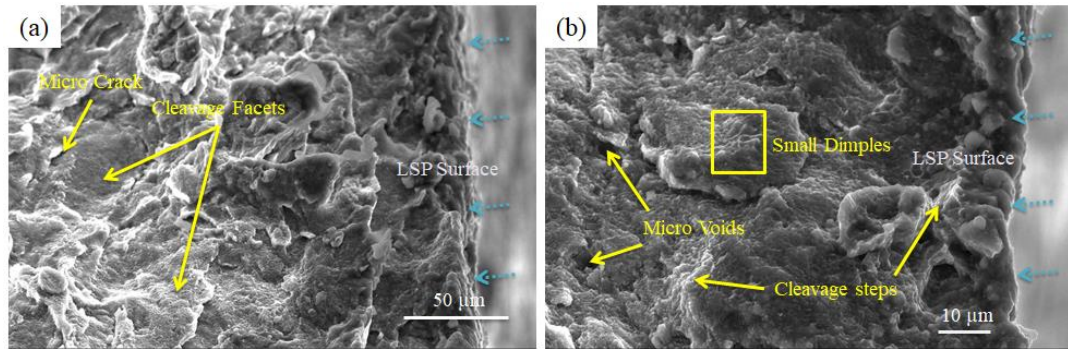


Figure 4.24 SEM Image of fracture surface for LSPwC with 100 % coverage of 2-Pass ECAP processed route B<sub>C</sub> samples

Fractured surfaces on regions other than LSP region appeared similar to ECAP processed 2-pass sample, under route B<sub>C</sub>. Change in hardness near peened surface, delayed crack initiation and fracture occur due to overloading in tensile mode. Slight increase in tensile strength was observed (as shown in figure 4.23). SEM image (figure 4.24 (b)) showed the existence of small micro-crack, cleavage facets by crossing the grain boundaries. Small dimples, created on cleavage facets due to peening, were observed. This evidence provided the effect of LSP on change in secondary phases, due to LSPwC processing. Small dimples indicate ductile fracture and enhancement of ductility (Pineau et al. 2016).

Figure 4.25 show the fracture surface for LSPwC processed sample with 200% coverage on 2 pass ECAP processed sample under route B<sub>C</sub>, with clear indication of formation of small dimples. Ductile fracture propagates with load and it can withstand limited load in regions near to LSPwC processed surface. Further, increase in loads evolves cleavage steps, by coalescence of dimples, as observed in figure 4.25 (a). Once the crack propagates to inside, cleavage will dominate (as the effect of LSPwC loses here) the fracture mode and leads to catastrophic failure, as mixed mode of ductile and brittle fracture. As percentage of dimples increase, more elongation is observed (figure 4.25 (b)) in stress-strain graph on LSP processed with 200% coverage sample.

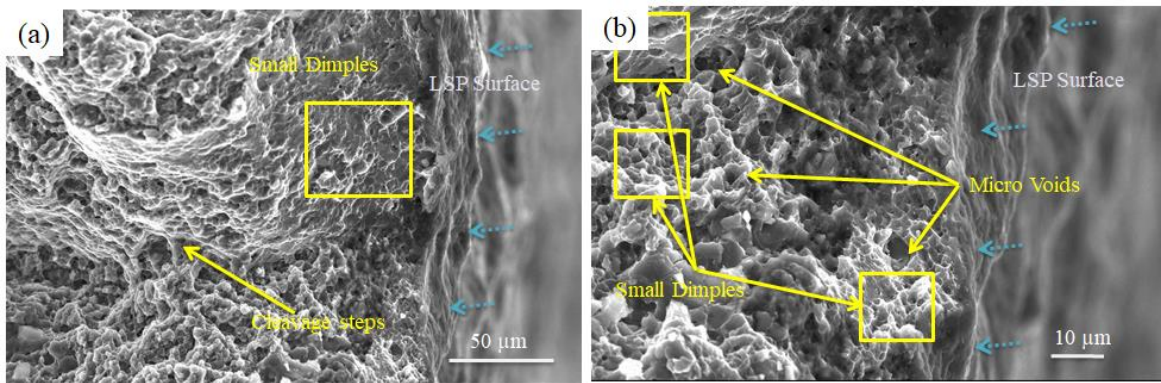


Figure 4.25 SEM Image of fracture surface for LSPwC processed with 200% coverage of ECAP 2-Pass processed route B<sub>C</sub> samples

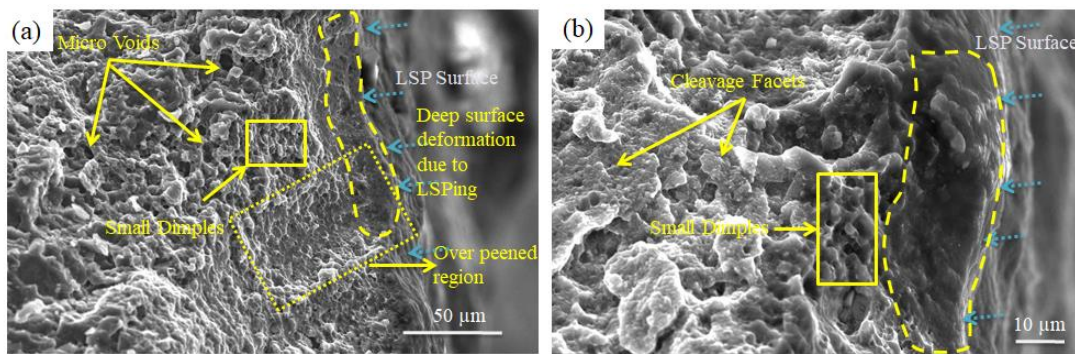


Figure 4.26 SEM Image of fracture surface for LSPwC processed with 300 % coverage of 2-Pass ECAP processed route B<sub>C</sub> samples

Fracture surface of LSPwC processed sample for 300% coverage, on ECAP processed 2- pass sample under route B<sub>C</sub>, is shown in figure 4.26. Difference between peened and non peened region is observed, as a result of peening and further more plastic deformation, and some over-peened regions are observed, as highlighted, in figure 4.26 (a). Many small sized dimples were observed near the peening surface, and voids are nucleated at inclusions which are grown by higher loads. Coalescence of these voids initiates cracks and leads to separation of material (Pineau et al. 2016). Percentage of dimples near the LSPwC processed surface is high, when compared with 100% and 200% samples, hence more ductility is shown in figure 4.23.

### 4.3 Nano indentation

Metals are, as promising as, engineering materials, from past centuries. As engineering field advances, demand for more efficient materials increases. When it comes to structural aspects of mechanical characterization, metals play crucial role, with respect



to, functional aspects. Nano indentation is one of the precise procedures to examine mechanical properties like hardness, elastic modulus, fracture toughness, creep and yield strength at nano level. Macro and micro hardness measurement units have larger tip geometry, deeper indentations and limited spatial resolutions (measurement of area of indentation) which limits obtained results with low accuracy. Nano indentation experiments were executed to analyse mechanical properties at accurate locations, with very precise tip shape (Nano scale), and high spatial resolution, which provide real time load displacement data during the experiment, which enhances the stabilization of results at nano regions.

Nano indentation experiments were carried out for depth of 2000 nm, at strain rate of  $0.05 \text{ S}^{-1}$ , tip TB15269, with a harmonic frequency of 45 Hz and harmonic displacement target of 2 nm. Figure 4.27 shows the indentation mark produced during indentation. At each location, 5 readings were taken to avoid surface uncertainty.

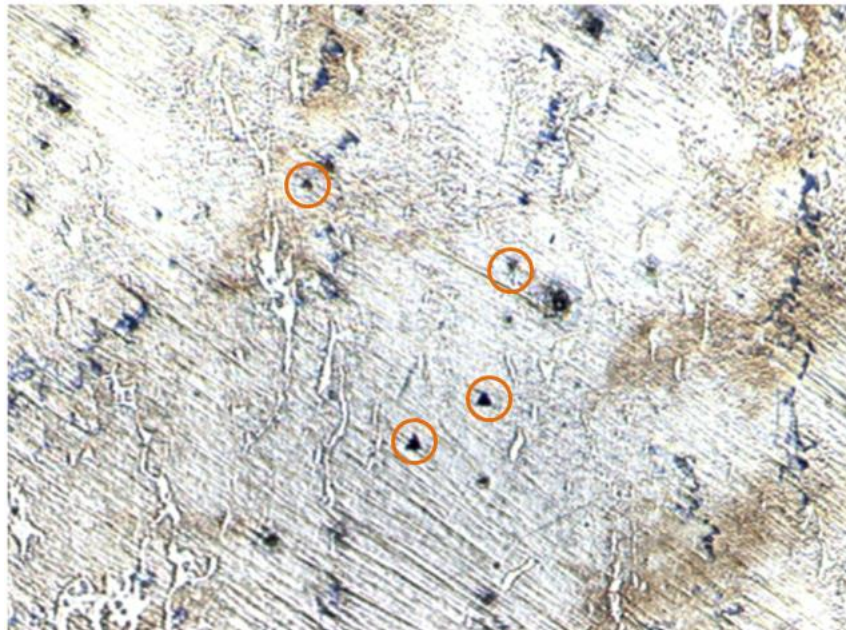


Figure 4.27 Indenter marks after executing the tests on 2-pass ECAP processed sample

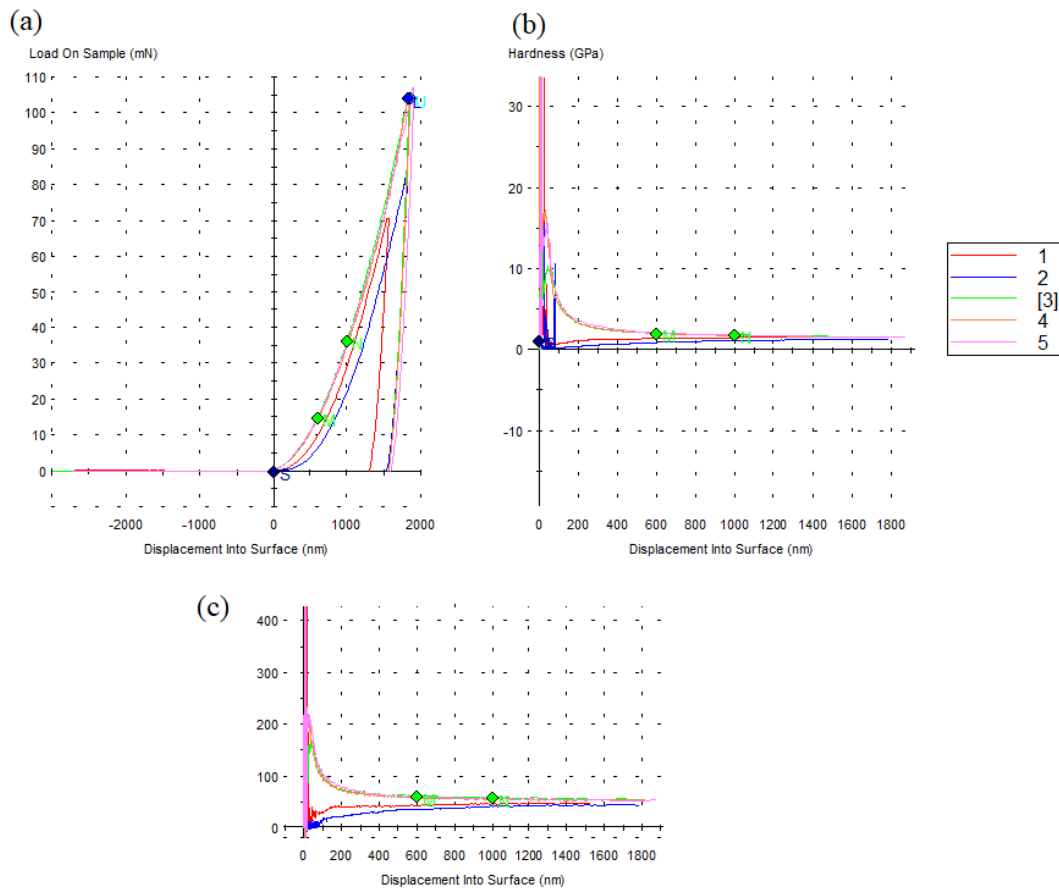


Figure 4.28 shows the data extracted from nano indentation experiment for ECAP 2-pass processed AM80 sample. (a) Load V/s displacement curve, (b) Hardness along the depth and (c) modulus along the depth

Figure 4.28 shows the data extracted from nano indenter, where penetration was associated with trapezoidal load function. Penetration decreases with increase in load. Longer duration of load and fast unloading minimizes viscoelastic effects, that are achieved with trapezoidal load function, which enhances precision of experiments. Figure 4.28 (a) shows load v/s displacement of nano indenter along the depth, and 2000 nm depth was kept as the limit for penetration. Experiments were conducted using high precision load cell with capacitor-based transducer for measurement of displacement. Indenter was penetrated at a rate of 45 times per second in step size of 2 nm during loading. Figure 4.28 (b & c)) show hardness and elastic modulus recorded against depth, during the experiment and it was repeated for 5 trials at each location.

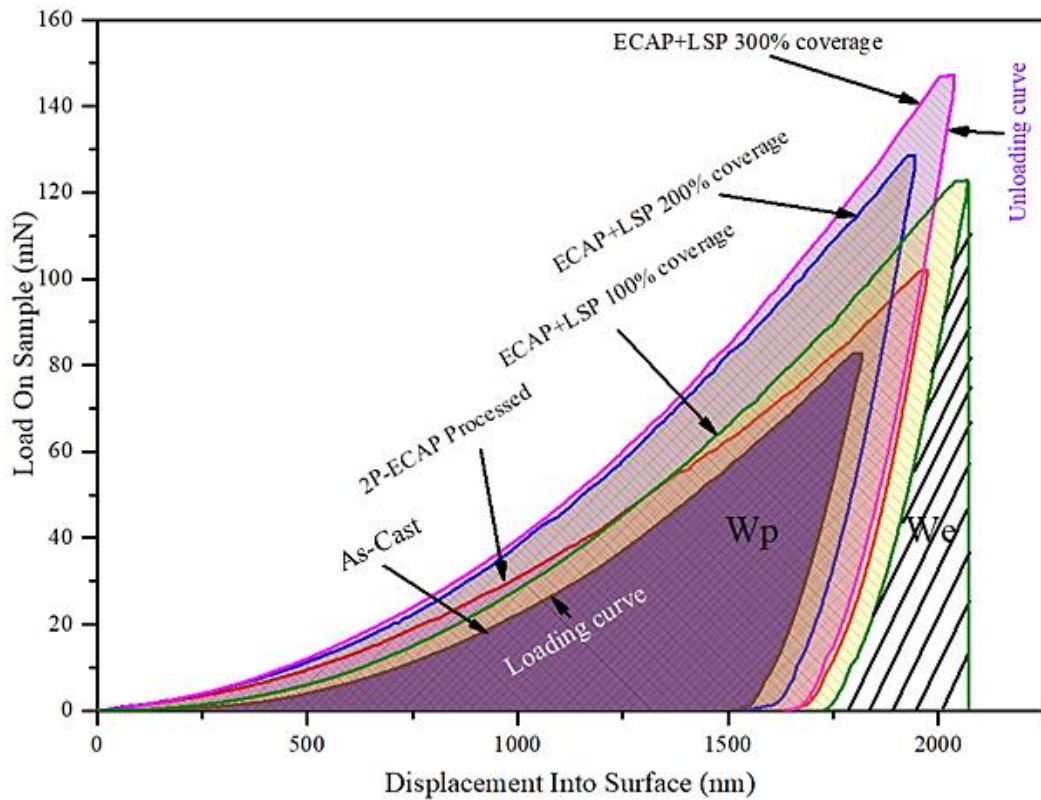


Figure 4.29 Load V/S displacement plot at different processing stage

Typical load-displacement curve of indentation was shown in figure 4.29, which contains the data measured at surface level of peening, as-cast and ECAP processed sample. Loading curve for as-cast sample showed least slope. 2P-ECAP processed sample showed capability for further load bearing capacity. Increase in slope proves stiffer compared to as cast sample. ECAP+LSP 100 % coverage sample showed enhancement in strength and ductility, through change in slope of loading curve and capable of receiving more displacement. ECAP+LSP 200 and 300 % coverage samples showed increase in strength and loss of ductility, which were observed by lower displacements at surface. Area under loading and unloading curve represents energy dissipated during plastic deformation ( $W_{plastic}$ ), and area under unloading curve and vertical line drawn from peak load, gives energy recovered due to relapsing of elastic deformation ( $W_{elastic}$ ). Total work done occurred in two parts, as mentioned below (equation 4-1, (Bao et al. 2004)).

$$W_{Total} = W_{Plastic} + W_{Elastic} \quad (4-1)$$

### 4.3.1 Relation between hardness and depth of peening

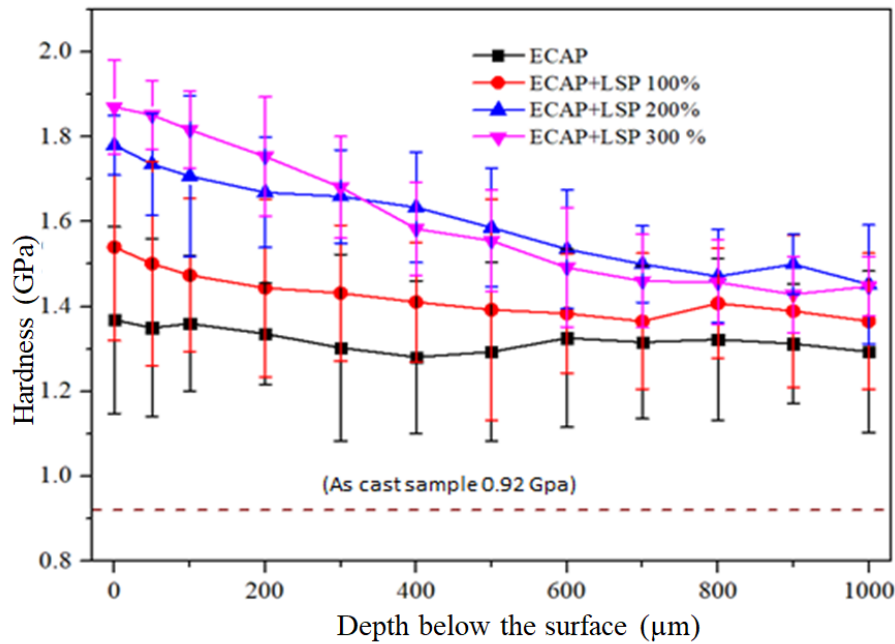


Figure 4.30 Hardness measurement of AM80 sample at different processing stage. Hardness is the resistance offered by material to penetration/scratch. In the present work, scratch is formed by a standard indenter. Figure 4.30 show the plot of hardness measured against depth of peening at different processing stage. Berkovich diamond indenter was used for extracting data, and hardness (H) is calculated as

$$H = \frac{P_{max}}{A} \quad (4-2)$$

As-cast sample showed hardness of 0.92 GPa and it was measured on one surface. processed by ECAP showed hardness of 1.36 GPa and little variation was observed, and minimum was observed at 1.28 GPa. Samples were further processed with LSP for 100, 200 and 300 % of coverage, and hardness increased significantly with increasing percentage of coverage. As LSP is surface treatment process, hardness showed decreasing trend with depth, and is shown in figure 4.30. The samples were targeted to decrease grain size through ECAP and LSPwC, which implies in increase in grain boundaries. As cast sample showed average grain size of 100 μm, which further reduced to 45 μm. LSP on ECAP processed sample showed further grain refinement

showing elongated bands of grains (figure 4.19) with an average width of 100 nm. Effect of grain sizes on indentations is shown in figure 4.31.

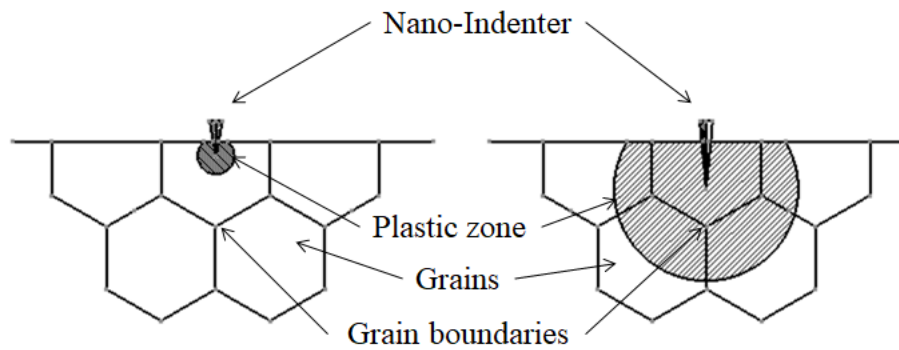


Figure 4.31 Schematic representation of effect of nano-indentation on grain refinement.

Ratio of average grain size and dimension (diameter) of indenter tip decreases with increase in grain refinement. When indenter penetrates the sample, deformation starts in its elastic limit, then further transfers into plastic limit. At the beginning of penetration, plastic zone initiates near the indenter tip and starts growing further away from tip and propagates as the load increases (Somekawa and Schuh 2011). Plastic zone is seen in limited number of grains or a single grain in coarse grain material. For a fine-grained material, number of grains increases in plastic zone. As the number of grains increases in plastic zone, percentage of grain boundaries also increases ( $Mg_{12}Al_{17}$ ), which causes change in resistance for plastic deformation. Hence, penetration to the material decreases with number of indentations, for small grain materials and hardness increases.

Elastic modulus of material defines bonding strength between atoms, which is an intrinsic property, and it is measured as the ratio of stress and strain in elastic region obtained from tensile plot. Depth sensing technique in nano indentation approach gives high precision measurement for mechanical properties in small region. As the samples are processed by different deforming techniques, at surface (by LSPwC) and bulk material (by ECAP), different characteristic features are imposed on the material. Measurement of elastic modulus is an important character to understand the stiffness in deformed regions. Experimental setup continuously measures the applied load and

displacement, then automatically calculates the projected contact area by using inbuilt software. Elastic modulus  $E_r$  is given by

$$E_r = \frac{\sqrt{\pi}}{2\beta} \frac{S}{\sqrt{A}} \quad (4-3)$$

A is the projected contact area at particular displacement, S is the slope of unloading curve and  $\beta$  is the compliance contact parameter for the contact between specimen and indenter (Lu et al. 2009).

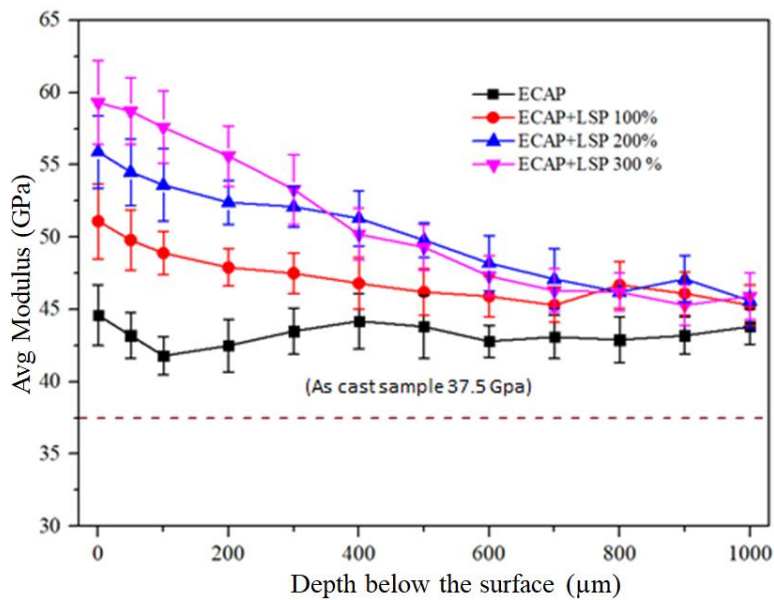


Figure 4.32 Characterization of modulus of AM80 at different processing stage

Figure 4.32 shows the typical variation of elastic modulus of material across the different processing stage, against the depth of material. As-cast samples showed modulus of 37.5 GPa and measurement were made at one surface, because no surface treatment was executed. ECAP processed sample showed elastic modulus of 45 GPa at surface, as measurement across the depth, showed small variations of modulus, due to inhomogeneity in grain size, which may be caused by residual stress present in the grains. Laser shock peened samples with percentage of coverage of 100, 200 and 300 % showed an increase in elastic modulus at surface, as peening effect was high at surfaces, due to plastic deformation and grain refinement. As the effective depth increases, elastic modulus decreased. Hardness and elastic modulus were inversely

proportional to projected contact area of indenter. Hence, both hardness and elastic modulus showed similar behaviour across the processing depth.

#### 4.4 Roughness measurement

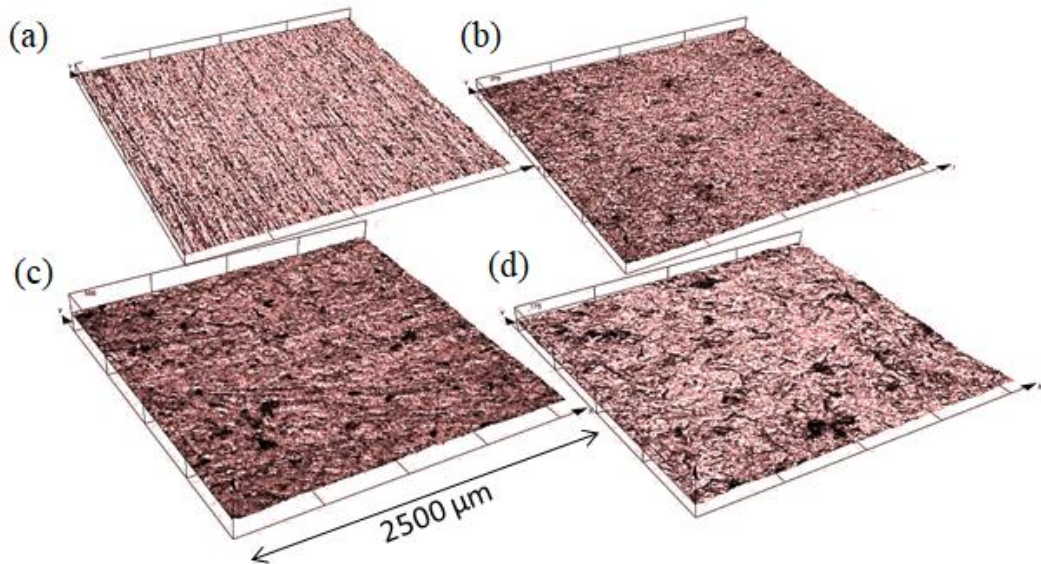


Figure 4.33 Confocal microscopic image of (a) ECAP processed and polished with SiC paper, surface treated with LSPwC (b) 100, (c) 200, (d) 300 % of coverage

Surface roughness ( $R_a$ ) on sample processed by ECAP for 2 passes was estimated as  $0.638 \mu\text{m}$ . With LSPwC of 100 % of coverage, roughness of  $3.584 \mu\text{m}$  was recorded. Plastic deformation caused by plasma blast creates small dents over the surface, and 70 % overlap of laser beam suppress 70% of previous dent, and it formed a new dent, by pushing the work material downwards. Hence, there is a push of material across the circumference of the plasma region (Dai et al. 2016), and formed the dents which are the larger than size of the beam, thereby increasing the surface roughness and is shown in figure 4.33. Impression created by first pulse causes single a dent, and it overlaps with other impression of laser pulse, creating more dents. By repeating peening randomly on already peened surface of 100% coverage, surface roughness increased to  $5.235$  and  $6.824 \mu\text{m}$ , respectively, on samples of 200 and 300 % of coverage. Figure 4.34 shows the comparison of roughness ( $R_a$ ) with respect to coverage of peening.

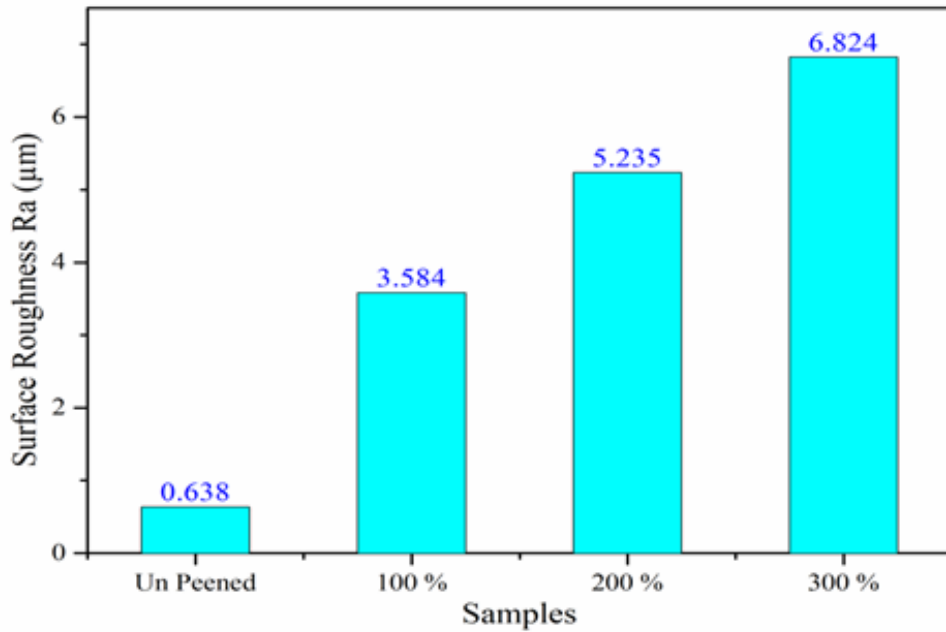


Figure 4.34 Roughness ( $R_a$ ) measurement of peened samples

In LSP without coating, material is directly exposed to high pressure plasma, whereas in LSP with coating, material is exposed high temperature plasma at peening surface, vaporizes transiently, and causes re-solidification of vaporized material because of the presence of water, which is used as working medium. These re-solidified droplets again bonds to material surface and causes increase in surface roughness (Maawad et al. 2012).

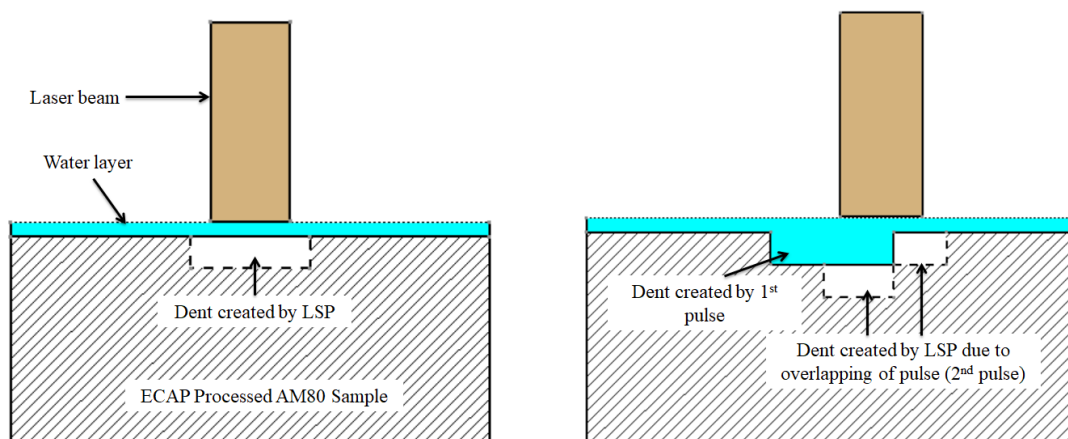


Figure 4.35 Formation of dents (permanent deformation) on the surface



#### 4.5 Wear analysis

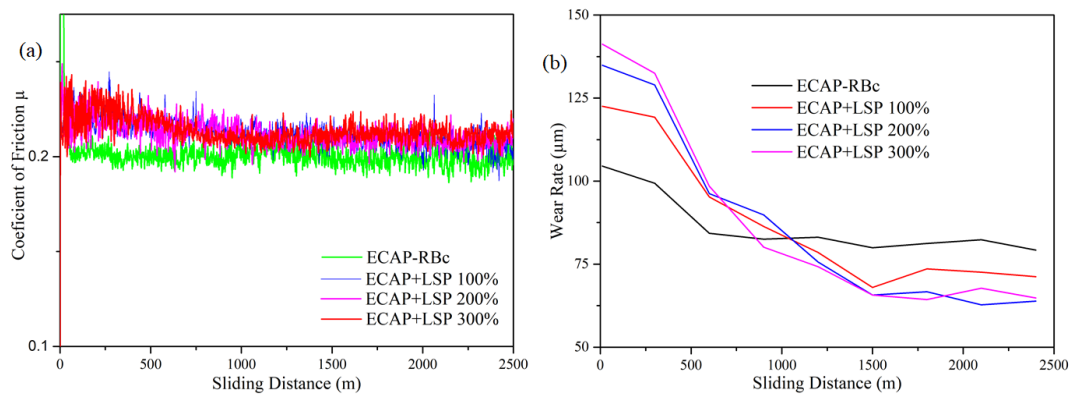


Figure 4.36 (a) Friction coefficients and (b) wear rate of ECAP processed 2-Pass sample under route B<sub>C</sub> additionally surface treated with LSPwC AM80 alloy

Wear characterization were executed to investigate and to understand wear mechanism. Figure 4.36 (a) shows the relation between friction coefficients and sliding distances, at a load of 40 N. ECAP processed (2-pass) samples showed no change in coefficient of friction with sliding distance. Grain refinement occurred throughout the sample and hardness increased, all over the sample and it possessed uniform high hardness compared to other ECAP passes (Gopi et al. 2017a). LSP created plastic deformation at surface, in the form of dents, developed at high strain rate during SPD, and causes further grain refinement at the surface (Lou et al. 2016; Ren et al. 2015). This lead to increase in hardness near the surface (Shen et al. 2017). Coefficient of friction, at the surface of LSPwC processed samples, were slightly higher than, in ECAP processed samples and starts to decrease with increase in sliding distance, due to wear of material. LSPwC was done at different percentage of coverage and 300% coverage sample showed better resistance to wear. Figure 4.36 (b) shows the behaviour of wear rate with respect to sliding distance. ECAP sample showed better resistance to wear rate at early stage compared to LSPwC processed sample. Wear rate of LSPwC sample increased with coverage percentage during early stages, because of increase in surface roughness (loss of contact surface) and starts to decrease with increase in coverage percentage. Samples, with 300% coverage, possess high surface roughness because of repeated peening and deep dents cause non uniform contact against steel disc. Wear rate decreases, as surface become uniform, as material starts to wear. Once worn surface

turn to uniform surface, wear rate reduces to a minimum value, because of high hardness.

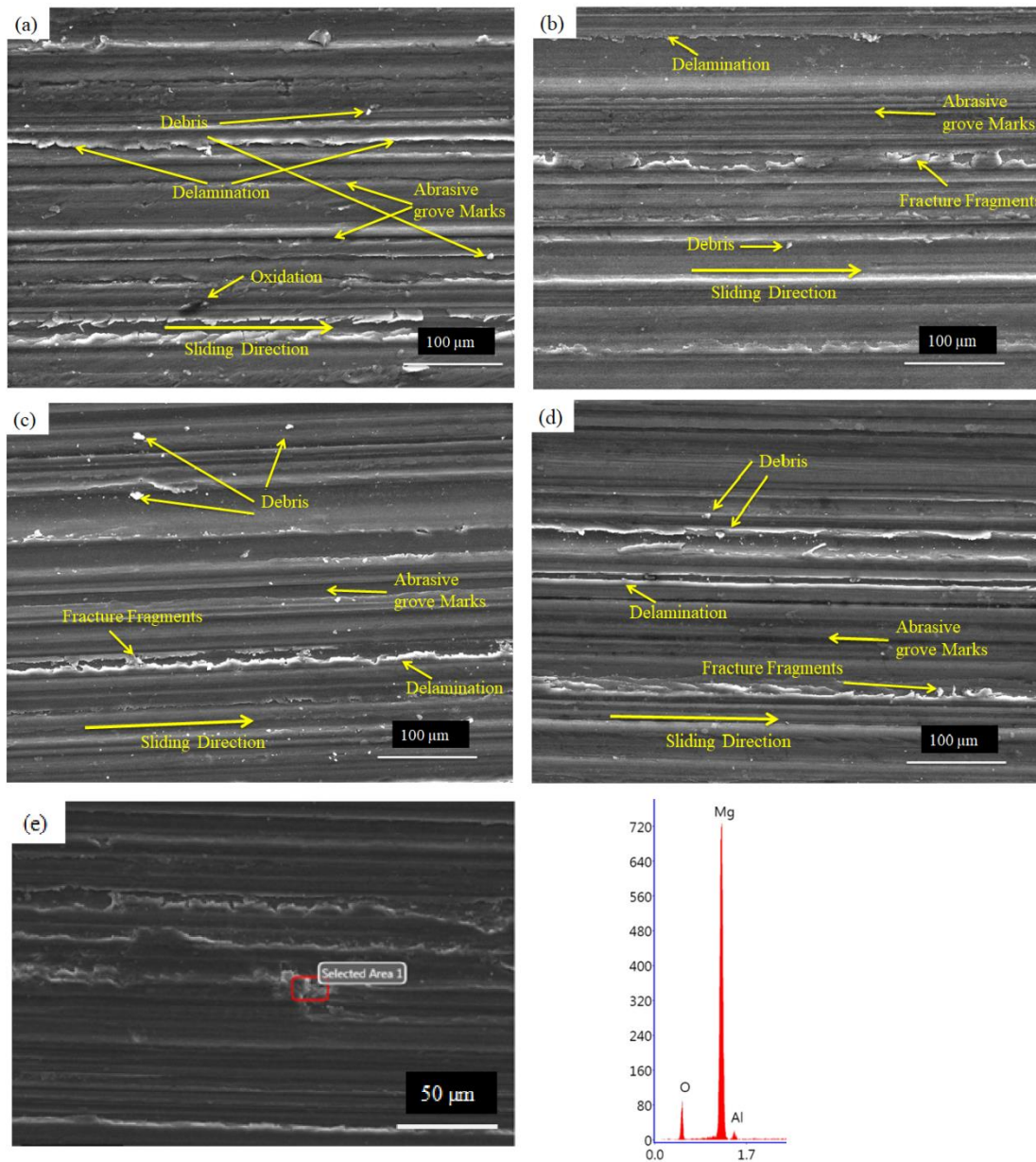


Figure 4.37 SEM images of worn surfaces of (a)ECAP processed 2-Pass sample under route Bc (b) ECAP processed with LSPwC 100% coverage (c) 200% coverage (d) 300% coverage and (e) EDS image of worn surface with elemental mapping

SEM images of worn surfaces of 2-pass ECAP processed sample and ECAP-LSPwC processed samples with different coverage percentage are shown in figure 4.37. Worn surfaces consists of grooves in the direction of sliding, caused by plastic deformation, occurred by abrasive wear mechanism. Surface roughness increases with abrasive

grooves and causes increase in friction coefficients (Rams et al. 2014). Width of abrasive groove marks depends on size of debris. Delamination occurred because of detachment of material caused by cracks perpendicular to sliding direction. Figure 4.37 (a) shows worn surface of ECAP processed sample having abrasive wear with delamination. Deep plough marks indicate an increase in surface roughness and softness of material compared to LSPwC processed samples.

Figure 4.37 (b, c & d) show worn surfaces of ECAP-LSPwC processed sample with 100, 200 and 300% of coverage. Surface became smoother after wear, compared to ECAP processed sample, because of increase in hardness by LSPwC. Figure 4.37 (e) shows the elemental mapping of energy dispersive X-Ray spectrometer near delamination region. Traces of oxygen were found on worn surface. Oxidation will be one of the dominating wear mechanisms in Mg based alloys and causes easy detachment of oxidised fragments (Zhang et al. 2018). These fragments are responsible for abrasive wear and also found in all samples.

#### 4.6 Residual stress Analysis

Measurement of stress is based on measuring value of strain and converting into stress value based on Hook's law. Hence, measurements of strain at atomic levels were carried out using X-ray diffraction method.

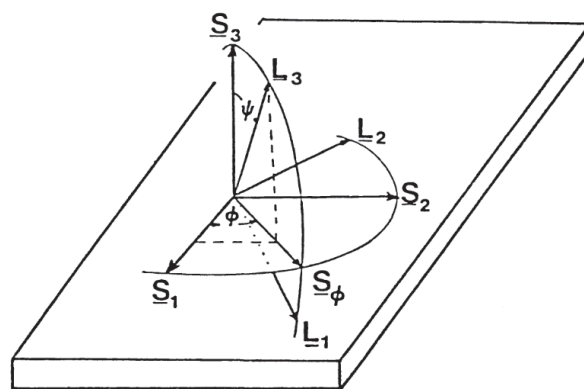


Figure 4.38 Schematic representation of co-ordinate system for measurement of d space for measuring residual strains

$S_i$  represents the coordinates of specimens, with respect to, surface considered for the measurements,  $L_i$  represents laboratory system used to measure normal directions ( $L_3$ ) of hkl planes, whose spacing are measured by diffraction.  $L_2$  lies in the planes  $S_1$  and

$S_2$  and makes an angle  $\phi$  with  $S_2$ . Here, prime tensor quantities were referred to laboratory system (L) and unprime tensor quantities referred to sample coordinate system (S). Lattice space ( $d_{\phi\psi}$ ) was obtained through peaks of diffraction for given hkl reflection, Normal strain ( $\epsilon_{33}$ ) along with  $L_3$  is obtained.

$$\begin{aligned}
 (\epsilon_{33})_{\phi\psi} &= \frac{d_{\phi\psi} - d_0}{d_0} \\
 &= \epsilon_{11} \cos^2 \phi \sin^2 \psi + \epsilon_{12} \sin 2\phi \sin^2 \psi \\
 &+ \epsilon_{22} \sin^2 \phi \sin^2 \psi + \epsilon_{33} \cos^2 \phi + \epsilon_{13} \cos \phi \sin 2\psi \\
 &+ \epsilon_{23} \sin \phi \sin 2\psi
 \end{aligned} \tag{4-4}$$

Where  $d_0$  is the stress-free lattice spacing.

Basic elemental diffraction pattern is shown in figure 4.25, and the peak at 63.5 was selected for the analysis of residual stresses. Figure 4.39 shows the diffraction peaks extracted from X-Pert pro, at  $2\theta = 60$  to  $66^\circ$ ,  $\phi = 0$  and  $\psi = -40, -35.09, -29.86, -23.91, -16.71, 0, 16.71, 23.91, 29.86, 35.09$  and  $40^\circ$ . In similar way, diffraction peaks are extracted for  $\phi = 45$ , and  $90$ . Lattice spacing for each diffraction peak is extracted and tabulated in table 4.1.

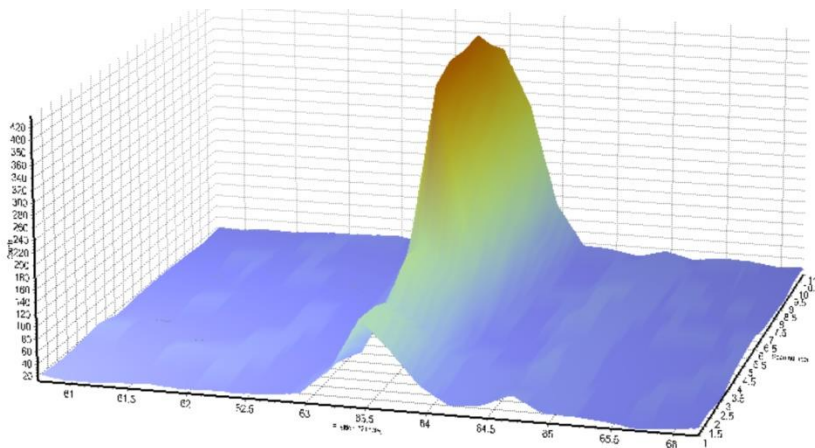


Figure 4.39 shows the diffraction peaks extracted from Xpert pro, at  $2\theta = 60$  to  $66^\circ$ ,  $\phi = 0$  and  $\psi = -40$  to  $40^\circ$

Figure 4.40 shows the plot of lattice spacing against  $\sin^2 \psi$ . There are totally 33 measurement, 11 diffraction measurement were carried at each of the angles of ( $\phi$ ) 0, 45 and  $90^\circ$ , and the plots showed split in d value, because of non-zero values of  $\epsilon_{13}$  and  $\epsilon_{23}$  (Noyan C and Cohen B 1986). To solve the linear equation 4-4, which is having

unknowns  $\epsilon_{11}$ ,  $\epsilon_{12}$ ,  $\epsilon_{22}$ ,  $\epsilon_{33}$ ,  $\epsilon_{13}$  and  $\epsilon_{23}$ , measurement of  $d_{\phi\psi}$  along six independent directions is required. But, to increase the accuracy of results, more directions are measured ( $\phi = 0, 45, 90$ ).

Table 4.1 X-ray diffraction data for d-spacing at surface of ECAP processed sample

Scan	Peak	Psi	$\text{Sin}^2\psi$	$\phi$	Peak	Corr.	d-spacing	h	k	L
No.	No.	( $^\circ$ )	(-)	( $^\circ$ )	( $^\circ$ ) $2\theta$	( $^\circ$ ) $2\theta$	( $\text{\AA}$ )			
28	28	0	0	180	63.3977	63.3977	1.46597	3	1	1
29	29	16.71	0.083	180	63.4535	63.4535	1.46481	3	8	5
30	30	23.99	0.165	180	63.4815	63.4815	1.46423	4	3	5
31	31	29.86	0.248	180	63.5104	63.5104	1.46364	4	3	9
32	32	35.09	0.33	180	63.5305	63.5305	1.46322	5	1	8
33	33	40	0.413	180	63.5475	63.5475	1.46287	6	3	4
27	27	16.71	0.083	0	63.3831	63.3831	1.46627	3	7	1
26	26	23.99	0.165	0	63.387	63.387	1.46619	3	9	2
25	25	29.86	0.248	0	63.3963	63.3963	1.466	3	6	8
24	24	35.09	0.33	0	63.4038	63.4038	1.46584	5	5	3
23	23	40	0.413	0	63.4279	63.4279	1.46534	5	2	2
6	6	0	0	90	63.3886	63.3886	1.46616	3	5	2
7	7	16.71	0.083	90	63.3366	63.3366	1.46723	3	2	8
8	8	23.99	0.165	90	63.3198	63.3198	1.46758	4	7	2
9	9	29.86	0.248	90	63.3198	63.3198	1.46758	5	4	6
10	10	35.09	0.33	90	63.3239	63.3239	1.4675	5	0	3
11	11	40	0.413	90	63.3329	63.3329	1.46731	5	9	9
5	5	16.71	0.083	270	63.4707	63.4707	1.46446	3	8	9
4	4	23.99	0.165	270	63.5046	63.5046	1.46376	3	8	5
3	3	29.86	0.248	270	63.5214	63.5214	1.46341	4	8	2
2	2	35.09	0.33	270	63.5382	63.5382	1.46306	4	6	8
1	1	40	0.413	270	63.555	63.555	1.46272	7	3	3
17	17	0	0	135	63.3989	63.3989	1.46594	3	7	3
18	18	16.71	0.083	135	63.387	63.387	1.46619	4	1	2
19	19	23.99	0.165	135	63.3933	63.3933	1.46606	4	1	0
20	20	29.86	0.248	135	63.4108	63.4108	1.4657	4	1	7
21	21	35.09	0.33	135	63.4134	63.4134	1.46564	4	9	7

22	22	40	0.413	135	63.4287	63.4287	1.46533	6	6	3
16	16	16.71	0.083	315	63.4301	63.4301	1.4653	3	6	3
15	15	23.99	0.165	315	63.4537	63.4537	1.46481	3	9	3
14	14	29.86	0.248	315	63.471	63.471	1.46445	4	9	1
13	13	35.09	0.33	315	63.4878	63.4878	1.4641	5	9	7
12	12	40	0.413	315	63.5046	63.5046	1.46376	6	7	6

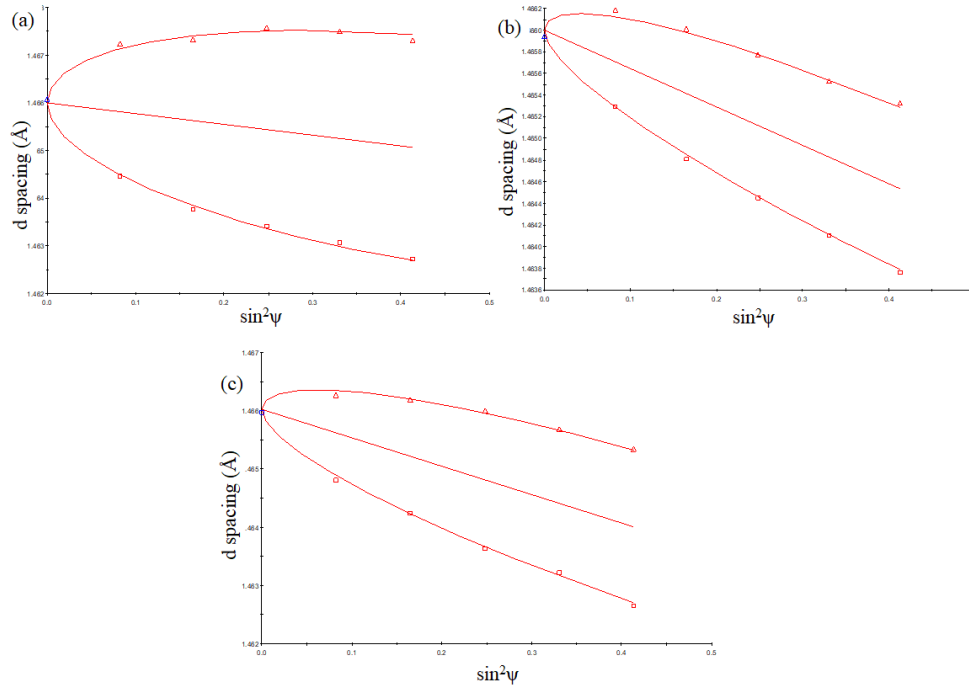


Figure 4.40 Lattice spacing  $d$  against  $\sin^2\psi$  for (a)  $\phi = 0^\circ$ , (b)  $\phi = 45^\circ$ , and (c)  $\phi = 90^\circ$  for ECAP processed sample at surface

By solving the equation 4-4, the strain tensor  $\epsilon_{ij}$  is presented as

$$\epsilon_{ij} = \begin{bmatrix} \epsilon_{11} & \epsilon_{12} & \epsilon_{13} \\ \epsilon_{12} & \epsilon_{22} & \epsilon_{23} \\ \epsilon_{13} & \epsilon_{23} & \epsilon_{33} \end{bmatrix} \quad (4-5)$$

Once the strains are identified, the relevant surface stress ( $\sigma_{ij}$ ) is calculated by Hooke's Law

$$\sigma_{ij} = C_{ijkl}\epsilon_{kl} \quad (4-6)$$

Where  $C_{ijkl}$  is the elastic stiffness coefficient, depends on Young's Modulus ( $E$ ) and Poisson's ratio ( $\nu$ ). This process is repeated for all other calculations of residual stresses at different steps. Material was removed by electro polishing for measurement of  $d$  space value at desired depth of specimen, by using perchloric acid as the electrolyte.

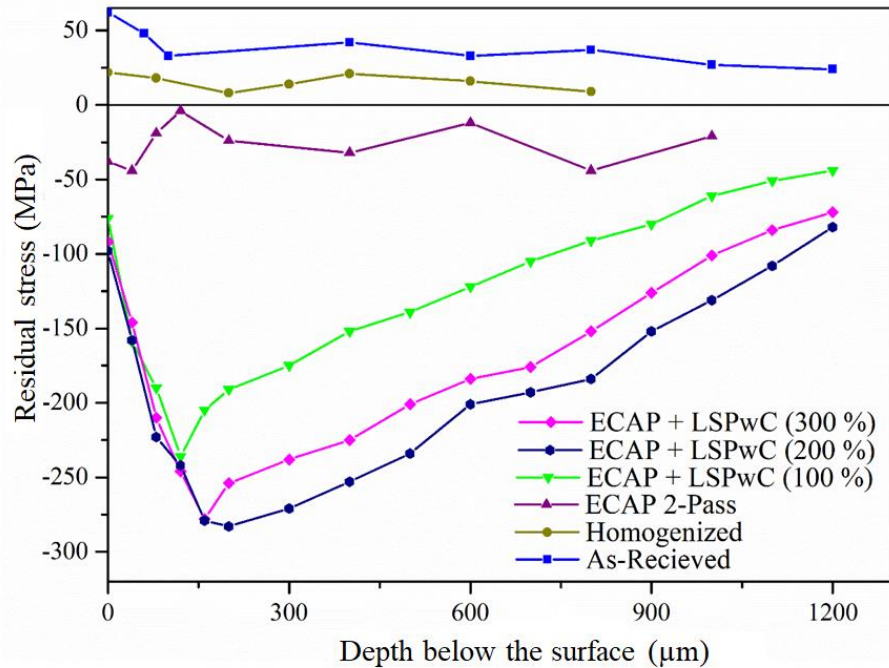


Figure 4.41 variation of residual stress with respect to depth below the surface for different processing condition

Figure 4.41 shows the nature of residual stresses, at each stage of processing are explained. Tensile profile of residual stress was observed in as-cast sample, because of material contraction, during solidification of metal. Homogenised sample showed decrease in stress from 65 to 25 MPa, because of stress relieving, occurred during grain growth. When molten metal is poured into the die, during casting, it starts to solidify, and shrinks in itself. This causes tensile stresses after casting of metals or alloys (Jacot et al. 2000). 2-pass ECAP processed sample showed compressive stress, and variations in magnitude of residual stress at different intervals of depth (Hosaka et al. 2017). Applied strain during ECAP is not uniform across the compressive shear plane. Hence, variation of magnitude is found. High dislocation densities are observed in samples processed by ECAP and are shown figure 4.2, which results in inducing residual stresses and also improves corrosion resistance (SONG et al. 2009). Further increase of

compressive residual stress was observed with LSPwC, and intensity of stress increases from -235 to -280 MPa for 100 to 300 % of coverage. During ECAP, simple shear was introduced to deform the specimen by applying intensive large strain, which ends up with no change in cross sectional dimension. Internal destruction occurred between grains, because of, applied strain during refinement, and causes shrinkage in grain, due to compressive shear. The sample may not fully recover from the applied strains after grain refinement, because of permanent deformation, along the cross section, which leads to accumulation of compressive residual stresses. LSPwC enhanced the magnitude of surface compressive residual stress significantly, and compressive residual stresses were found to be in the range of 100 to 200  $\mu\text{m}$  from peened surface. Figure 4.41 shows that, the rate of residual stresses induced for 100, 200 and 300 % of coverage, is not uniform, and each impact decrease the effect of LSPwC. This may be due to the resistance caused for plastic deformation through peening, after first impact, because of increase in hardness. This also may cause reduction in pressure of shock wave which penetrates the material surface (Nie et al. 2014).

#### **4.7 Fatigue analysis**

Fatigue is an important characterization, where the loading part of the material undergoes progressive repetitive damage at localized loads. Failures, due to fatigue loads, occur catastrophically with small warnings. Hence, identifying fatigue characteristic of material is very important for real applications, as most of the components were designed for multiple uses.

In the present work, fatigue was characterized at a maximum load of 120 MPa, with stress ratio of 0.125. Figure 4.42 shows the results extracted from fatigue testing. Tests were executed on as-cast, 2-pass ECAP processed at route B<sub>C</sub>, ECAP+LSP processed samples at 100, 200 and 300%. There was no any macroscopic change in dimension of fatigue specimen after LSPwC, and tests were conducted without any surface treatment after peening.



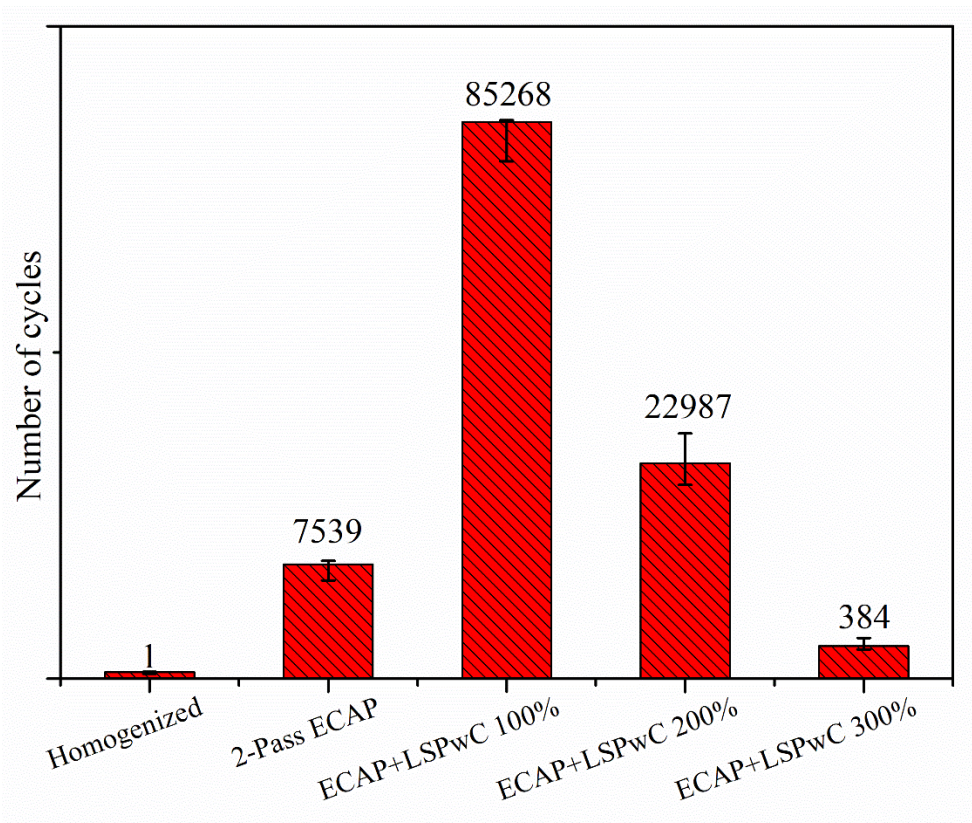


Figure 4.42 Fatigue life of AM80 alloy at different processing stage

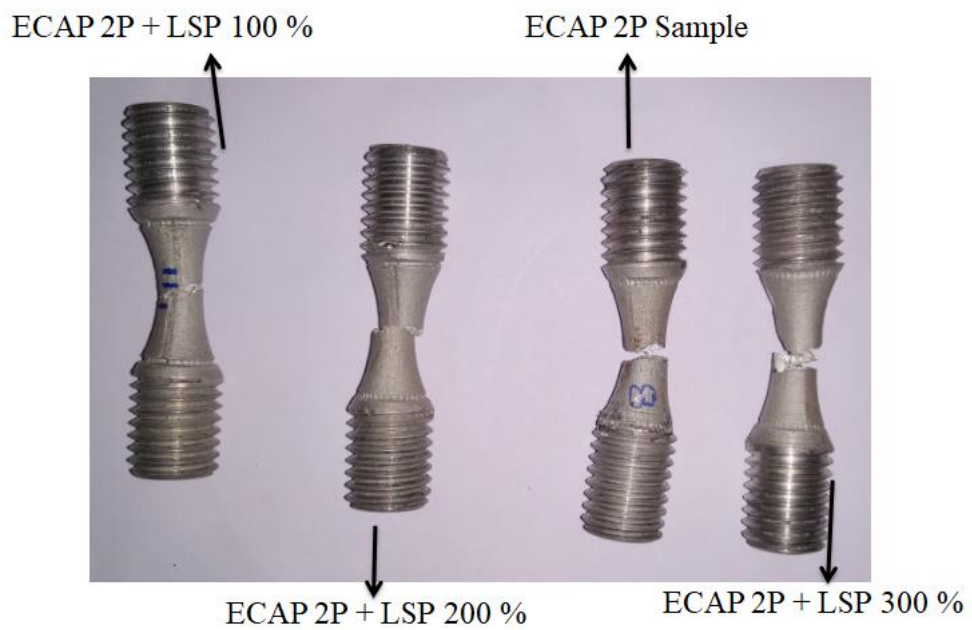


Figure 4.43 Fractured specimens after fatigue testing

Fatigue test were conducted at maximum stress of 120 MPa and minimum stress of 15 MPa, which led to stress ratio (R) of 0.125. As-cast sample hardly took a stress of 120 MPa, and failed at 2<sup>nd</sup> cycle, as it showed low strength during tensile testing (figure 4.10). ECAP strengthens the material by grain refinement and correlates with Hall-Petch Equation (Kulyasova et al. 2009), and induces compressive residual stress (figure 4.41). Fatigue life was increased to 7,539 cycles. ECAP-LSPwC processed sample, with 100 % of coverage, enhanced the life of the component to 85,268 cycles. Compressive residual stress has an advantage for delaying crack initiation and propagation, because of tensile stress (Nie et al. 2014), which enhances the fatigue threshold of peened region.

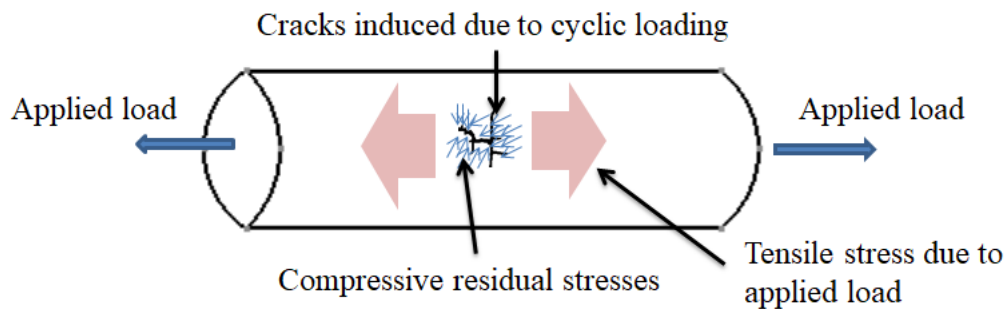


Figure 4.44 Effect of compressive residual stresses during fatigue loading

Compressive residual stresses are significantly potential to reduce micro cracks generated while loading. Further, increase in LSPwC by 200 and 300 % of coverage, decrease fatigue life to 22,987 and 384 cycles, respectively. Decrease in fatigue life was observed with increase in percentage of coverage. Figure 4.44 shows the schematic of a sample under tensile load, which is a part of fatigue load cycles. Cracks were initiated by microstructural damage at weak section, due to formation of microcracks or voids. Tensile stresses are more prone to induce dislocation pile ups at stress concentrated region, compared to compressive stresses (Ritchie 1998). Summation of applied tensile stress with existing surface compressive stress and compressive stresses, because of ECAP (figure 4.41) decrease resultant magnitude in tensile range. Hence, effective stresses on the sample decreased. Even though, if small cracks occur at surface, due to loading, compressive residual stresses, existing at the surface level, heals the crack by compressing it.

#### 4.7.1 Fracture analysis of fatigue samples

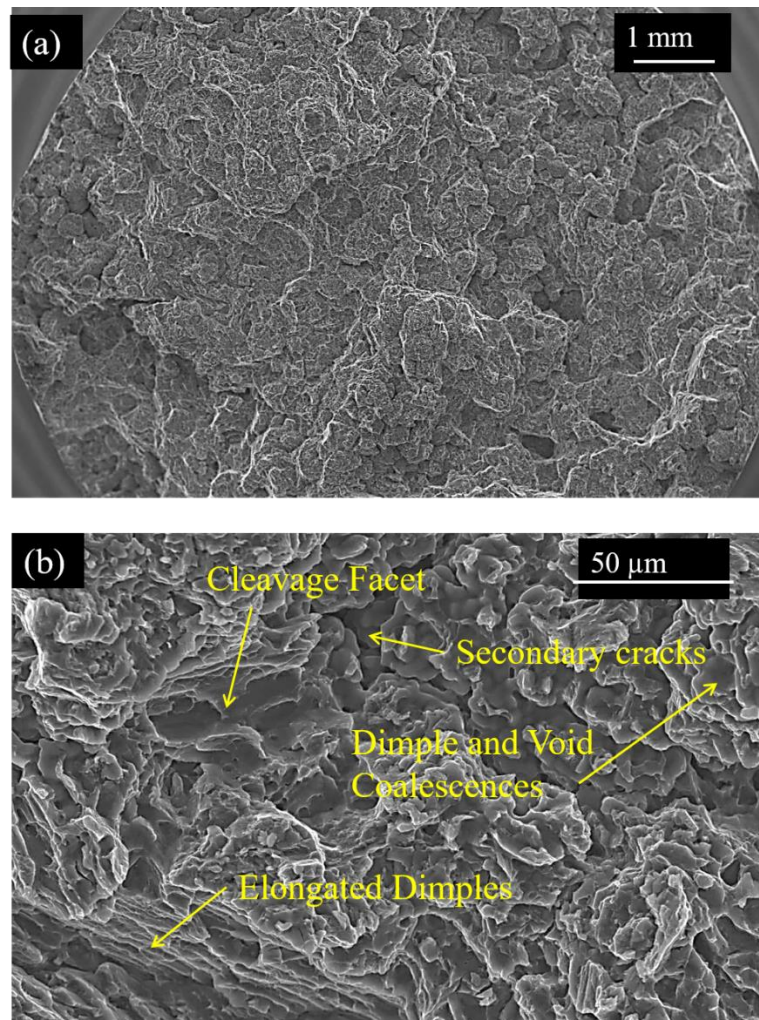


Figure 4.45 Fracture topography of as cast AM80 alloy due to fatigue failure

Figure 4.45 shows SEM micrographs of as-cast sample, ruptured after first cycle of loading, because of low tensile strength, as the sample consists of dendritic grains (figure 4.1) due to fast cooling rate during solidification. Figure 4.45 (b) shows fractured surface, dominated by dimples of different sizes, secondary cracks, cleavage facets and elongated dimples. Appearance of dimples justify the occurrence of fracture, because of void coalescence, and secondary phase particles or inclusions, which are responsible for formation of voids (Pineau et al. 2016). Secondary cracks revealed poor formability, as the expansion of micro cracks induced failure of sample (Lü et al. 2000). Elongated dimples were formed due to dendritic grain structure, and cleavage facets with shear lip revealed transition of brittle to ductile.

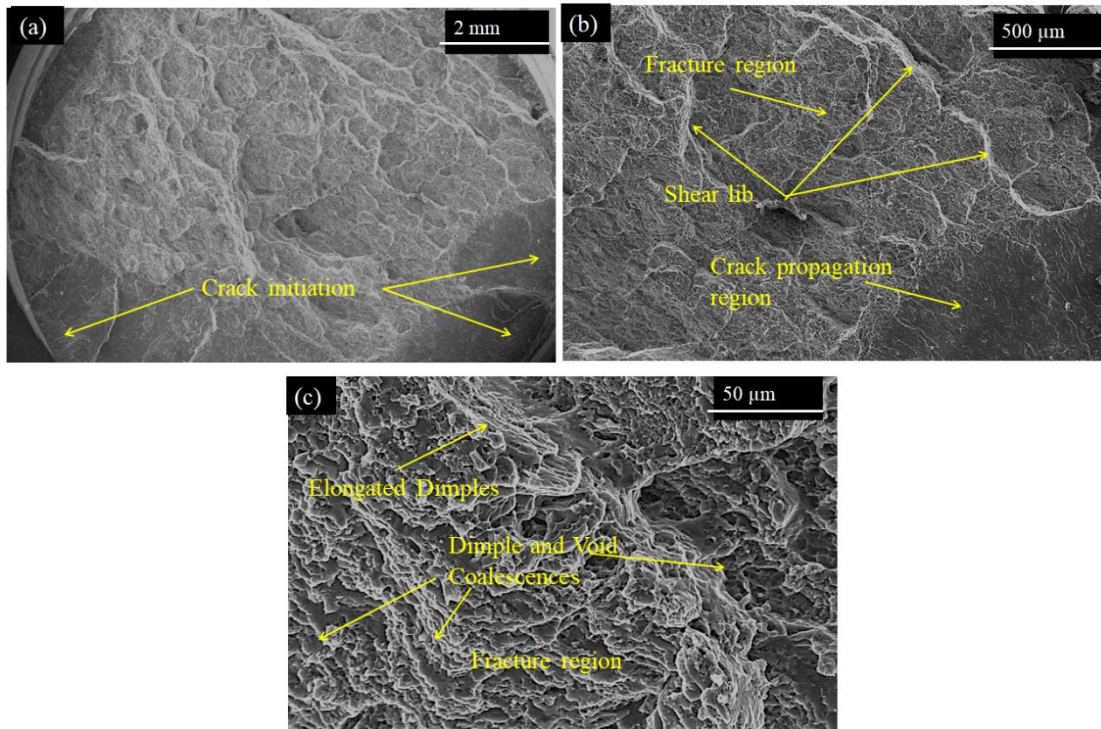


Figure 4.46 Fracture topography of 2-pass ECAP processed at route Bc AM80 alloy due to fatigue failure

Figure 4.46 shows SEM images of 2-pass ECAP processed sample under fatigue loading. Sample ruptured after 7539 life cycles. Increase in tensile characteristics was reported after ECAP from as-cast sample, 2-pass ECAP processed samples possess bimodal grain structure. There was change in residual stress profile from tensile to compressive, which enhance fatigue characteristics. Figure 4.46 (a) shows the initiation of crack at multiple locations on the circumferential surface in peened region. Figure 4.46 (b) shows crack propagation region, which reveals time delay in between crack initiation and fracture. Presence of shear lip exposes the progress of fracture at different planes along loading direction. Figure 4.46 (c) shows the detailed view of fracture mode, where dimples of different sizes are formed. Small dimples need more energy for fracture, compared to large ones, hence strength was increased.

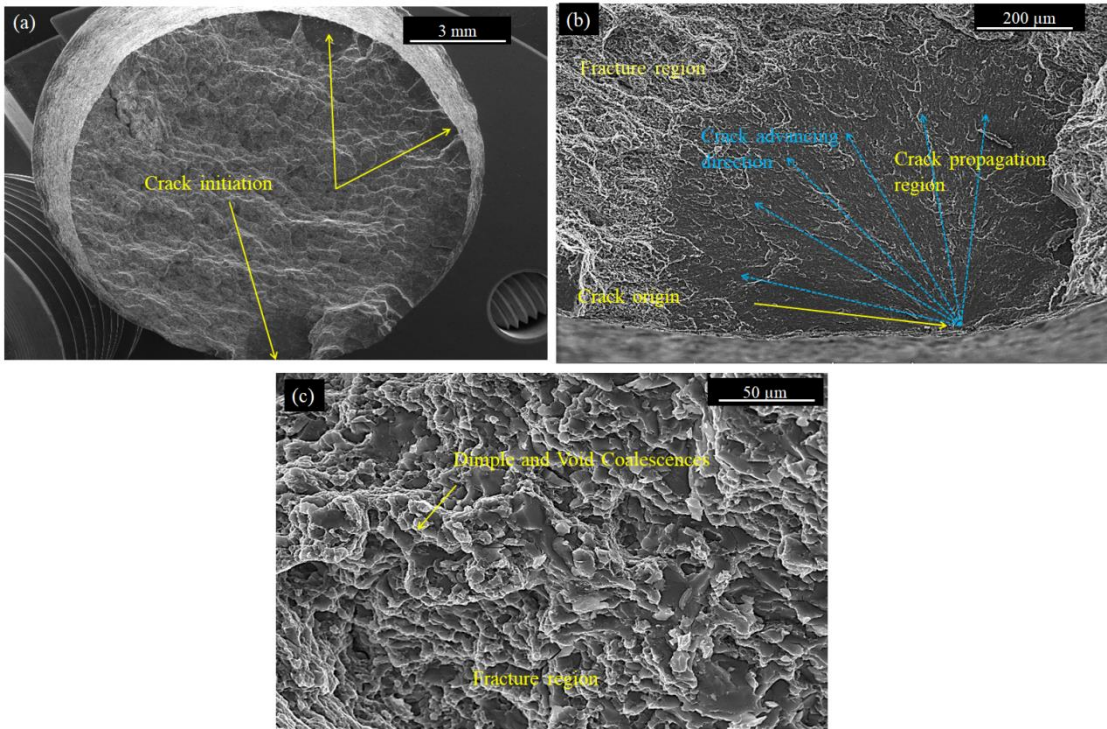


Figure 4.47 Fracture topography of 2-pass ECAP+LSP 100% coverage processed at route B<sub>C</sub> AM80 alloy due to fatigue failure

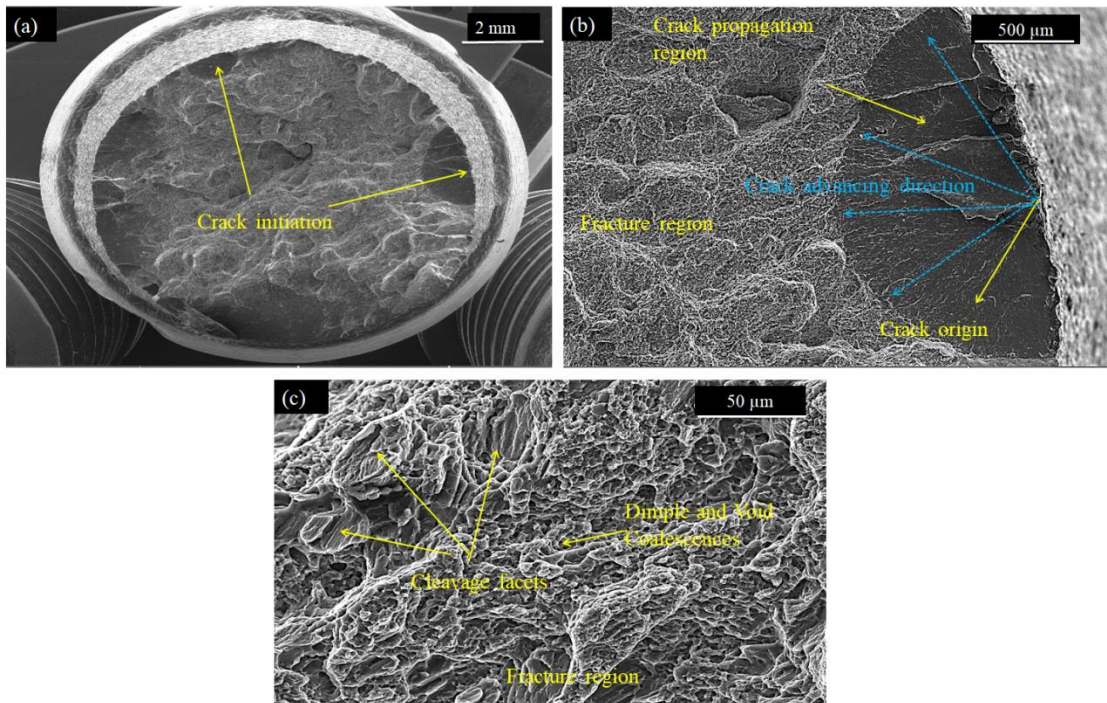


Figure 4.48 Fracture topography of 2-pass ECAP+LSP 200% coverage processed at route B<sub>C</sub> AM80 alloy due to fatigue failure

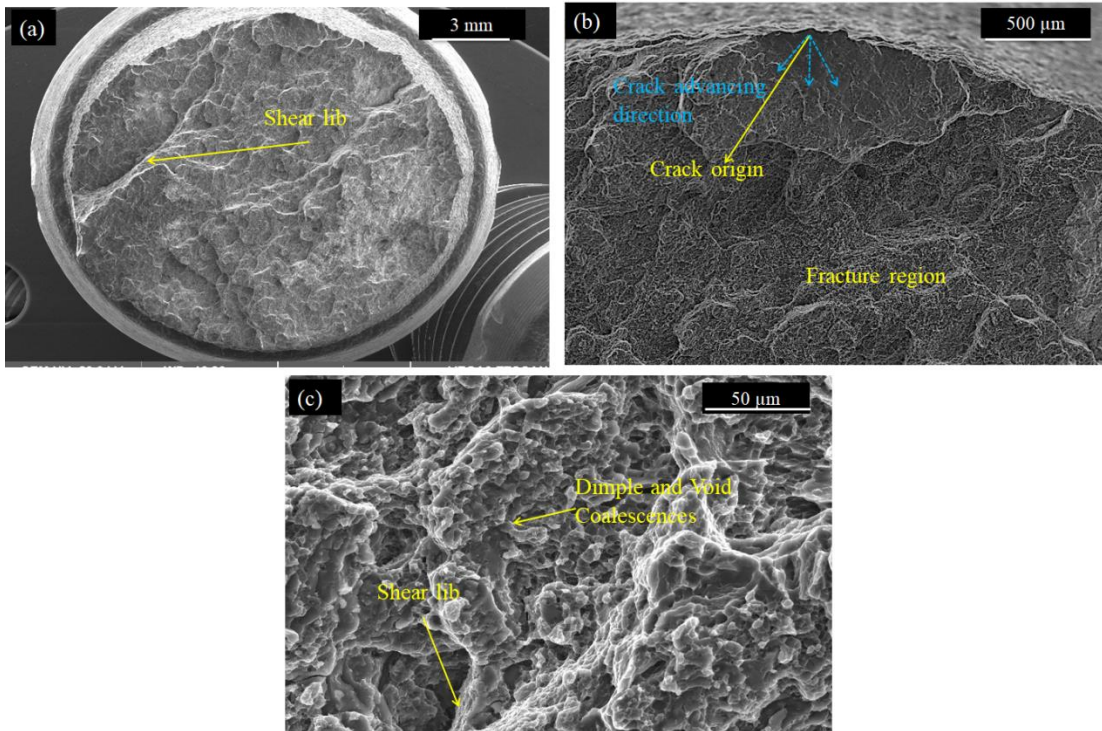


Figure 4.49 Fracture topography of 2-pass ECAP+LSP 300% coverage processed at route B<sub>C</sub> AM80 alloy due to fatigue failure

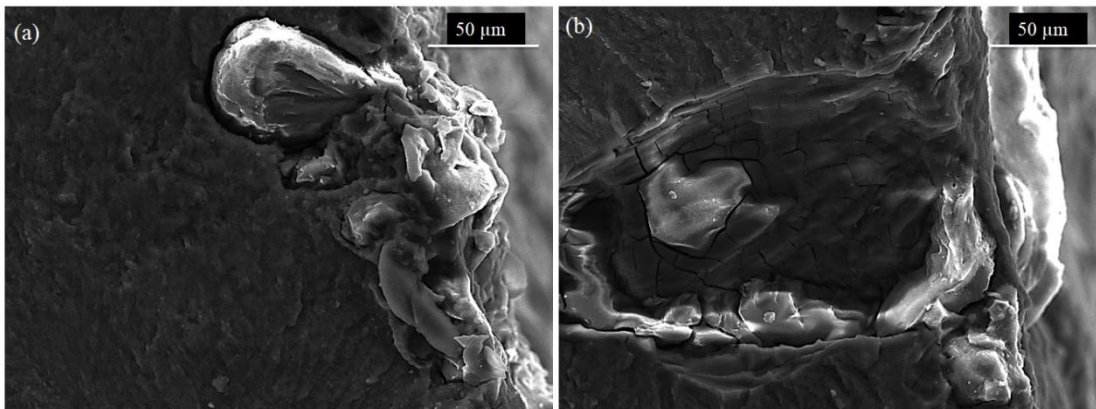


Figure 4.50 surface defects observed at fracture topography of 2-pass ECAP+LSP 200 and 300 % coverage processed at route B<sub>C</sub> AM80 alloy

Figure 4.47 shows fracture surface for ECAP-LSPwC sample with 100 % of coverage, fatigue life of sample increased to 85,268 cycles. Cracks initiated at surface, and propagated towards the centre of sample. LSPwC induces compressive stress of 220 MPa at circumference, and causes delay in crack initiation and propagation, while loading. Fracture region was found to be similar to ECAP processed samples, because effect of LSPwC was limited, to small depths near surface. Figure 4.48 & 4.49 show fracture regime of ECAP-LSPwC sample with 200 and 300 % of cover, where fatigue

life decreased to 22,987 and 384 cycles respectively. By increasing peening coverage, surface roughness ( $R_a$ ) increased to 5.2 and 6.8  $\mu\text{m}$  (figure 4.34) respectively, which causes easy crack initiation near surface. Figure 4.50 shows the inclusions present at surface after LSPwC, where crack initiation activated. Similar results were reported by Wang, Lu, and Wang 2004. Repetitive peening with higher power density created burnt spots at peening surface, which enhances risk of fatigue failure, and observed in ECAP-LSPwC processed samples with 200 and 300 % of coverage (Liu et al. 2007).

## 4.8 Summary

“Results and Discussion” chapter is a collection of all data extracted during experiments and explanation for results observed. In first part, ECAP were carried out for four passes on AM80 alloy, microstructures and tensile strength were analysed.

### 4.8.1 ECAP processed samples

Table 4. 1 Grain refinement analysis of ECAP processed samples

Sl. No.	Material processing stage	Average grain size ( $\mu\text{m}$ )
1	As-Cast (received)	Dendritic, 100
2	Homogenized	100
3	ECAP-1-Pass	65
4	ECAP-2-Pass	45
5	ECAP-3-Pass	8
6	ECAP-4-Pass	3

Table 4. 2 X-ray diffraction of ECAP processed samples

Sl. No.	Phases identified	Lattice structure
1	Mg	Hexagonal close packing
2	$\text{Mg}_{17}\text{Al}_{12}$	Cubic
3	$\text{Mg}_2\text{Al}_3$	Cubic
4	$\text{MnAl}_6$	orthorhombic

Table 4. 3 **Tensile test results** of ECAP processed samples

Sl. No.	Material processing stage	Yield Strength (0.2 % of strain) (MPa)	Tensile Strength (MPa)	% of elongation
1	As-Cast (received)	48	140	04
2	ECAP-1-Pass	70	270	26
3	ECAP-2-Pass	145	310	24
4	ECAP-3-Pass	97	240	17
5	ECAP-4-Pass	105	205	12

Highlights of **Fractography** analysis of ECAP processed samples (Tensile test)

As-cast sample: Trans-granular crack flow was observed with micro voids, and fracture was characterized by cleavage facets, steps and rivers. Dimples were visible in some regions; combination of cleavage and dimples are observed along with undesired cracks. Fracture is a combination of brittle and ductile fracture and more dominated by brittle behaviour.

ECAP-2P sample: 2-pass sample under route B<sub>C</sub> showed bimodal structure, where small grains were surrounded by large grains and these led to heterogeneous fractured surface, having dimples of different sizes. Small dimple caused more elongation compared to large dimples. This fractured surface consisted of cleavage facets, steps, small dimples and large dimples with some secondary cracks and influences combination of ductile and brittle nature.



#### 4.8.2 ECAP-LSPwC processed samples

Table 4. 4 Refinement of grains due to **ECAP (2P) +LSP** at surface level

Sl. No.	Material processing stage	SEM Findings	TEM Findings
1	ECAP (2P) +LSP 100 %	5 to 2 $\mu\text{m}$ grains were observed	Banded structure, more precipitates, Nano grains in the range of 70 nm
2	ECAP (2P) +LSP 200 %	Microstructures observed in the form of flower petals (Clusters)	Intersection of banded structure due to repetitive peening, High density dislocations in Mg matrix, Nano grains in the range of 30 nm
3	ECAP (2P) +LSP 300 %	High distorted non-linear grains	Banded structures in needle form, more intense dislocations in grain, Nano grains of less than 15 nm is observed

X-ray diffraction of **ECAP+LSP** processed samples: Change in peak intensity was observed, as the sample processed from as-cast to ECAP+LSP 300 %, indicating the formation of new grains and possible induction of new residual stresses due to material processing.

Table 4. 5 Tensile test results of **ECAP-LSPwC** processed samples

Sl. No.	Material processing stage	Tensile Strength (MPa)
1	ECAP-2-Pass	310
2	ECAP (2P) +LSPwC 100 %	350
3	ECAP (2P) +LSPwC 200 %	390
4	ECAP (2P) +LSPwC 300 %	405

Highlights of fractography of **ECAP+LSPwC** samples (Tensile test)

ECAP+LSPwC 100 % coverage: Change in hardness near peened surface, delays in crack initiation and fracture, due to overloading in tensile mode, small dimples were created on cleavage facets due to peening.

ECAP+LSPwC 200 % coverage: Crack propagates from peened region towards ECAP processed region, Cleavage dominated fracture mode and leads to catastrophic failure, as mixed mode of ductile and brittle fracture. As percentage of dimples increase, more elongation was observed.

ECAP-LSPwC 300 % coverage: Percentage of dimples near the LSPwC processed surface was high when compared with 100 and 200% samples and hence more ductility, many small sized dimples were observed near peening surface and voids are nucleated at inclusions which are grown by higher loads.

#### 4.8.3 Nano Indentation

Maximum plastic deformation was observed in 2P-ECAP+LSP 100 % with increase in strength, ductility and stiffness compared to other samples. Hence, it consumes more energy before permanent deformation.

Homogenized sample showed hardness value of 0.92 GPa at one surface. Further 2-pass ECAP processed sample showed hardness of 1.36 GPa, with little variation. LSP processed samples showed increase in hardness at surface, and decrease in hardness at the interior (depth) of sample. Hardness and Elastic modulus were inversely proportional to projected contact area of indenter; hence both showed similar behaviour across the processing depth.

#### 4.8.4 Roughness measurement

Table 4. 6 Roughness measured for ECAP-LSPwC samples

Sl. No.	Material processing stage	Roughness ( $R_a$ ) ( $\mu\text{m}$ )
1	ECAP-2-Pass	0.638
2	ECAP (2P) +LSP 100 %	3.584
3	ECAP (2P) +LSP 200 %	5.235
4	ECAP (2P) +LSP 300 %	6.824

#### 4.8.5 Wear analysis

ECAP+LSP processed samples showed good wear resistance at beginning, but decreased as the sample wear out. As hardness increases, wear resistance also increased and it starts decreasing as the treated surface worn out.

Microscopic studies revealed that the worn surfaces consists of grooves in the direction of sliding, caused by plastic deformation, occurred by abrasive wear mechanism. Delamination occurred due to detachment of material, caused by cracks, perpendicular to sliding direction. Oxidation will be one of the dominating wear mechanism in Mg based alloys and causes easy detachment of oxidised fragments.

#### 4.8.6 Residual stresses

Tensile profile of residual stress was observed in as-cast sample. Values of stress reduced in homogenised sample from 65 to 25 MPa, because of stress relieving during grain growth. 2-Pass ECAP processed sample shows compressive stress in nature,

Increase of compressive residual stress was observed with LSPwC, and intensity of stress increases from -235 to -280 MPa from 100 to 300 % of coverage.

#### 4.8.7 Fatigue analysis

Fatigue experiments were carried out with stress ratio of 0.125 at maximum stress of 120 MPa.

Table 4. 7 Fatigue life cycles of ECAP+LSPwC processed samples

Sl. No.	Material processing stage	Fatigue life cycles
1	As-cast	1
2	ECAP-2-Pass	7539
3	ECAP (2P) +LSP 100 %	85268
4	ECAP (2P) +LSP 200 %	22987
5	ECAP (2P) +LSP 300 %	384

Fractrography reveals that, as cast samples fails due to tensile loading, ECAP and ECAP+LSP samples reveals the crack initiation location at outer surface of samples, propagates inside the material, followed by fracture.

## CHAPTER 5

### CONCLUSIONS

Severe plastic deformation was executed by two different process, for tailoring of grains. They are i) ECAP, for bulk refinement of grains and ii) LSP for grain refinement at near surface.

#### 5.1 Equal channel angular pressing for bulk refinement of grains

ECAP was carried out on split die, at elevated temperature of 275° C, with a strain rate of 0.5 mms<sup>-1</sup> on homogenized sample for upto four pass. Processed samples were investigated for microscopic observations, to understand the formation of new grains. Tensile tests witnessed change in strength and experiments of X-ray diffraction revealed the presence of different phases in material.

##### Outcomes:

- As-received material showed dendritic structures. Equiaxed grains of 3 µm were formed in samples deformed by ECAP for 4 passes. But inhomogeneity was observed due to unequal strain distribution, in all samples, processed by ECAP.
- Increase in tensile strength were observed in ECAP process, and maximum tensile strength of 310 MPa were noticed at ECAP 2-pass with average grain size of 45 µm.
- X-ray diffraction revealed the presence of Mg<sub>17</sub>Al<sub>12</sub>, Mg<sub>2</sub>Al<sub>3</sub>, MnAl<sub>6</sub> with Mg phases, which had cubic and orthorhombic lattice structure with HCP structure (magnesium matrix). In as-received condition, Mg<sub>17</sub>Al<sub>12</sub> was identified at grain boundaries. As refinement of grain occurs, rearrangement of Mg<sub>17</sub>Al<sub>12</sub> occurred at grain boundaries. Redistribution Mg<sub>17</sub>Al<sub>12</sub> phase, enhanced the strength and ductility of material.

#### 5.2 Laser shock peening for grain refinement at near surface

Laser shock peening without coating was executed on 2-pass ECAP processed (high tensile strength) sample at energy density of 8 GWcm<sup>-2</sup>, with a beam diameter of 0.8 mm at 100, 200 and 300 percentage of coverage. LSPwC processed samples were characterized using electron microscopes, tensile tests, confocal microscope, X-ray

diffraction, for residual stresses, nano indentation, wear and fatigue experiments. The outcomes of these characterizations are mentioned below.

- SEM and TEM analyses revealed the formation of nano grains, due to LSP effect, at near surface. As sample were processed with ECAP 2-pass prior to LSP, grain size of 45  $\mu\text{m}$  was obtained, and the result demonstrated tailoring of grains near surface by different LSP parameter.
- Microstructures, similar to clusters of flower petals, and banded shaped structure, were observed in SEM and TEM analysis.
- Increase in tensile strength was observed with ECAP+LSP processed sample. Further refinement of grains, at near surface strengthens the grain boundaries.
- Fractography revealed combination of ductile and brittle failures, and small dimples at near surface proved increase in strength and ductility, due to peening effect.
- Increase in energy absorption before failure, was observed in ECAP+LSP, 100 % coverage sample, and there was a slight decrease in energy absorption at 200 and 300 % of coverage.
- Measurement of hardness on ECAP+LSP processed sample showed, maximum hardness at surface and starts decreasing as depth increases.
- Increase in surface roughness caused by impacts of the laser pulses was observed, and small dents or surface roughness increased due to interaction of laser energy on metal surface causes evaporation of metal in very short interval and induces plasma blast.
- Increase in wear resistance was observed from wear analysis on peened samples due to increase in hardness, and surface grain refinement.
- There was change in residual stress profile from tensile to compression, as the material was processed by ECAP. Because of accumulated strain during ECAP, magnitude of compressive residual stresses increases effectively, due to peening effect.
- Fatigue experiments clearly distinguish the effect of ECAP and ECAP-LSP on reliability of material. Experiments were carried out at 120 MPa of maximum

stress with 0.125 of stress ratio and ECAP-LSP with 100 % of coverage showed highest fatigue life.

- Even though increase in tensile strength, hardness and compressive residual stresses were identified in ECAP-LSP at coverage of 200 and 300 %, decrease in fatigue life were recorded, effectively. Fracture investigation revealed the formation of surface damage due to repetitive peening, which acted as nucleation for crack formation.

## **FUTURE WORK**

### **Extension of present work**

Present work doesn't cover EBSD analysis of processed material, During LSP, surface damage occurred, which resulted in decrease of fatigue strength in 200 and 300 % of coverage. Optimization of process and some more advanced material characterization required idealized the process more effective. Hence future work is highly effective and more effective and promised results can be expected.

### **Importance of ECAP+LSP process in bio material**

Mg alloys are impressed by bio-compatibility while building implants and other relative application, but there is a strong draw back in terms of limited fatigue life and high corrosion rate. Research work, carried out, with respect to, tailoring of grains showed an effective improvement in fatigue life, with ECAP processed sample, and significant improvement with ECAP-LSP 100% coverage sample. Hence, vast research gap can be addressed with fatigue life and controlled corrosion rate of Mg alloys.

### **In Aerospace industries**

Critical parts like wing root, landing gears, and many more aerospace structures demand more stable material due to large loads. But these parts are made of strong wrought titanium. Research, in ECAP and LSP, showed improved mechanical properties, including fatigue life component. Hence, there is an opportunity to build more optimized structure using these techniques.

### **LSP at elevated temperature**

Most of the LSP processes were carried out at room temperature, due to required transparent layer (water or glass) for trapping laser beam. But if LSP is processed at elevated temperature, there is an opportunity to activate additional slip system, in HCP material and hence possibility of achieving better results. Hence, it is important to find suitable transparent material (some other liquids having high boiling point, having good optical index) which can be operated at high temperature.

## REFERENCES

- Abbaschian, R., Abbaschian, L., and Reed-Hill, R. E. (2009). *Physical metallurgy principles*. Cengage Learning.
- Agnew, S. R., and Tom, C. N. (2003). “Study of slip mechanisms in a magnesium alloy by neutron diffraction and modeling.” 48, 1003–1008.
- Akbaripannah, F., Fereshteh-Saniee, F., Mahmudi, R., and Kim, H. K. (2013a). “The influences of extrusion and equal channel angular pressing (ECAP) processes on the fatigue behavior of AM60 magnesium alloy.” *Mater. Sci. Eng. A*, 565, 308–316.
- Akbaripannah, F., Fereshteh Saniee, F., Mahmudi, R., and Kim, H. K. (2013b). “The influences of extrusion and equal channel angular pressing (ECAP) processes on the fatigue behavior of AM60 magnesium alloy.” *Mater. Sci. Eng. A*, 565, 308–316.
- Alaneme, K., and Okotete, E. (2017). “Enhancing plastic deformability of Mg and its alloys — A review of traditional and nascent developments.” *J. Magnes. Alloy.*, 5(4), 460–475.
- ASTM. (2009). *Standard Test Methods for Tension Testing of Metallic Materials 1*. *Astm Int*.
- ASTM. (2015). *Standard Practice for Conducting Force Controlled Constant Amplitude Axial Fatigue Tests of Metallic Materials 1*. *ASTM Int*.
- Azushima, A., Kopp, R., Korhonen, A., Yang, D. Y., Micari, F., Lahoti, G. D., Groche, P., Yanagimoto, J., Tsuji, N., Rosochowski, A., and Yanagida, A. (2008). “Severe plastic deformation ( SPD ) processes for metals.” *CIRP Ann. - Manuf. Technol.*, 57(57), 716–735.
- Bagheri, S., and Guagliano, M. (2009). “Review of shot peening processes to obtain nanocrystalline surfaces in metal alloys.” *Surf. Eng.*, 25(1), 3–14.
- Bagherpour, E., Pardis, N., and Reihanian, M. (2018). “An overview on severe plastic deformation: research status, techniques classification, microstructure evolution, and applications.” *Int. J. Adv. Manuf. Technol.*, 100, 1647–1694.
- Bao, Y. W., Wang, W., and Zhou, Y. C. (2004). “Investigation of the relationship between elastic modulus and hardness based on depth-sensing indentation measurements.” *Acta Mater.*, 52(18), 5397–5404.
- Barnett, M. R., Keshavarz, Z., Beer, A. G., and Atwell, D. (2004). “Influence of grain size on the compressive deformation of wrought Mg-3Al-1Zn.” *Acta Mater.*, 52(17), 5093–5103.
- Biswas, S., Suwas, S., Sikand, R., and Gupta, A. K. (2011). “Analysis of texture evolution in pure magnesium and the magnesium alloy AM30 during rod and tube



extrusion.” *Mater. Sci. Eng. A*, 528(10–11), 3722–3729.

Brown, D. W., Agnew, S. R., Bourke, M. A. M., Holden, T. M., Vogel, S. C., and Tomé, C. N. (2005). “Internal strain and texture evolution during deformation twinning in magnesium.” *Mater. Sci. Eng. A*, 399(1–2), 1–12.

Chapuis, A. (2014). “Low temperature plane strain compression of a magnesium single crystal with  $\langle c \rangle$  axis constrained.” *Mater. Sci. Eng. A*, 590, 401–405.

Chapuis, A., and Driver, J. H. (2011). “Temperature dependency of slip and twinning in plane strain compressed magnesium single crystals.” *Acta Mater.*, 59(5), 1986–1994.

Christian, J. W., and Mahajan, S. (1995). “Deformation twinning.” *Prog. Mater. Sci.*, 39(1–2), 1–157.

Dahle, A. K., Lee, Y. C., Nave, M. D., Scha, P. L., and Stjohn, D. H. (2001). “Development of the as-cast microstructure in magnesium - aluminium alloys.” *J. Light Met.*, 1, 61–72.

Dai, F., Zhou, J., Lu, J., and Luo, X. (2016). “A technique to decrease surface roughness in overlapping laser shock peening.” *Appl. Surf. Sci.*, 370, 501–507.

Dieter, G. E., and Bacon, D. (1962). “Mechanical metallurgy.” *J. Franklin Inst.*

Easton, M. A., Qian, M., Prasad, A., and StJohn, D. H. (2016). “Recent advances in grain refinement of light metals and alloys.” *Curr. Opin. Solid State Mater. Sci.*, 20(1), 13–24.

Eisenmeier, G., Holzwarth, B., Höppel, H. ., and Mughrabi, H. (2001). “Cyclic deformation and fatigue behaviour of the magnesium alloy AZ91.” *Mater. Sci. Eng. A*, 319, 578–582.

Ferrasse, S., Segal, V. M., Alford, F., Kardokus, J., and Strothers, S. (2008). “Scale up and application of equal-channel angular extrusion for the electronics and aerospace industries.” *Mater. Sci. Eng. A*, 493(1–2), 130–140.

Figueiredo, R. B., and Langdon, T. G. (2010). “Grain refinement and mechanical behavior of a magnesium alloy processed by ECAP.” *J. Mater. Sci.*, 45(17), 4827–4836.

Friedrich, H. E., and L.Mordike, B. (2006). *Magnesium Technology: Metallurgy, Design Data, Applications*. Springer-Verlag Berlin Heidelberg.

Gencalp Irizalp, S., and Saklakoglu, N. (2016). “High strength and high ductility behavior of 6061-T6 alloy after laser shock processing.” *Opt. Lasers Eng.*, 77, 183–190.

Gopi, K. R., Nayaka, H. S., and Sahu, S. (2016). “Investigation of Microstructure and Mechanical Properties of ECAP-Processed AM Series Magnesium Alloy.” *J. Mater.*

*Eng. Perform.*, 25(9), 3737–3745.

Gopi, K. R., Shivananda Nayaka, H., and Sahu, S. (2017a). “Wear Properties of ECAP-Processed AM80 Magnesium Alloy.” *J. Mater. Eng. Perform.*, 26(7), 3399–3409.

Gopi, K. R., Shivananda Nayaka, H., and Sahu, S. (2017b). “Microstructural Evolution and Strengthening of AM90 Magnesium Alloy Processed by ECAP.” *Arab. J. Sci. Eng.*

Gujba, A. K., and Medraj, M. (2014). *Laser peening process and its impact on materials properties in comparison with shot peening and ultrasonic impact peening. Materials (Basel)*.

Hammersley, G., Hackel, L. A., and Harris, F. (2000). “Surface prestressing to improve fatigue strength of components by laser shot peening.” *Opt. Lasers Eng.*, 34(4–6), 327–337.

Hong, T., Ooi, J. Y., and Shaw, B. (2008). “A numerical simulation to relate the shot peening parameters to the induced residual stresses.” *Eng. Fail. Anal.*, 15(8), 1097–1110.

Horita, Z., Furukawa, M., Nemoto, M., and Langdon, T. G. (2010). “Development of fine grained structures using severe plastic deformation.” *Mater. Sci. Technol.*, 16(11–12), 1239–1245.

Hosaka, T., Yoshihara, S., Amanina, I., and Macdonald, B. J. (2017). “Influence of Grain Refinement and Residual Stress on Corrosion Behavior of AZ31 Magnesium Alloy Processed by ECAP in RPMI-1640 Medium.” *Procedia Eng.*, 184, 432–441.

Jacot, A., Maijer, D., and Cockcroft, S. (2000). “Modeling of microstructure and residual stress in cast iron calender rolls.” *Metall. Mater. Trans. A Phys. Metall. Mater. Sci.*, 31(4), 1201–1211.

Jahadi, R., Sedighi, M., and Jahed, H. (2014). “ECAP effect on the micro-structure and mechanical properties of AM30 magnesium alloy.” *Mater. Sci. Eng. A*, 593, 178–184.

Janecek, M., Minarik, P., Krajňák, T., Cizek, J., Kužel, R., Dopita, M., Srba, O., and Gubicza, J. (2017). “Mechanical Properties and Microstructure Development in Ultrafine-grained Materials Processed by Equal-channel Angular Pressing.” *Sev. Plast. Deform. Tech.*, M. Cabibbo, ed., Rijeka: InTech.

Jing-yuan, L. I., Jian-xin, X. I. E., Jun-bing, J. I. N., and Zhi-xiang, W. (2012). “Microstructural evolution of AZ91 magnesium alloy during extrusion and heat treatment.” *Trans. Nonferrous Met. Soc. China*, 22(5), 1028–1034.

Kim, H. L., Park, J. S., and Chang, Y. W. (2012). “Effects of lattice parameter changes on critical resolved shear stress and mechanical properties of magnesium binary single crystals.” *Mater. Sci. Eng. A*, 540, 198–206.

- Kim, W. J., Hong, S. I., Kim, Y. S., Min, S. H., Jeong, H. T., and Lee, J. D. (2003). "Texture development and its effect on mechanical properties of an AZ61 Mg alloy fabricated by equal channel angular pressing." *Acta Mater.*, 51(11), 3293–3307.
- Kobayashi, M., Matsui, T., and Murakami, Y. (1998). "Mechanism of creation of compressive residual stress by shot peening." *Int. J. Fatigue*, 20(5), 351–357.
- Kochmann, D. M., and Le, K. C. (2009). "A continuum model for initiation and evolution of deformation twinning." *J. Mech. Phys. Solids*, 57(6), 987–1002.
- Koike, J. (2005). "Enhanced deformation mechanisms by anisotropic plasticity in polycrystalline Mg alloys at room temperature." *Metall. Mater. Trans. A*, 36(7), 1689–1696.
- Koike, J., Ohyama, R., Kobayashi, T., Suzuki, M., and Maruyama, K. (2003). "Grain-Boundary Sliding in AZ31 Magnesium Alloys at Room Temperature to 523 K." *Mater. Trans.*, 44(4), 445–451.
- Kulekci, M. K. (2008). "Magnesium and its alloys applications in automotive industry." *Int. J. Adv. Manuf. Technol.*, 39(9–10), 851–865.
- Kulkarni, K. N., and Luo, A. A. (2013). "Interdiffusion and phase growth kinetics in magnesium-aluminum binary system." *J. Phase Equilibria Diffus.*, 34(2), 104–115.
- Kulyasova, O., Islamgaliev, R., Mingler, B., and Zehetbauer, M. (2009). "Microstructure and fatigue properties of the ultrafine-grained AM60 magnesium alloy processed by equal-channel angular pressing." *Mater. Sci. Eng. A*, 503(1–2), 176–180.
- Lainé, S. J., Knowles, K. M., Doorbar, P. J., Cutts, R. D., and Rugg, D. (2017). "Microstructural characterisation of metallic shot peened and laser shock peened Ti–6Al–4V." *Acta Mater.*, 123, 350–361.
- Lavrentev, F. F. (1975). "Relation of Dislocation Density in Different Slip Systems to Work Hardening Parameters for Magnesium Crystals." 18, 261–270.
- Lee, Y. C., Dahle, A. K., and StJohn, D. H. (2000). "The role of solute in grain refinement of magnesium." *Metall. Mater. Trans. A*, 31(11), 2895–2906.
- Liu, Q., Yang, C. H., Ding, K., Barter, S. A., and Ye, L. (2007). "The effect of laser power density on the fatigue life of laser-shock-peened 7050 aluminium alloy." *Fatigue Fract. Eng. Mater. Struct.*, 30(11), 1110–1124.
- Lojkowski, W., Djahanbakhsh, M., and Bu, G. (2001). "Nanostructure formation on the surface of railway tracks." 303, 197–208.
- Lou, S., Li, Y., Zhou, L., Nie, X., He, G., Li, Y., and He, W. (2016). "Surface nanocrystallization of metallic alloys with different stacking fault energy induced by laser shock processing." *Mater. Des.*, 104, 320–326.

- Lu, J. Z., Luo, K. Y., Zhang, Y. K., Sun, G. F., Gu, Y. Y., Zhou, J. Z., Ren, X. D., Zhang, X. C., Zhang, L. F., Chen, K. M., Cui, C. Y., Jiang, Y. F., Feng, A. X., and Zhang, L. (2010). "Grain refinement mechanism of multiple laser shock processing impacts on ANSI 304 stainless steel." *Acta Mater.*, 58(16), 5354–5362.
- Lu, J. Z., Zhang, L., Feng, A. X., Jiang, Y. F., and Cheng, G. G. (2009). "Effects of laser shock processing on mechanical properties of Fe-Ni alloy." *Mater. Des.*, 30(9), 3673–3678.
- Lü, Y. ., Wang, Q. ., Ding, W. ., Zeng, X. ., and Zhu, Y. . (2000). "Fracture behavior of AZ91 magnesium alloy." *Mater. Lett.*, 44(5), 265–268.
- Ma, E. (2006). "Eight routes to improve the tensile ductility of bulk nanostructured metals and alloys." *Jom*, 58(4), 49–53.
- Maawad, E., Sano, Y., Wagner, L., Brokmeier, H. G., and Genzel, C. (2012). "Investigation of laser shock peening effects on residual stress state and fatigue performance of titanium alloys." *Mater. Sci. Eng. A*, 536, 82–91.
- Mathur, H. N., Maier-Kiener, V., and Korte-Kerzel, S. (2016). "Deformation in the  $\gamma$ -Mg17Al12 phase at 25–278 °C." *Acta Mater.*, 113, 221–229.
- Meguid, S. A., Shagal, G., and Stranart, J. C. (1999). "Finite element modelling of shot-peening residual stresses." *J. Mater. Process. Technol.*, 92–93, 401–404.
- Mixte, L. U., No, R., Prieur, A., Cedex, A., and Received, F. (1995). "Laser shock processing: a review of the physics and applications." *Opt. Quantum Electron.*, 27, 1213–1229.
- Montross, C. S., Wei, T., Ye, L., Clark, G., and Mai, Y. W. (2002). "Laser shock processing and its effects on microstructure and properties of metal alloys: A review." *Int. J. Fatigue*, 24(10), 1021–1036.
- Mordike, B. L., and Ebert, T. (2001). "Magnesium properties - application - potential." *Mater. Sci. Eng. A*, 302(1), 37–45.
- Muránsky, O., Barnett, M. R., Carr, D. G., Vogel, S. C., and Oliver, E. C. (2010). "Investigation of deformation twinning in a fine-grained and coarse-grained ZM20 Mg alloy: Combined in situ neutron diffraction and acoustic emission." *Acta Mater.*, 58(5), 1503–1517.
- Nie, X., He, W., Zhou, L., Li, Q., and Wang, X. (2014). "Experiment investigation of laser shock peening on TC6 titanium alloy to improve high cycle fatigue performance." *Mater. Sci. Eng. A*, 594, 161–167.
- Nieh, T. G., and Wadsworth, J. (1991). "Hall-Petch Relation in Nanocrystalline Solids." *Scr. Met. Mater.*, 25, 955–958.

- Noyan C, I., and Cohen B, J. (1986). *Residual Stress Measurement by Diffraction and Interpretation*. (B. Ilshner and N. Grant J, eds.), Springer-Verlag.
- Obara, T., Yoshinga, H., and Morozumi, S. (1973). “{112} Slip system in magnesium.” *Acta Metall.*, 21(7), 845–853.
- Pan, F., Yang, M., and Chen, X. (2016). “A Review on Casting Magnesium Alloys: Modification of Commercial Alloys and Development of New Alloys.” *J. Mater. Sci. Technol.*, 32(12), 1211–1221.
- Pekguleryuz, M. O., Kainer, K. U., Arslan Kaya, A., and Witte, F. (2013). *Fundamentals of Magnesium Alloy Metallurgy. Fundam. Magnes. Alloy Metall.*
- Peyre, P., Fabbro, R., Merrien, P., and Lieurade, H. P. (1996). “Laser shock processing of aluminium alloys. Application to high cycle fatigue behaviour.” *Mater. Sci. Eng. A*, 210, 102–113.
- Pineau, A., Benzerga, A. A., and Pardoën, T. (2016). “Failure of metals I: Brittle and ductile fracture.” *Acta Mater.*, 107, 424–483.
- Pourbahari, B., Mirzadeh, H., and Emamy, M. (2018). “The Effects of Grain Refinement and Rare Earth Intermetallics on Mechanical Properties of As-Cast and Wrought Magnesium Alloys.” *J. Mater. Eng. Perform.*, 27(3), 1327–1333.
- Rams, J., Taltavull, C., Rodrigo, P., Torres, B., and Lo, A. J. (2014). “Dry sliding wear behavior of AM50B magnesium alloy.” *Mater. Des.*, 56, 549–556.
- Ren, X. D., Huang, J. J., Zhou, W. F., Xu, S. D., and Liu, F. F. (2015). “Surface nanocrystallization of AZ91D magnesium alloy induced by laser shock processing.” *Mater. Des.*, 86, 421–426.
- Ritchie, R. ~O. (1998). “Mechanism of Fatigue-Crack Propagation in Ductile and Brittle Materials”.” *Int. J. Fract.*, 100, 55–83.
- Seipp, S., Wagner, M. F.-X., Hockauf, K., Schneider, I., Meyer, L. W., and Hockauf, M. (2012). “Microstructure, crystallographic texture and mechanical properties of the magnesium alloy AZ31B after different routes of thermo-mechanical processing.” *Int. J. Plast.*, 35, 155–166.
- Shen, X., Shukla, P., Nath, S., and Lawrence, J. (2017). “Improvement in mechanical properties of titanium alloy (Ti-6Al-7Nb) subject to multiple laser shock peening.” *Surf. Coatings Technol.*, 327, 101–109.
- Shukla, P. P., Swanson, P. T., and Page, C. J. (2014). “Laser shock peening and mechanical shot peening processes applicable for the surface treatment of technical grade ceramics: A review.” *Proc. Inst. Mech. Eng. Part B J. Eng. Manuf.*, 228(5), 639–652.

Smolin, A., Gutmanas, E., Levashov, E., Gotman, I., Dluhoš, L., Valiev, R. Z., Seefeldt, M., Rabkin, E., Mishnaevsky, L., Segurado, J., Prokoshkin, S., Sabirov, I., Korotitskiy, A., Solov'yov, A. V., Enikeev, N., and Psakh'e, S. (2014). "Nanostructured titanium-based materials for medical implants: Modeling and development." *Mater. Sci. Eng. R Reports*, 81, 1–19.

Somekawa, H., and Schuh, C. A. (2011). "Effect of solid solution elements on nanoindentation hardness, rate dependence, and incipient plasticity in fine grained magnesium alloys." *Acta Mater.*, 59(20), 7554–7563.

SONG, D., MA, A. b., JIANG, J. h., LIN, P. h., and YANG, D. h. (2009). "Corrosion behavior of ultra-fine grained industrial pure Al fabricated by ECAP." *Trans. Nonferrous Met. Soc. China (English Ed.)*, 19(5), 1065–1070.

StJohn, D. H., Qian, M., Easton, M. A., Cao, P., and Hildebrand, Z. (2005). "Grain refinement of magnesium alloys." *Metall. Mater. Trans. A Phys. Metall. Mater. Sci.*, 36(7), 1669–1679.

Tan, L., Sridharan, K., Allen, T. R., Nanstad, R. K., and McClinton, D. A. (2008). "Microstructure tailoring for property improvements by grain boundary engineering." *J. Nucl. Mater.*, 374, 270–280.

Tao, N. R., and Lu, K. (2009). "Nanoscale structural refinement via deformation twinning in face-centered cubic metals." *Scr. Mater.*, 60(12), 1039–1043.

Umapathi, A., and Swaroop, S. (2018). "Deformation of single and multiple laser peened TC6 titanium alloy." *Opt. Laser Technol.*, 100, 309–316.

Valiev, R. Z., and Alexandrov, I. V. (2000). "Bulk Nanostructured materials from severe plastic deformation." *Prog. Mater. Sci.*, (45), 103–189.

Valiev, R. Z., and Langdon, T. G. (2006). "Principles of equal-channel angular pressing as a processing tool for grain refinement." *Prog. Mater. Sci.*, 51(7), 881–981.

Vinogradov, A., Serebryany, V. N., and Dobatkin, S. V. (2017). "Tailoring Microstructure and Properties of Fine Grained Magnesium Alloys by Severe Plastic Deformation." *Adv. Eng. Mater.*, 1700785, 1–22.

Wagner, L. (1999). "Mechanical surface treatments on titanium, aluminum and magnesium alloys." *Mater. Sci. Eng. A*, 263(2), 210–216.

Wang, X. S., and Fan, J. H. (2006). "An evaluation on the growth rate of small fatigue cracks in cast AM50 magnesium alloy at different temperatures in vacuum conditions." *Int. J. Fatigue*, 28(1), 79–86.

Wang, X. S., Lu, X., and Wang, D. H. (2004). "Investigation of surface fatigue microcrack growth behavior of cast Mg-Al alloy." *Mater. Sci. Eng. A*, 364(1–2), 11–

16.

Wu, L. J., Luo, K. Y., Liu, Y., Cui, C. Y., Xue, W., and Lu, J. Z. (2018). "Effects of laser shock peening on the micro-hardness, tensile properties, and fracture morphologies of CP-Ti alloy at different temperatures." *Appl. Surf. Sci.*, 431, 122–134.

Xue, Q., Beyerlein, I. J., Alexander, D. J., and Gray, G. T. (2007). "Mechanisms for initial grain refinement in OFHC copper during equal channel angular pressing." *Acta Mater.*, 55(2), 655–668.

Yamashita, A., Horita, Z., and Langdon, T. G. (2001). "Improving the mechanical properties of magnesium and a magnesium alloy through severe plastic deformation." 300, 142–147.

Yoo, M. H., Agnew, S. R., Morris, J. R., and Ho, K. M. (2001). "Non-basal slip systems in HCP metals and alloys : source mechanisms." 321, 87–92.

Zhang, L., Luo, X., Liu, J., Leng, Y., and An, L. (2018). "Dry sliding wear behavior of Mg-SiC nanocomposites with high volume fractions of reinforcement." *Mater. Lett.*, 228, 112–115.

Zhang, R., Hou, X., Zhou, X., Gao, H., Mankoci, S., Qin, H., Ren, Z., Doll, G. L., Martini, A., Dong, Y., Sahai, N., and Ye, C. (2016). "Effects of laser shock peening on the wear and degradation behaviors of magnesium alloys." *ASME 2016 11th Int. Manuf. Sci. Eng. Conf. MSEC 2016*, 2, 1–6.

Zhang, X.-C., Zhang, C.-C., Wang, Z.-M., Tu, S.-T., Jia, Y.-F., and Fu, Y. (2019). "Effects of Different Mechanical Surface Enhancement Techniques on Surface Integrity and Fatigue Properties of Ti-6Al-4V: A Review." *Crit. Rev. Solid State Mater. Sci.*, 44:6 445-469.

Zhao, X., Zhang, Y., and Liu, Y. (2017). "Surface characteristics and fatigue behavior of gradient nano-structured magnesium alloy." *Metals (Basel)*, 7(2), 1–11.

### LIST OF PUBLICATIONS

Sl. No.	Title of the paper	Authors (in the same order as in the paper. Underline the Research Scholar's name)	Name of the Journal/ Conference/ Symposium, Vol., No., Pages	Month & Year of Publication	Category *
1	Numerical Simulation of Shot Peening Process on Equal Channel Angular Pressed Magnesium Alloy	<b><i>T.R. Praveen</i></b> , K.R. Gopi, H. Shivananda Nayaka	Silicon (SCI IF-1.21). doi:doi.org/10.1007/s12633-018-9778-3	April-2018	1
2	Influence of Equal Channel Angular Pressing and Laser Shock Peening on Fatigue Behaviour of AM80 Alloy	<b><i>T. R. Praveen</i></b> , H. Shivananda Nayaka, S. Swaroop	Surface & Coating Technology, (SCI IF-3.2), <a href="https://doi.org/10.1016/j.surfcoat.2019.03.072">https://doi.org/10.1016/j.surfcoat.2019.03.072</a>	March-2019	1
3	Strength enhancement of magnesium alloy through equal channel angular pressing and laser shock peening	<b><i>T. R. Praveen</i></b> , H. Shivananda Nayaka, S. Swaroop, Gopi K. R	Applied Surface Science, (SCI IF-5.2)	February-2020	1
4	Numerical Simulation of Shot Peening on ECAP processd AM80 alloy	<b><i>Praveen T. R</i></b> , H. Shivananda Nayaka	The 4 <sup>th</sup> International conference on Advances in Materials & Material Processing (ICAMMP-IV),	Nov 5 <sup>th</sup> -7 <sup>th</sup> 2016, IIT Kharagpur	4



5	Investigation of Surface Topology of Laser peening on ECAP processed Magnesium alloy	<i>Praveen T. R.</i> , H. Shivananda Nayaka	International conference on Advances in material and processing: Challenges and opportunities (AMPCO2017),	Nov 30th- Dec 2 <sup>nd</sup> 2017, IIT Roorkee	4
6	Effect of residual stresses on ECAP processed magnesium alloy	Praveen T. R, H. Shivananda Nayaka, N. R. Sathya Swaroop	All India Seminar on Residual Stress and Advanced NDE Techniques for Structural Integrity Assessment: Key Challanges & Remedies,	May 16th-17th 2018, NIAS-IISc Bangalore. (1st Place for poster prasentation)	4
7	Investigation of Grain Refinement and Residual Stress Characterization for ECAP and Laser Shock Peening processed AM80 Al	Praveen T. R, H. Shivananda Nayaka, N. R. Sathya Swaroop, K. Praveenkumar	Investigation of Grain Refinement and Residual Stress Characterization for ECAP and Laser Shock Peening processed AM80 Alloy	Oct 24 <sup>th</sup> -27 <sup>th</sup> 2018, Thiruvananthapuram, India	4

Category: 1: Journal paper, full paper reviewed      2: Journal paper, Abstract reviewed      3: Conference/Symposium paper, full paper reviewed  
4: Conference/Symposium paper, abstract reviewed      5: Others (including papers in Workshops, NITK Research Bulletins, Short notes etc.)

### Bio Data

1.	Name and full correspondence address	Praveen T. R. S/O Ramachandraiah B, 2 <sup>nd</sup> Main, 2 <sup>nd</sup> Cross, Hanumanthapura, Tumkur - 572103
2.	Email(s) and contact number(s)	<a href="mailto:Praveentr0@gmail.com">Praveentr0@gmail.com</a> 7022716971
3.	Institution	National Institute of Technology karnataka
4.	Date of Birth	27-Nov-1984

#### 5. Academic Qualification (Undergraduate Onwards)

Sl. No	Degree	Year	Subject	University/Institution	% of marks
1	Bachelor of Engineering	2006	Mechanical Engineering	Visvesvariah Technological University	61.4
2	Master of Engineering	2009	Machine design	Bangalore University	82.4
3	Ph.D	2020	Mechanical Engineering	National Institute of Technology Karnataka	-

#### 6. Professional Recognition/ Award/ Prize/ Certificate, Fellowship received by the applicant

Sl. No	Name of Award	Awarding Agency	Year
1.	Best Poster Award	<i>All India seminar on residual stress and advanced NDE techniques for structural integrity assessment: key challenges and remedies conducted by NIAS, IISc-Bangalore.</i>	2018

#### 7. Publications (List of papers published in SCI Journals, in year wise descending order)

Sl. No.	Author(s)	Title	Name of Journal	Volume	Page	Year
1.	<b>T. R Praveen,</b> H. Shivananda Nayaka, S. Swaroop, Gopi K. R	Strength enhancement of magnesium alloy through equal channel angular pressing and laser shock peening	Applied surface science	512	14755	2020
2.	<b>T. R Praveen,</b> H. Shivananda Nayaka, S. Swaroop,	Influence of Equal Channel Angular Pressing and Laser Shock Peening on Fatigue Behaviour of AM80 Alloy	Surface & Coatings Technology	369	221	2019
3.	<b>T.R. Praveen,</b> K.R. Gopi, H.S. Nayaka,	Numerical Simulation of Shot Peening Process on Equal Channel Angular Pressed Magnesium Alloy	Silicon	10	2463	2018

Praveen T. R